Measurement of the mass and natural width of the Higgs boson in the H to ZZ to 4ℓ decay channel with the ATLAS detector

A dissertation presented

by

William R Spearman

to

The Department of Physics

in partial fulfillment of the requirements

for the degree of

Doctor of Philosophy

in the subject of

Physics

Harvard University

Cambridge, Massachusetts

August 2014

Dissertation Advisor: Author:

João Pedro Barreiro Guimarães da Costa   **William R Spearman**

Measurement of the mass and natural width of the Higgs boson in the H to ZZ to 4ℓ decay channel with the ATLAS detector

Abstract

This thesis presents a measurement of the mass, natural width, and signal strength, defined as the yield normalized to the Standard Model prediction, of the Higgs boson in the $H \to ZZ^{(*)} \to 4\ell$ decay channel using an approach which utilizes event-by-event detector response information. The measurement is performed on p-p collision data recorded by the ATLAS experiment at the CERN Large Hadron Collider. The data corresponds to an integrated luminosity of 25 fb^{-1} with center-of-mass energies of 7 TeV and 8 TeV. The measured mass of the Higgs boson is $m_H = 124.57^{+0.48}_{-0.43}$ GeV. The signal strength was estimated at $\mu = 1.76^{+0.46}_{-0.37}$. Finally, the natural width of the Higgs was determined to be < 2.6 GeV with 95% confidence. The event-by-event approach used in this analysis involves the parameterization of the behavior of single leptons in the ATLAS detector and the convolution of a mass response with the Higgs truth distribution to derive the reconstruction level signal model.

Contents

List of Figures

List of Tables

Acknowledgments

I owe a huge debt of gratitude to many people. In particular I want to thank my advisor, João Pedro Barreiro Guimarães da Costa. He has selflessly given his time in mentoring me and motivating me. His insights into particle physics were absolutely invaluable. I could not have completed this analysis without the help of my fellow graduate student and friend, Siyuan Sun. His contribution to this thesis was monumental and without his tireless efforts, the analysis would never have reached completion. I also wish to thank my postdoc, Pierluigi Catastini. He taught me and guided me every step along the way and it is thanks to his encouragement and direction that the measurement was able to proceed. I want to recognize Graham Cree for his dedication and hard work in perfecting the electron response functions. His efforts were vital to the success of the measurement.

A special thanks also goes to Corrinne Mills and Alberto Belloni for their guidance during my first years at CERN. I would like to express my gratitude to David Lopez Mateos for mentoring me, encouraging me, and being willing to answer any question at any time. David is also an excellent mountaineering partner and I will miss exploring the Swiss alps with him.

I would like to thank the members of the Harvard ATLAS group, Masahiro Morii, John Huth, Melissa Franklin and all the ATLAS graduate students for being so wonderful to work with and learn from. I want to recognize Giovanni Zevi della Porta for being an amazing office-mate who taught me a great deal. I would like to thank Stephen Chan for his help in reading my thesis and for being a great friend.

Lastly, I want to thank my family and dedicate this thesis to them. Mark, Blair, Jacob, and Rebekah: your love and support have sustained me over the past five

years and I am so thankful to have you in my life. I also want to thank all my friends, in particular Eric Lewis and Ethan Williams, for your patience, understanding, and encouragement during the past five years. Thank you!

Chapter 1

Introduction

In 1964, Peter Higgs, François Englert, Robert Brout, Gerald Guralnik, C. R. Hagen, and Tom Kibble [12–14] developed the Higgs mechanism to give mass to the weak vector bosons, the $W^{\pm}$ and the Z. This Higgs mechanism predicted the existence of a scalar boson, known as the Higgs boson.

Nearly 50 years later, in 2012, the ATLAS and CMS collaborations discovered a new particle with a mass of about 125 GeV using data from p-p collisions at the Large Hadron Collider (LHC) [15, 16]. The ATLAS observation was based on an integrated luminosity of 4.9 fb^{-1} at a center of mass energy $\sqrt{s} = 7$ TeV and 5.8 fb^{-1} at $\sqrt{s} = 8$ TeV. The discovery was the result of a combination of analyses searching for the Higgs decay in the $H \rightarrow WW^{(*)} \rightarrow \ell\nu\ell\nu$, the $H \rightarrow ZZ^{(*)} \rightarrow 4\ell$, and the $H \rightarrow \gamma\gamma$ channels. In these channels, ℓ refers to electrons and muons only.

With the Higgs discovery, our focus shifted from discovery to measurement. This dissertation presents a measurement of the Higgs mass and width in the $H \rightarrow ZZ^{(*)} \rightarrow 4\ell$ decay channel using the combined 2011 and 2012 ATLAS dataset with an integrated

luminosity of 25 fb^{-1}. The mass of the Higgs is not predicted by Standard Model (SM) of particle physics. A direct measurement is essential to check the consistency of the SM and put constraints on the existence of new physics. The total decay width of the Higgs boson is predicted by the SM to be ~ 4.1 MeV. Any deviation from this would indicate the presence of new physics that couples to the Higgs sector.

The measurement of the mass and width of the Higgs boson must overcome a number of challenges. The small branching ratio for $H \rightarrow 4\ell$ yields few Higgs candidates. The off-shell $Z^{(*)}$ in the decay chain produces low-momentum leptons, hence understanding the efficiency of such leptons is important to increase the channel acceptance. To estimate the Higgs mass and decay width, it is necessary to develop signal and background models that can be used to fit the data. These models are made using Monte-Carlo templates and event-by-event techniques. In the event-by-event technique, the behavior of the leptons in the ATLAS detector is parameterized using *lepton response functions*. These lepton response functions are combined into mass response functions which can then be convolved with the shape of the Higgs resonance to produce an invariant mass signal model. Using these models, a combined probability density function is written which can then be used to fit Monte-Carlo and data to determine the expected and observed limits on the Higgs mass and width.

The dissertation is arranged in the following manner. Chapter 2 describes the theoretical understanding of the Higgs boson, its production and decay modes. Furthermore, the measurement of the mass and decay width of the Higgs boson is motivated. Chapter 3 discusses the Large Hadron Collider, while in Chapter 4, the ATLAS detector is introduced. Chapter 5 covers the performance of the muon reconstruction

algorithms and the corrections which bring the Monte-Carlo (MC) simulated data into agreement with ATLAS data. Such agreement is needed for understanding the effect of cuts and models. The measurement of the reconstruction and identification efficiency for low momentum muons using the J/ψ resonance is also discussed at length in Chapter 5.

The selection of Higgs candidate events is described in Chapter 6. These selections are chosen to reduce the Higgs backgrounds and provide a sample with high significance, $S/\sqrt{B}$. Using the candidate events selected in Chapter 6, we turn our attention to the measurement of the mass and width of the Higgs boson in Chapter 7. To perform this measurement, various signal and background models are needed which describe the shape of the signal and background distributions. Chapter 8 summarizes the results, putting them in context with other ATLAS and CMS measurements.

Chapter 2

Theory

2.1 The Standard Model

The Standard Model (SM) of particle physics is the culmination of a century of theoretical and experimental breakthroughs in the field of particle physics. The SM describes all of the known forces, with the exception of gravity, and all of the currently observed fundamental particles: both fermions and bosons. Furthermore, it predicts the existence of a scalar boson, the Higgs boson, that allows the vector bosons of the electroweak force to acquire mass while preserving their gauge symmetry. The force carrying bosons of the Standard Model are found in Table 2.1. The fermions in the Standard Model are shown in Table 2.1. In the SM, the fermions have a spin of $\frac{1}{2}$, while the force carrying bosons have a spin of 1. Additionally, for each particle there is a corresponding antiparticle which has the same mass and opposite charge.

Table 2.1: Bosons in Standard Model and their properties [9].

Force	Symbol	Name	Mass [GeV]	Charge [e]
Electromagnetism	γ	photon	0	0
	Z	Z boson	91.1876	0
Weak	W^+	W^+ boson	80.385	+1
	W^-	W^- boson	80.385	-1
Strong	g	gluon	0	0

Table 2.2: Fermions in Standard Model and their properties [9].

Generation	Symbol	Name	Mass [MeV]	Charge [e]	Boson Couplings
	e	electron	0.511	-1	γ, $W^\pm/Z$
First	ν_e	electron neutrino	< 0.001	0	$W^\pm/Z$
	u	up quark	$1.7 - 3.1$	2/3	γ, W$^\pm$/Z, g
	d	down quark	$4.1 - 5.7$	-1/3	γ, W$^\pm$/Z, g
	μ	muon	105.6	-1	γ, $W^\pm/Z$
Second	ν_μ	muon neutrino	< 0.001	0	$W^\pm/Z$
	c	charm quark	~ 1290	2/3	γ, W$^\pm$/Z, g
	s	strange quark	~ 100	-1/3	γ, W$^\pm$/Z, g
	τ	tau	1776.8	-1	γ, $W^\pm/Z$
Third	ν_τ	tau neutrino	< 0.001	0	$W^\pm/Z$
	c	charm quark	~ 1290	2/3	γ, W$^\pm$/Z, g
	b	bottom quark	~ 4.19	-1/3	γ, W$^\pm$/Z, g

2.1.1 The Glashow-Weinberg-Salam Theory of Weak Interactions

Fundamentally, quantum field theory provides the mathematical basis for the Standard Model of particle physics. In quantum field theory, the Lagrangian is the fundamental equation that encapsulates the parameters and interactions of particles. By applying the local gauge symmetries of a Lagrangian (e.g. $SU(2)$ or $U(1)$) to write the covariant derivative, massless gauge boson field(s) can be read off. For the electromagnetic and strong interactions, this procedure causes the photon and gluon

fields to emerge from the theory with coupling parameters measured by experiment. The weak force is known to have massive force carriers, the $W^\pm$ and Z bosons. Adding an explicit mass term causes the theory to be non-renormalizable, as an increasing number of tuning parameters are required to cancel divergences when calculating the terms from higher order diagrams. To solve these problems, Glashow, Weinberg, and Salam developed a theory of weak interactions which utilizes the Higgs mechanism to give mass to the weak gauge bosons [17,18]. To do this, they introduce a field, ϕ, which obeys $SU(2)$ and $U(1)$ gauge symmetries. This means that the gauge transformation of this field can be written as:

$$\phi \rightarrow e^{i\alpha^a \sigma^a/2} e^{i\beta/2} \phi \tag{2.1}$$

Where the σ^a are the Pauli-matrices, and α^a and β are arbitrary phases for the gauge transformation. The three Pauli matrices are written as:

$$\sigma_1 = \begin{pmatrix} 0 & 1 \\ 1 & 0 \end{pmatrix} \tag{2.2}$$

$$\sigma_2 = \begin{pmatrix} 0 & -i \\ i & 0 \end{pmatrix} \tag{2.3}$$

$$\sigma_3 = \begin{pmatrix} 1 & 0 \\ 0 & -1 \end{pmatrix} \tag{2.4}$$

The potential term of the Higgs Lagrangian, $\mathcal{L} = \left(D_\mu \phi\right)^\dagger D^\mu \phi - V_H$ seen in Figure 2.1, is chosen to be:

$$V_H = -\mu^2 \phi^\dagger \phi + \lambda \left(\phi^\dagger \phi\right)^2 \tag{2.5}$$
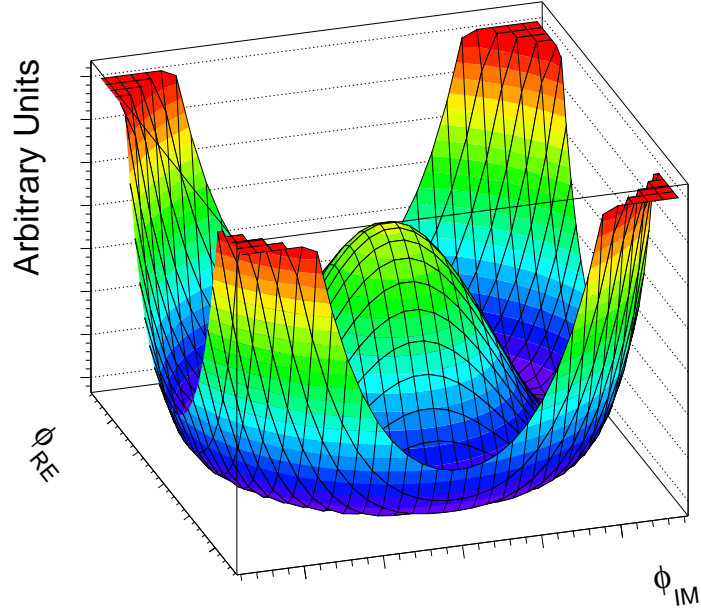
Figure 2.1: The Higgs potential, $V_H = \mu\phi^\dagger\phi + \lambda\left(\phi^\dagger\phi\right)^2$, split into the $\Re\left(\phi\right)$ and $\Im\left(\phi\right)$ plane.

So as to give a vacuum expectation value at:

$$\langle\phi\rangle = \frac{1}{2}\begin{pmatrix} 0 \\ v \end{pmatrix} \tag{2.6}$$

Where $v \equiv \sqrt{\frac{\mu^2}{\lambda}}$. The parameters λ and μ are field strength couplings in the potential. A gauge transformation where $\alpha^1 = \alpha^2 = 0$ and $\alpha^3 = \beta$ will make $\phi \to \phi$ and leave the field invariant. The covariant derivative of ϕ is:

$$D_\mu\phi = \left(\partial_\mu - i\frac{1}{2}gA_\mu^a\sigma^a - i\frac{1}{2}g'B_\mu\right)\phi \tag{2.7}$$

In which A_μ^a and B_μ are gauge fields corresponding to the U(1) and SU(2) symmetry groups with coupling constants of g and g' respectively. Evaluating the $(D_\mu\phi)^\dagger D^\mu\phi$

component of the Lagrangian at the vacuum expectation value gives:

$$\Delta \mathcal{L} = \frac{1}{2} \begin{pmatrix} 0 & v \end{pmatrix} \left(\frac{1}{2} g A_\mu^a \sigma^a + \frac{1}{2} g' B_\mu \right) \left(g \frac{1}{2} A^{b\mu} \sigma^b + \frac{1}{2} g' B^\mu \right) \begin{pmatrix} 0 \\ v \end{pmatrix} \tag{2.8}$$

Evaluating with the Pauli-matrices gives the following:

$$\Delta \mathcal{L} = \frac{1}{2} \left| \begin{pmatrix} g A_\mu^3 + g' B_\mu & g A_\mu^1 - i g A_\mu^2 \\ g A_\mu^1 + i g A_\mu^2 & -g A_\mu^3 + g' B_\mu \end{pmatrix} \begin{pmatrix} 0 \\ v \end{pmatrix} \right|^2 \tag{2.9}$$

Using the following basis:

$$W_\mu^\pm \equiv \frac{1}{\sqrt{2}} \left(A_\mu^1 \mp i A_\mu^2 \right) \tag{2.10}$$

$$Z_\mu^0 \equiv \frac{g A_\mu^3 - g' B_\mu}{\sqrt{g^2 + g'^2}} \tag{2.11}$$

$$A_\mu \equiv \frac{g' A_\mu^3 + g B_\mu}{\sqrt{g^2 + g'^2}} \tag{2.12}$$

The matrix multiplication yields:

$$\Delta \mathcal{L} = \left(\frac{vg}{2} \right)^2 W_\mu^+ W^{-\mu} + \frac{1}{2} \left(\frac{v \sqrt{g^2 + g'^2}}{2} \right)^2 Z_\mu Z^\mu + 0 \left(A_\mu A^\mu \right) \tag{2.13}$$

This indicates the existence of two massive charged vector bosons, $W_\mu^\pm$, with a mass of:

$$m_{W^\pm} = \frac{gv}{2} \tag{2.14}$$

A single neutral vector boson, given by the Z_μ field, with a mass of:

$$m_Z = \frac{1}{2} v \sqrt{g^2 + g'^2} \tag{2.15}$$

And a final massless scalar field, A_μ. A mixing angle between the coupling coefficients g and g' can be introduced which is defined as $g'/g \equiv \tan \theta_W$ which yields the familiar relationship $M_W / M_Z = \cos \theta_W$.

2.1.2 The Higgs Boson

In addition to giving mass to the Electroweak gauge bosons, the Higgs mechanism predicts the existence of a scalar Higgs boson [18]. The Higgs field can be expanded around the vacuum expectation value (v.e.v.) using another real-valued field $h(x)$ by writing:

$$\phi(x) = U(x) \frac{1}{\sqrt{2}} \begin{pmatrix} 0 \\ v + h(x) \end{pmatrix} \tag{2.16}$$

In which $U(x)$ represents a general $SU(2)$ gauge transformation. By using the unitary gauge in which $\alpha^1 = \alpha^2 = 0$ and $\alpha^3 = \beta$, the gauge transformation goes to unity $U(x) \to 1$. As discussed before, the Higgs Lagrangian that gives the non-zero vacuum expectation value is:

$$\mathcal{L} = |D_\mu \phi|^2 + \mu^2 \phi^\dagger \phi - \lambda \left(\phi^\dagger \phi\right)^2 \tag{2.17}$$

Leading to a vacuum expectation value at $\phi = \frac{1}{\sqrt{2}} \binom{0}{v}$ where $v \equiv \sqrt{\mu^2/\lambda}$. By substituting Equation 2.16 into Equation 2.17, one obtains:

$$\mathcal{L} = |D_\mu \phi|^2 + \mu^2 h^2 + \lambda v h^3 + \frac{1}{4}\lambda h^4 \tag{2.18}$$

Noticing that the term $-\mu^2 h^2$ looks like a mass term, one can define $m_H = \sqrt{2}\mu$ which leads to the following simplification:

$$\mathcal{L} = |D_\mu \phi|^2 + \frac{1}{2}m_H^2 h^2 + \sqrt{\frac{\lambda}{2}}m_h h^3 + \frac{1}{4}\lambda h^4 \tag{2.19}$$

To evaluate the kinetic term of the Higgs Lagrangian, $|D_\mu \phi|^2$, the substitution $v \to v + h(x)$ is made into Equation 2.13:

$$\Delta \mathcal{L} = \left[m_W^2 W^{\mu +} W_\mu^- + \frac{1}{2}m_Z^2 Z^\mu Z_\mu \right] \left(1 + \frac{h}{v}\right)^2 \tag{2.20}$$

This indicates that the Higgs to W boson coupling is $\propto 2\frac{m_W^2}{v}W^{\mu\,+}W_\mu^- h$ while the Higgs to Z boson coupling is $\propto \frac{m_Z^2}{v}Z^{\mu\,+}Z_\mu^- h$ [18]. These couplings indicate that the Higgs can couple to W^+W^- or ZZ pairs.

2.1.3 Higgs Production at the LHC

As discussed above, the Higgs mechanism gives mass to the $W^\pm$ and Z bosons. In addition, a new particle, the Higgs boson, is predicted. The Higgs mass is not constrained because $m_H = \sqrt{2\lambda}v$ and λ is a free parameter in the theory. The allowable vertices between the Higgs and the other particles of the Standard model are known, and these couplings depend on measurable parameters and the mass of the Higgs itself. Some of these parameters are not known to a high precision, such as the mass of the top quark and the W boson. Despite this, the production rates and decay branching ratios of the Higgs at a proton-proton collider like the Large Hadron Collider (LHC) can be calculated to a fairly high-precision.

As protons are themselves a conglomeration of three valence quarks (two ups and a down), sea quarks (of all flavors), and gluons, a vast array of Higgs production modes are available. The relative strengths of these production modes are determined by the Feynman vertices and the momentum fraction carried by each of the partons
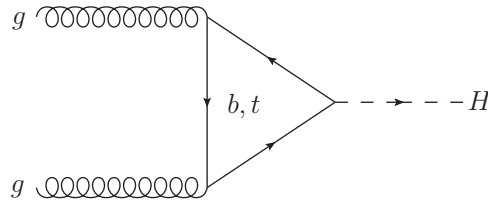
Figure 2.2: A Feynman diagram showing the most common Higgs production mode at the LHC: gluon-gluon fusion.
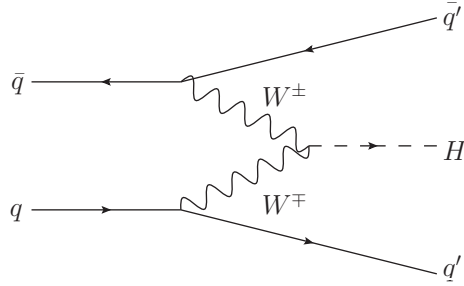
Figure 2.3: A Feynman diagram showing the lowest order Feynman diagram for Higgs production through vector boson fusion.

involved in the production. The most common Higgs production mode is that of gluon-gluon fusion. The lowest order Feynman diagram for this production mode is shown in Figure 2.2. The next most common production mode is known as vector boson fusion (VBF), and the lowest order Feynman diagram displaying this process is seen in Figure 2.3. In the case of VBF, a quark and antiquark fuse through vector bosons to create a Higgs. This production mode is notable because it invariably includes two jets in the final state which can be used to select these events.

The third most common production mode is associated production. In associated production, the Higgs is produced along with secondary particles. Adding the mass of these particles to the total energy of the final state makes their production less likely and renders these cross-sections smaller. The secondary particle, however, can make analyses in these channels somewhat easier, as the associated particle provides a means of tagging "interesting" events that could contain a Higgs produced in this mode. The first of these associated production modes is called vector boson associated Higgs production (with a W or Z boson). In this case two quarks fuse, creating a virtual W or Z boson that then radiates a Higgs; this is also known as Higgs-strahlung. This is seen in Figures 2.4 and 2.5. Antiquarks carry a small fraction of the proton's
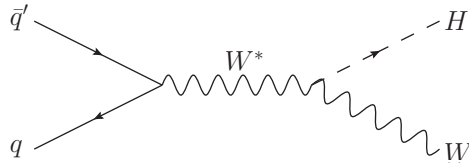
Figure 2.4: A Feynman diagram showing W boson, Higgs associated production.
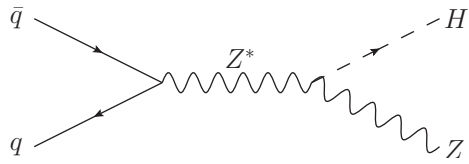
Figure 2.5: A Feynman diagram showing Z boson, Higgs associated production.

momentum, and this helps to account for the low production cross section for these associated production modes. The Higgs can also be produced along with a top quark-antiquark pair, as shown in Figure 2.6.

Figure 2.7 summarizes the production cross-sections for the Higgs boson as a function of the mass of the Higgs. For p-p collisions with a center of mass energy of 8 TeV, gluon-gluon fusion is the dominant production mode. The VBF channel, labeled $pp \rightarrow qqH$ in the Figure, accounts for approximately 10% of the gluon-gluon
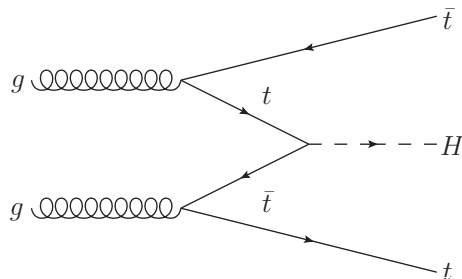
Figure 2.6: A Feynman diagram showing Higgs $t\bar{t}$ associated production.
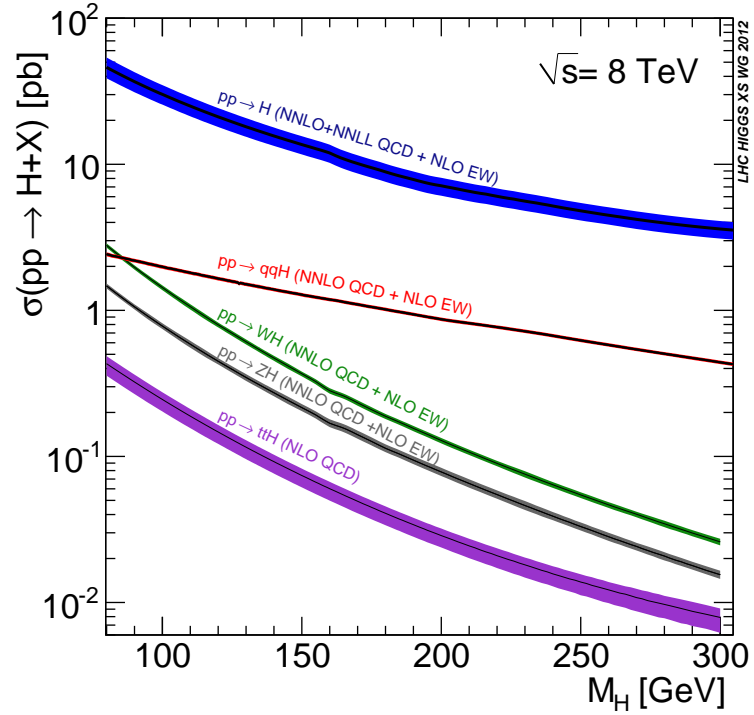
Figure 2.7: The Higgs production cross sections for *p-p* collisions with a center of mass energy $\sqrt{s} = 8$ TeV and their dependence on the mass of the Higgs [1].

fusion process. The associated production modes represent smaller contributions to the total Higgs production. They are labeled $pp \to WH$, $pp \to ZH$, and $pp \to ttH$ respectively in Figure 2.7.

2.2 Higgs Decay

The Higgs, upon production, will almost immediately decay into various particles. The decay, like the production, is mediated by the Higgs couplings. Couplings to fermions are proportional to the mass of the fermion. The couplings to the vector boson are more complex but they scale with the mass of the vector boson in question. Certain decay modes, however, will involve more than a single vertex. Some of these,
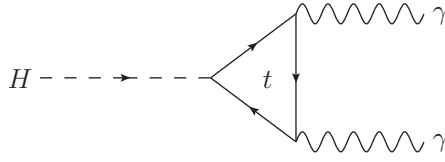
Figure 2.8: The lowest order Feynman diagram showing the Higgs decay to two photons. The top quark loop can be replaced with another charged fermion or a $W^\pm$ loop.
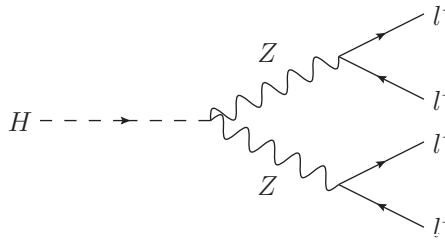
Figure 2.9: The lowest order Feynman diagram showing the Higgs decay to two Z-bosons, at least one of which will be off-shell for $m_H = 125$ GeV. Each of the Z-bosons then decays leptonically.

like the decay of the Higgs to two photons will involve a top quark loop, and others, like the decay of the Higgs to ZZ to 4-leptons, will have intermediate decay products which are produced before the final state particles that are observed in the detector. One of the most important decay modes for measuring the mass is the Higgs decay to two photons. The Feynman diagram showing this process is seen in Figure 2.8. This mode is useful because the energy of photons can be measured with good precision. Another decay mode, and the subject of this thesis, is the Higgs decay to two Z-bosons each of which then decays leptonically. The lowest order Feynman diagram representing this decay is seen in Figure 2.9.

In addition to the vertex factors, the Higgs decay will be affected by the available phase space for a given Higgs mass. For example, when the mass of the Higgs is less than about 182 GeV, the Higgs will not have the kinematic phase space to decay

into two real Z-bosons, and, thus the decay to ZZ will be suppressed, as one of the Zs would necessarily be off-shell. In Figure 2.12, the various branching fractions are shown as a function of the Higgs mass. The branching fraction is the ratio of the decay width divided by the total decay width of the Higgs boson (i.e. the sum of the decay widths for all channels).

Using the knowledge that the Higgs mass is near 125 GeV, $H \rightarrow b\bar{b}$ is the dominant process for the majority of the mass range. This is because the b-quark is the heaviest fermion for the entire kinematic phase space since $m_H < 2m_t$. Given that the top quark mass is about 173 GeV, the Higgs decay to $t\bar{t}$ will be heavily suppressed because kinematically both top quarks would have to be highly off-shell. Practically speaking, $H \rightarrow b\bar{b}$ is a difficult channel in which to measure the Higgs. This is because b-quark jets are produced in large numbers by the proton-proton collisions at the LHC. Furthermore, the poor jet energy resolution makes it difficult to resolve the wide signal mass shape against the large multi-jet background. Like the $b\bar{b}$ channel, a Higgs decay to $c\bar{c}$ or two gluons would suffer from many of the same problems.

The next most massive fermion is the tau lepton, τ. The tau is a fermion, but unlike the muon and electron, it decays quickly to a W boson and a neutrino. This decay can either be hadronic, as seen in Figure 2.10 or leptonic, as seen in Figure 2.11. Complex algorithms are used to tag these tau-decays and to separate them from similar events that do not involve a tau decay.

The $H \rightarrow WW$ decay dominates the mass region around 140 GeV. This is the point in phase space at which it is possible to produce two real W-bosons. The $H \rightarrow WW$ analysis can be performed in different sub-channels. The fully hadronic
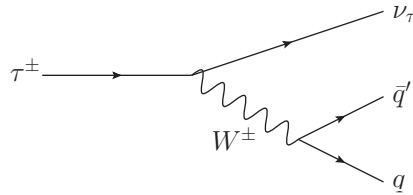
Figure 2.10: The lowest order Feynman diagram showing hadronic tau decay.
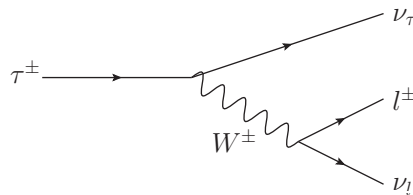
Figure 2.11: The lowest order Feynman diagram showing leptonic tau decay.

sub-channel, where both W bosons decay hadronically is difficult at the LHC because of the large jet background produced by p-p collisions. There is a semi-hadronic mode where one W decays to a lepton and a neutrino and the other decays hadronically. Again, this suffers from high backgrounds. The third mode occurs when both W-bosons decay leptonically. This has the benefit that leptons are well measured by ATLAS. The neutrinos, however, cannot be reconstructed in the ATLAS detector, and therefore, it is not possible to directly measure the mass of the Higgs. Kinematic variables such as the "transverse mass" are used to separate signal from the backgrounds. Though the $H \to WW \to \ell^+ \nu \ell^- \nu$ channel is very useful for measuring the Higgs production cross section, it is poor for measuring the mass of the Higgs, and it provides very weak constraints on the Higgs mass.

Like the $H \to WW$, the $H \to ZZ$ sees a sharp uptick in relative production cross-section when both Z bosons are real (i.e. where $m_H > 2m_Z$). Muons and electrons
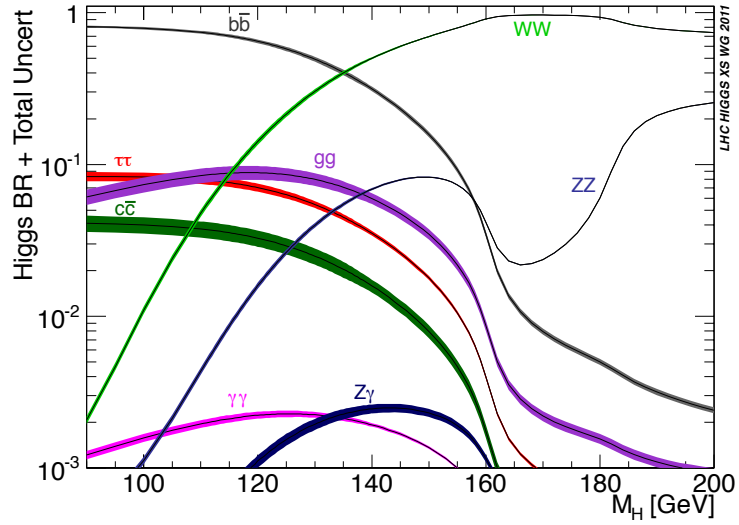
Figure 2.12: The dependence of the Higgs decay branching fraction on the Higgs mass for various decay modes [2].

are very well-measured by the ATLAS detector, and thus, excellent mass resolution can be achieved when both Z-bosons decay to lepton pairs. The other decay channels, in which the Zs decay to some combination of leptons, jets, and neutrinos, are less suited to precise mass measurements.

Although the Higgs cannot couple directly to the massless photon, it is possible for the Higgs to decay to photons through a fermionic loop, as seen in Figure 2.8. This loop of virtual fermions suppresses the decay. Despite a poor signal to background ratio, the shape of the background is very continuous, and the Higgs will appear as a sharp peak on a continuous and falling background. This makes the channel very important when measuring the mass of the Higgs boson.

2.3   Mass of the Higgs Boson

Through radiative corrections, precision measurements of the Standard Model parameters can be used to measure or constrain unknown parameters by performing a global fit that utilizes electroweak precision measurements and theoretical predictions. Before the discovery of the Higgs and including the direct limits from Higgs searches, this procedure was able to constrain the Higgs mass to 120^{+12}_{-5} GeV [19].

Including the mass of the Higgs boson in the global fit over-constrains the electroweak sector of the SM. This over-constraint can be used to check the consistency of the SM. By allowing the measured SM parameters to vary within their statistical and systematic uncertainties, it is possible to perform a global fit. The value of the fitted parameters is then compared to their experimentally measured values and the p-value representing the compatibility of the data with the SM hypothesis can be calculated.

2.4   Width of the Higgs Boson

In the SM, the natural width of the Standard Model Higgs boson can be calculated because all Higgs couplings to fermions and bosons are specified by the mass of the Higgs and the mass of the decay products. Knowing these couplings makes it possible to sum the partial width of each decay mode. As these couplings depend on the Higgs mass, the natural width of the Higgs can be described as a function of the Higgs mass. This dependence is shown for the SM Higgs boson in Figure 2.13. If the Higgs width were measured by experiment to be larger than the SM prediction, it would indicate
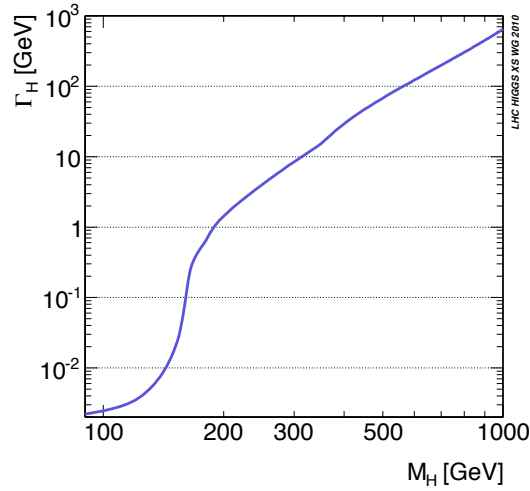
Figure 2.13: Theoretical prediction of the total width of the Higgs boson as a function of the mass of the Higgs boson [1].

the presence of new particles to which the Higgs boson could decay. For this reason, Higgs width measurements can be used to probe the existence of new physics that couples to the Higgs sector.

As will be discussed later, the invariant mass resolution from the ATLAS detector is about 1-2 GeV for a 4-lepton Higgs event. Therefore, the measured limit on the width of the Higgs boson will be near this characteristic resolution. The decay width of the Higgs is around 4 MeV for a mass of 125 GeV. To increase the Higgs width to the GeV-scale, the partial decay width to these new particles must be on the GeV scale.

Chapter 3

The Large Hadron Collider

3.1 Introduction

At the end of the twentieth century, the Standard Model of particle physics was all but complete. Every particle predicted had been observed with the most recent discovery being the top quark, discovered in 1995 at Fermilab. In 2008, a new hadron collider constructed at the European Organization for Nuclear Research (CERN) was inaugurated. This machine, the Large Hadron Collider (LHC), was built to uncover the last piece of the Standard Model: the Higgs boson.

3.2 Specifications

The LHC is a particle collider located near Geneva, Switzerland [20]. It was built in the circular tunnel (26.695 km in circumference) used by the previous generation Large Electron-Positron (LEP) collider. Although the tunnel itself was left

unchanged, the inner workings were changed dramatically. The magnets, radio-frequency (RF) cavities, and other collider apparatus were removed and replaced with state of the art equipment. Figure 3.1 shows a section of the LHC tunnel after the installation of the LHC in the former LEP tunnel. Within the tunnel is a beam-pipe housing the two proton beams, traveling in opposite directions. These are housed side-by-side in a joint casing. An schematic showing this side-by-side configuration is seen in Figure 3.2. To control and focus the beam, a large variety of magnets are used. These range from dipoles to decapoles and each serves a different purpose. The primary steering magnets are the main dipole magnets. These copper-clad niobium-titanium magnets are cooled using liquid helium to 1.9 K and they provide the dipole field of 8.33 Teslas required to curve the proton beams in a circle. Each dipole, seen in Figure 3.2, is 15 m long and weights 35 tonnes. The dipoles are physically built into the beamline with two dipoles adjacent to each other to steer the opposing beams. A total of 1,232 superconducting dipole magnets curve the beam while an additional 392 superconducting quadrupole magnets focus the beam.

To collide the beams, additional magnets are used to bring the two opposing beams together and focus them to converge at the interaction point. The products of the resultant collisions are then measured using the detectors discussed in Section 3.4 that are built around the LHC interaction points.

Though designed for *p-p* collisions with a center of mass energy of 14 TeV and an instantaneous luminosity of 10^{34} cm^{-2}s^{-1}, the currently achieved values are somewhat lower. During LHC Run-1[1], the highest *p-p* center of mass energy achieved was 8 TeV

---

[1]LHC Run-1 corresponds to the 2010, 2011, and 2012 data taking periods at the LHC
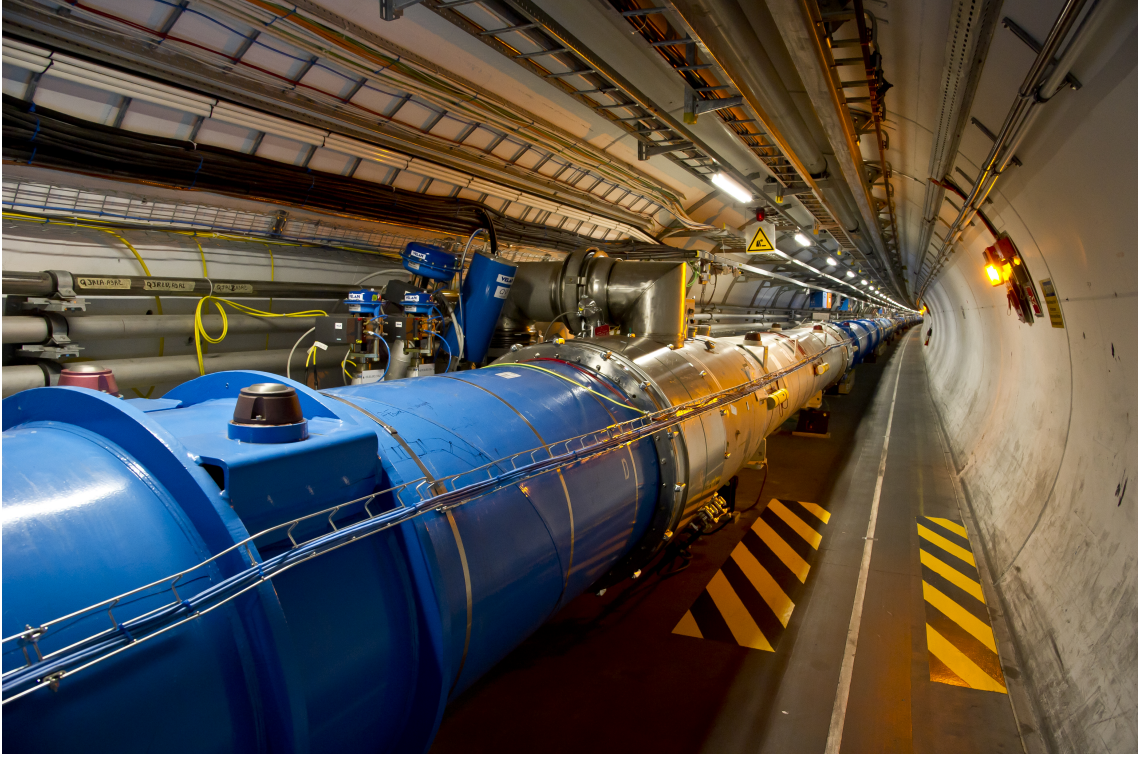
Figure 3.1: A picture of the LHC tunnel showing a section of the beamline. The blue tube on the left is the outside of one of the main dipole magnets.

and the peak instantaneous luminosity obtained was 7.7×10^{33} cm^{-2}s^{-1}. The LHC was designed to collide lead-lead nuclei with a 2.8 TeV per nucleon energy and an instantaneous luminosity of 10^{27} cm^{-2}s^{-1}. The design specifications for the LHC proton beams and the performance achieved in the 2011 and 2012 runs can be found in Table 3.2. The final row in Table 3.2 refers to the maximum (over all runs in a given year) of the mean number of hard scattering events per run. This number is a measure of the "in time pileup" which is defined as the number of hard scattering events that occur in a given bunch crossing. In contrast, the "out of time pileup" refers to the additional collisions from previous bunch crossings that are being recorded simultaneously by the detector.

Table 3.1: Design specifications of the LHC proton beams and the values achieved during the 2011 and 2012 runs [10, 11].

Property	Design Specification	2011	2012
Energy per Beam [TeV]	7	3.5	4
Peak Luminosity [cm^{-2}s^{-1}]	10^{34}	3.7×10^{33}	7.7×10^{33}
Bunches per beam	2808	1380	1380
Bunch spacing [ns]	25	70/50	50
Protons per bunch	1.15×10^{11}	1.45×10^{11}	1.7×10^{11}
β^* [m]	0.55	1.0	0.6
Maximum $\langle N_p \rangle$	19	17	37
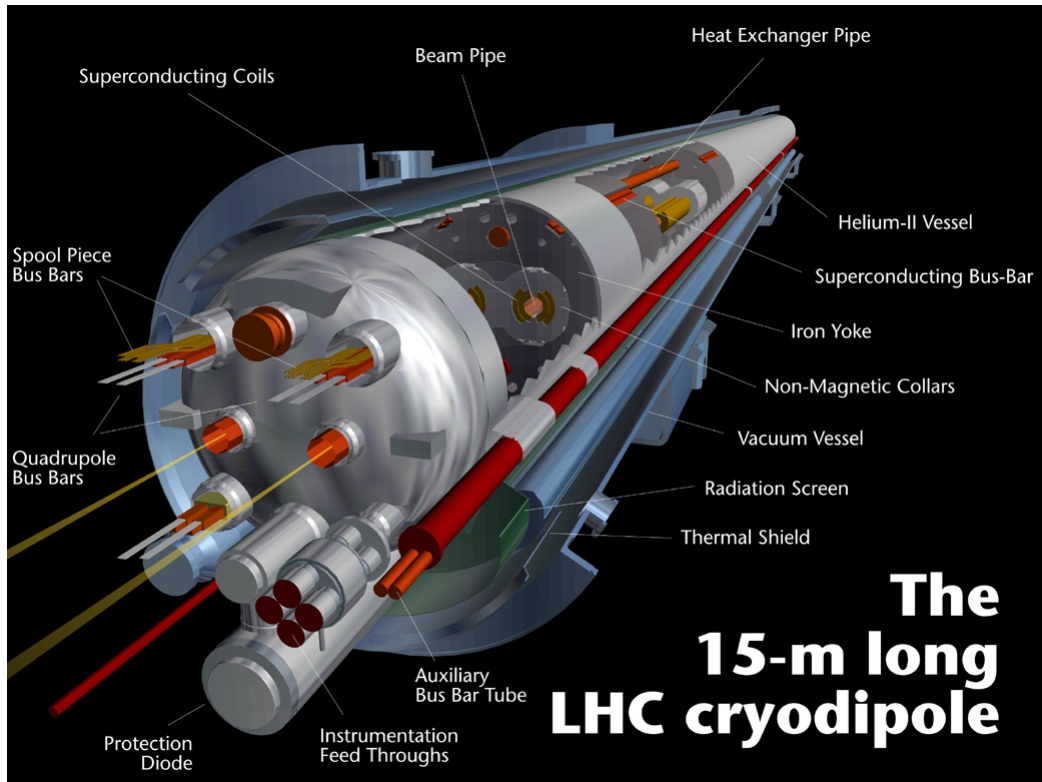
Figure 3.2: A schematic showing the structure of the main LHC dipole magnets.

3.3   Accelerator Complex
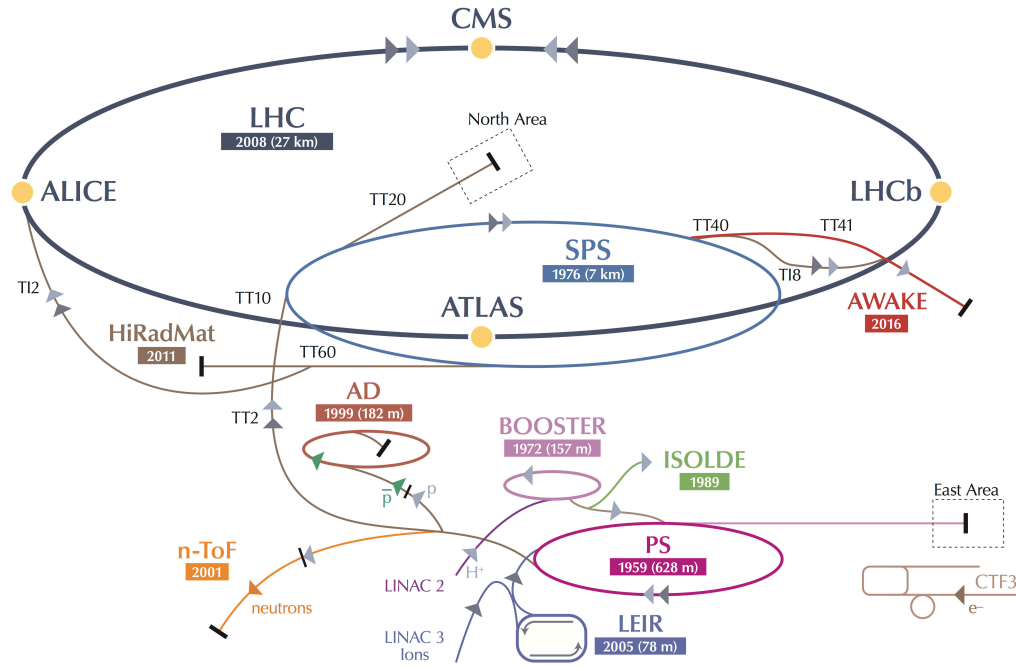
Figure 3.3: A schematic of the CERN accelerator complex with the accelerators labeled.

Figure 3.3 shows a schematic of the CERN accelerator complex. To accelerate protons to 4 TeV a series of linear and circular accelerators are used. The protons start as Hydrogen gas and are accelerated to ~ 50 MeV by a linear particle accelerator, LINAC 2. These are then injected into a small Proton Synchrotron Booster which increases their energy to 1.4 GeV. From here, the protons are injected into the Proton Synchrotron which raises their energy to 26 GeV. After this, they enter the Super Proton Synchrotron (SPS) which produces protons with an energy of 450 GeV. At this stage, the beam can finally be injected into the Large Hadron Collider (LHC) which accelerates the 'beam to its final collision energy. The beams are the collided

resulting in a center of mass energy of 7 or 8 TeV. Collisions with the design center of mass energy of 14 TeV are currently scheduled for the 2015 run.

3.4   Experiments

On the LHC, there are four interaction points that have detectors located at them. These detectors are the ATLAS detector, the CMS detector, the ALICE detector, and the LHCb detector. ATLAS and CMS are general purpose detectors optimized to measure the Higgs, Supersymmetry, and the Standard Model. ALICE is a detector which is specialized to measure heavy ion (Pb-Pb) collisions. LHCb is designed to make precision B-physics measurements. Two additional LHC experiments, LHCf and TOTEM, do not have their own interaction point. Instead they are built around one of the main interaction points, for LHCf, this is ATLAS and for TOTEM, this is CMS. LHCf seeks to measure neutral pions produced at the LHC collisions to gain a better understanding of cosmic rays while TOTEM is designed with detectors at very high pseudo-rapidity, η, to measure the proton-proton interaction cross section and study diffractive physics in the non-perturbative regime of Quantum Chromodynamics (QCD).

Chapter 4

The ATLAS Detector

The ATLAS detector was designed to perform a diverse array of physics measurements using the high luminosity p-p collisions provided by the LHC. A primary motivation was the desire to search for the Higgs boson and, if found, measure its properties. As discussed in Chapter 2, the Higgs boson can decay to a large array of final states. These final states involve a combination of particles including muons, electrons, jets, b-quark jets, and neutrinos. To measure these particles requires high-precision tracking and calorimetry which can operate in the high luminosity environment of the LHC.

The ATLAS detectors must be able to precisely measure the momentum and energy of particles in the presence of high pileup, and the detectors must have good time resolution to determine which bunch crossing the particles originated from. The detectors themselves and their readout electronics must be able to withstand the radiation from the high luminosity LHC collisions for many years before being replaced. The radiation hardness of the detectors is particularly critical in the forward regions

where the particle flux is the highest.

Figure 4.1 shows a three-dimensional representation of this same ATLAS geometry while Figure 4.2 shows a cross-sectional view of the ATLAS detector. Closest to the interaction point is the inner detector (ID) that is intended to provide precise vertexing and tracking for charged particles originating from the interaction point. Beyond the inner detector, there are two layers of calorimetry. The first, known as the electromagnetic (EM) calorimeter, is intended to stop electron and photon showers and measure their energy. The hadronic calorimeter (HCAL), located beyond the electromagnetic calorimeter is designed to measure the energy deposition of hadronic jets. The last component of the detector is the muon spectrometer (MS). Because muons tend to lose only a few GeVs during their transit, most will simply pass through the detector without stopping. To properly measure the momentum of high momentum muons, it is imperative to have a high magnetic field to curve the track and a large distance over which the curvature of the track can be determined. Generally, neutrinos, will pass through the detector without interacting. Their existence can be inferred through the conservation of momentum. Combining tracking and calorimetery is particularly important for the measurement of electrons and jets. The calorimetric resolution scales inversely with the square root of the energy:

$$\frac{\delta E}{E} \propto \frac{1}{\sqrt{E}} \tag{4.1}$$

In comparison, tracking momentum resolution scales linearly with the momentum:

$$\frac{\delta p}{p} \propto p \tag{4.2}$$

For electrons and hadrons, these resolutions complement each other. Low momentum/low energy electrons can be well-measured by the tracking system while high

energy/high momentum electrons will be poorly measured by the tracking but (relatively) well measured by the calorimeter.
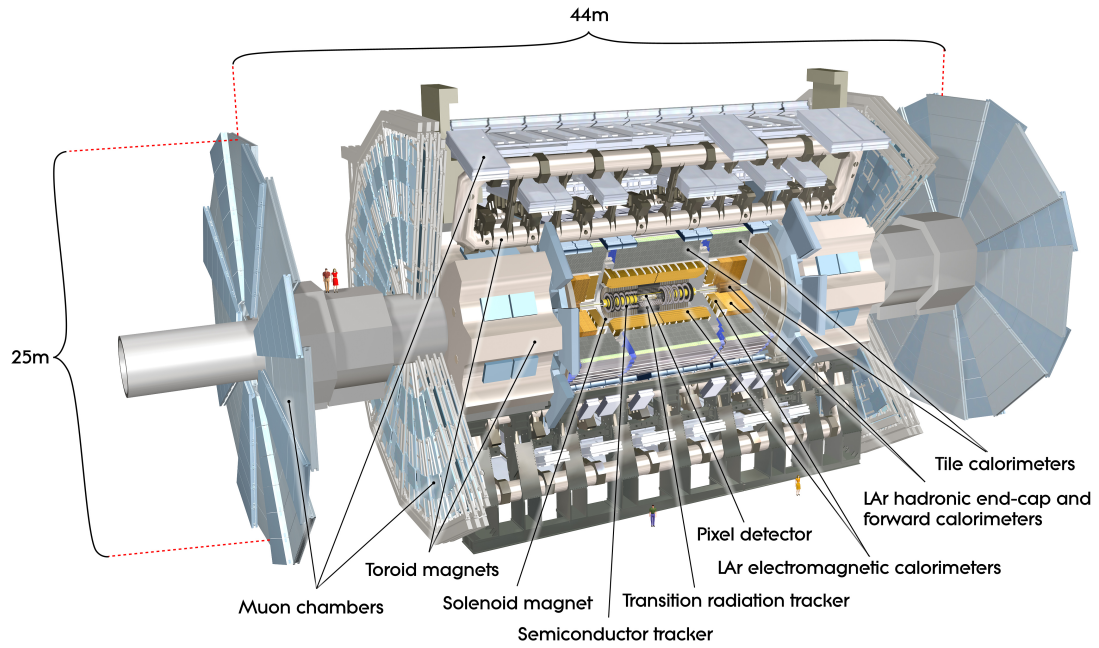
Figure 4.1: A schematic of the ATLAS detector with important detector elements labeled [3].
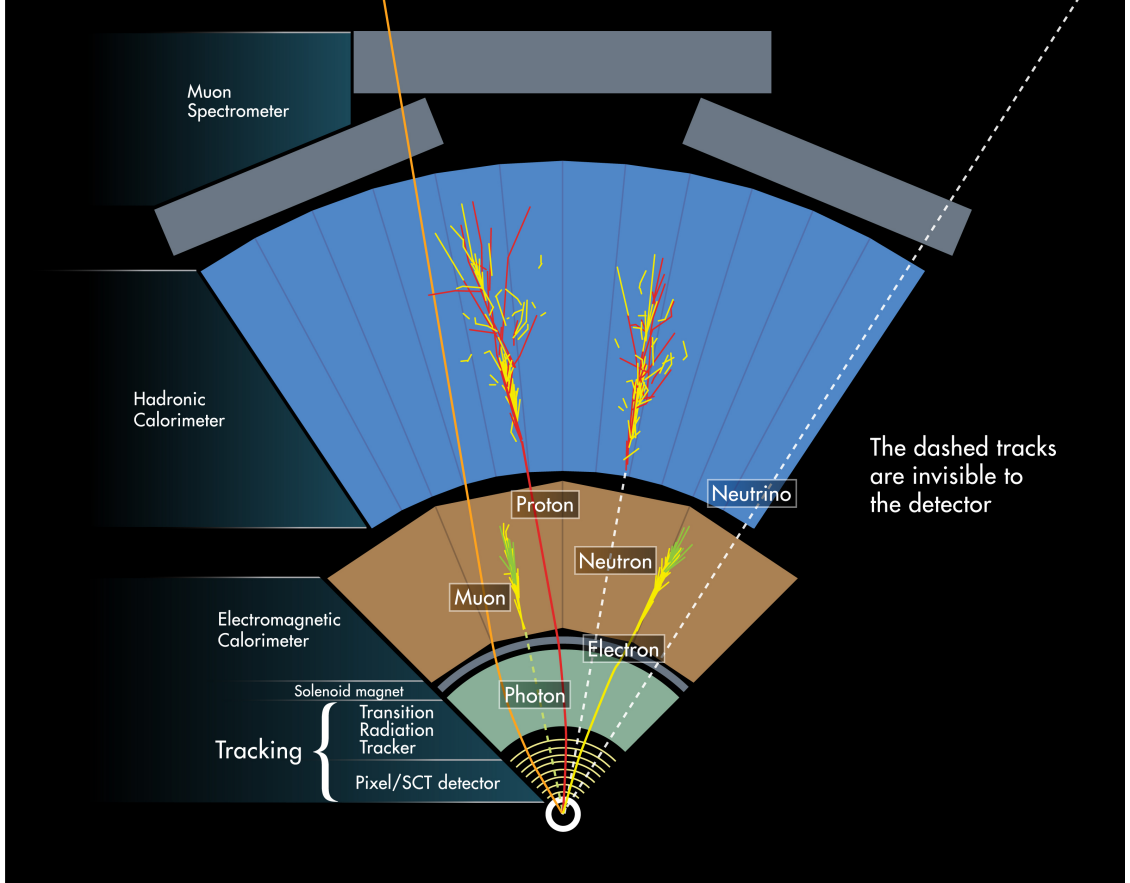
Figure 4.2: A cross-section view of the ATLAS detector showing how different types of particles interact and are measured by the detector.

4.1 Coordinates

In the ATLAS detector, the pseudorapidity is defined by $\eta \equiv -\ln\left[\tan\left(\frac{\theta}{2}\right)\right]$ where θ is the polar angle of the particle; $\theta = 0$ is the direction perpendicular to the beamline, $\theta = \pi/2$ points to the C-side of the detector, and $\theta = \pi$ points to the A-side of the detector. The other angle, ϕ is the azimuthal angle defined to be 0 when pointing toward the center of the accelerator ring. Using these coordinates, the transverse momentum, p_T, and the momentum, p are related by $|p| = p_\mathrm{T} \cosh\eta$. The angular distance between two tracks, ΔR, is defined to be $\sqrt{\eta^2 + \phi^2}$.

4.2   Magnet System

In the high energy regime of the LHC, nearly all particles are moving at speeds indistinguishable from the speed of light. As a result, it is not possible to measure the momentum of these particles by measuring their speed. To determine the momentum, it is necessary to apply a force on them and then measure the effect of that force on their motion. The Lorentz force on a charged particle in a magnetic field is given by:

$$\vec{F} = \frac{d\vec{p}}{dt} = q\vec{v} \times \vec{B} \tag{4.3}$$

There are three separate magnet systems each with their own cooling and cabling. These are the Central Solenoid, the Barrel Toroid, and the End-cap Toroid. The solenoid and toroids bend the charged tracks in the ID and MS respectively making it possible to measure the track momentum. All the magnets are made from aluminum stabilized Cu/Nb/Ti superconducting material and they are kept at 4.5 K using a liquid Helium cryogenic system [3].

4.2.1   Central Solenoid

The ATLAS Central Solenoid provides a 2 Tesla magnetic field [4] [21]. The solenoid is designed to be as thin as possible so as to avoid adding material that could stop particles before they can be measured by the calorimetry system. The solenoid coil has an inner diameter of 2.46 m and an outer diameter of 2.56 m. Axially, the length of the cylinder is 5.8 m. The solenoid is cooled by forcing liquid helium at 4.5 K through tubes welded onto the casings of the coil windings. There are 1154 turns in the solenoid and it operates with a current of 7.73 kA. This leads to a stored energy

of 40 MJ. Because the solenoid creates an axial field pointed along the beam-line, a charged particle moving transverse to the beam-line will be bend in the ϕ-plane. The magnetic field lines return through the steel in calorimeters.

4.2.2 Muon Spectrometer Toroids

The ATLAS barrel toroid is composed of eight separate air-core toroid elements as seen in Figure 4.3 [4,22]. These start radially at 9.4 m and end at 20.1 m. Axially, the barrel toroid is 25.3 m long. The peak magnetic field provided by the barrel toroid is 3.9 T due to a 20.5 kA current in the coils. This yields a stored energy of 1080 MJ.
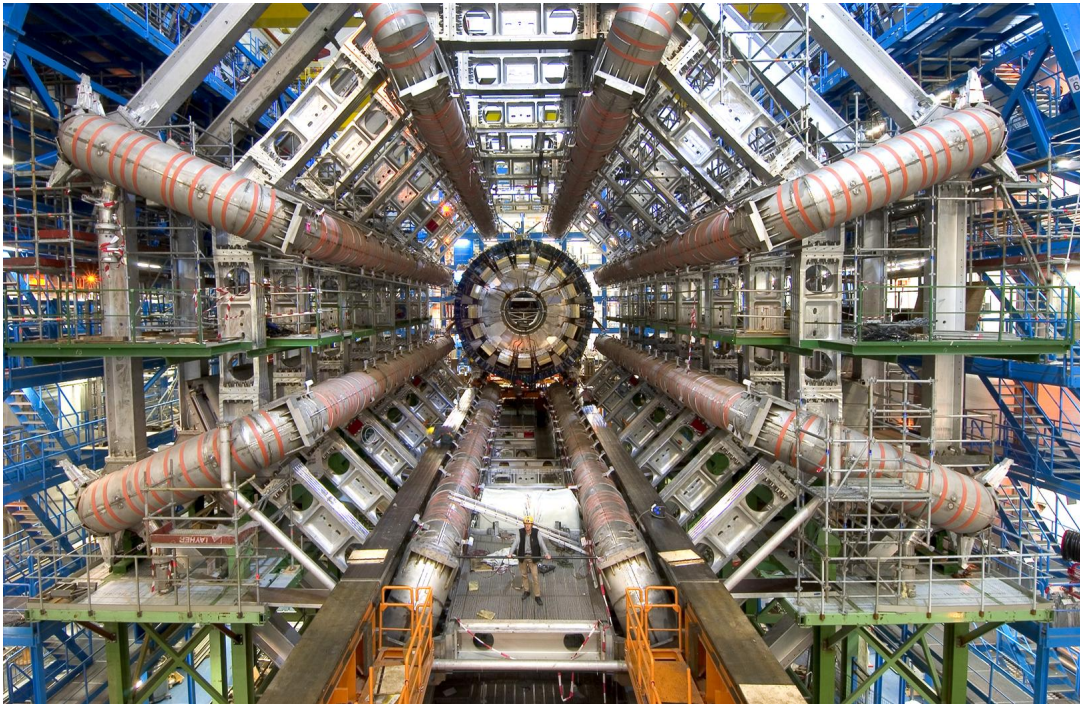
Figure 4.3: A photo of the barrel toroid installed in the ATLAS underground cavern. The eight barrel toroid coils are visible; each is encased in a stainless-steel vacuum structure. The entire assembly is held in place by eight inner and eight outer rings of struts. The temporary scaffolding and green platforms were removed after installation [4].

Each of the two ATLAS end-cap toroids consists of eight coils [4]. They are housed in an aluminum alloy casing. The inner diameter of the end-cap torroid is 1.65 m and it extends up to 10.7 m. The operating current is 20.5 kA leading to a peak field of 4.1 T and a stored energy of 250 MJ in each end-cap torroid.

The expected magnetic field integral for the ATLAS toroid is used to evaluate the bending power of the field. This field integral is shown in Figure 4.4. There is good magnetic field coverage up to $|\eta| < 2.6$. The regions with low magnetic field, $1.4 < |\eta| < 1.6$, correspond to the area where the fringe field from the barrel and end-cap cancel the bending power of each other [4]. The measurement of the muon momentum in this region tends to degrade.
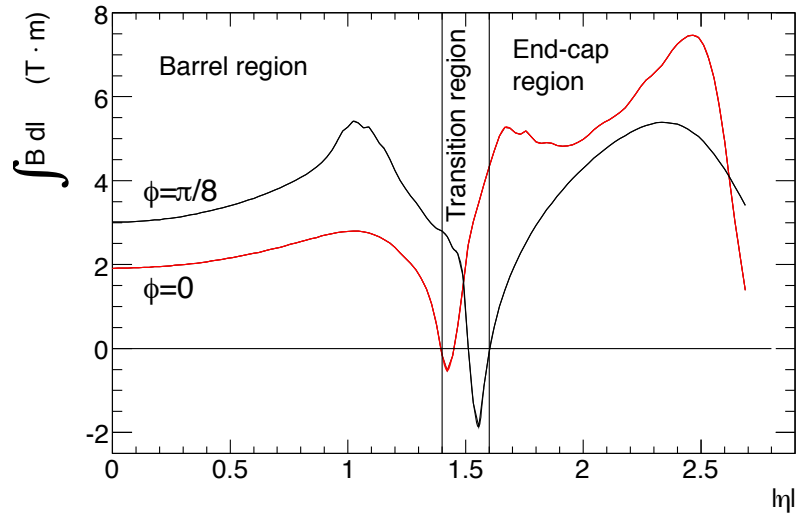
Figure 4.4: The predicted field integral as a function of $|\eta|$ from the innermost to the outermost MDT layer in one toroid octant. The field assumes perfectly straight tracks. The black curve shows the field integral at $\phi = \pi/8$ and the red curve shows the field integral at $\phi = 0$.

4.3   Inner Detector

The ATLAS inner detector consists of multiple sub-detectors which work together to measure the momentum of charged particles [4, 23, 24]. Energy loss profiles and the track curvature can be combined to determine the particle identity. The three components of the ID are the Pixel layer, the Semiconductor Tracker (SCT), and the Transition Radiation Tracker (TRT). Figure 4.5 shows the acceptance and layout of the various ID components. A schematic of the ID layers is seen in Figure 4.6.
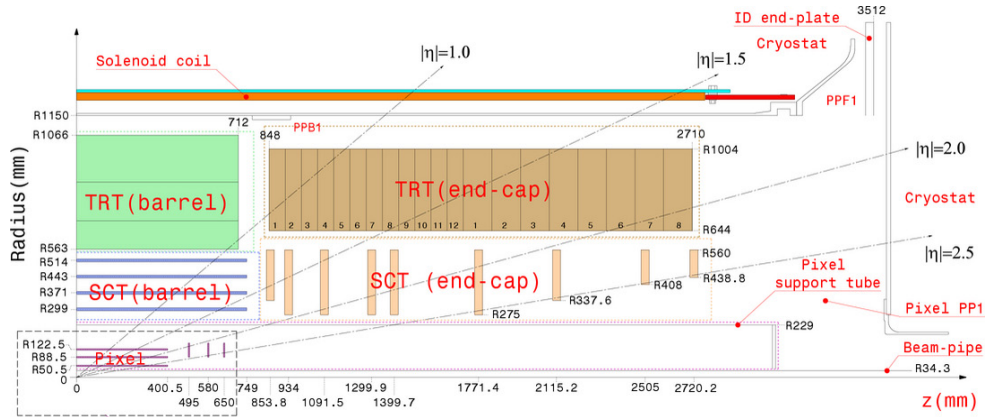
Figure 4.5: A schematic quarter-section view of the ATLAS inner detector. The major inner detector components are labeled. Straight lines show the pseudorapidity coverage of various detector components.

R = 1082 mm

TRT

R = 554 mm
R = 514 mm

R = 443 mm

SCT

R = 371 mm

R = 299 mm

TRT

SCT

R = 122.5 mm
Pixels · R = 88.5 mm
R = 50.5 mm

R = 0 mm

Pixels
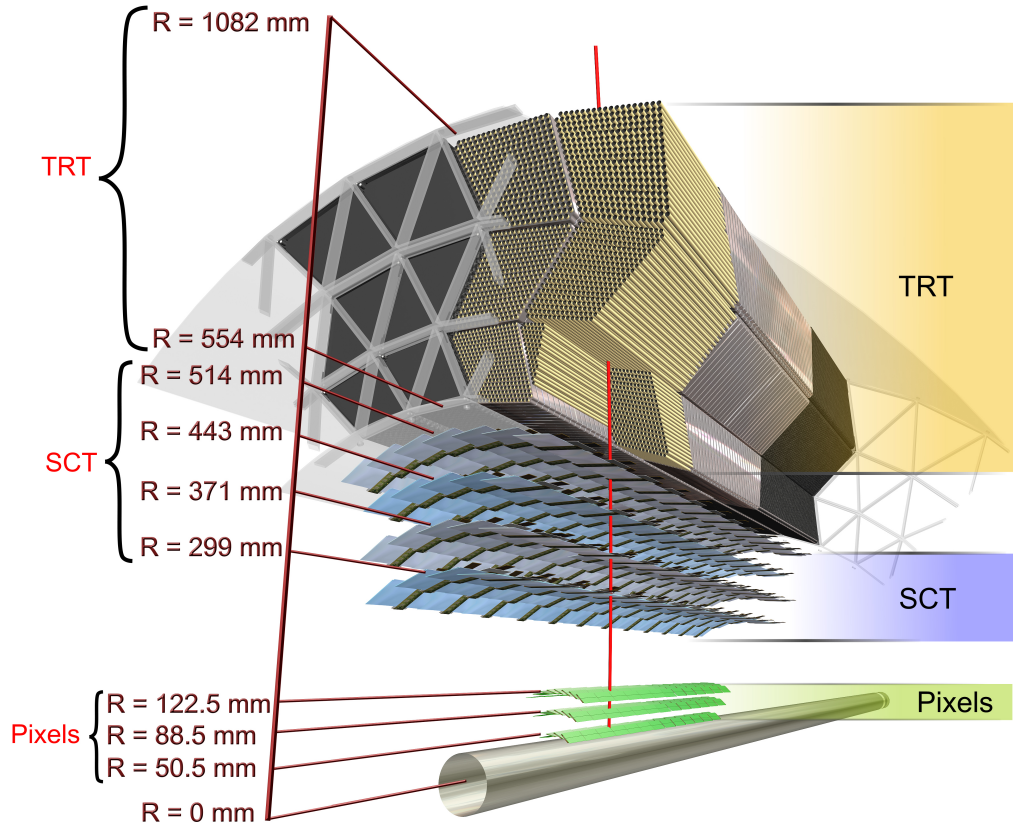
Figure 4.6: A schematic of the ATLAS Inner Detector detector with sub-detector components labeled. The red line represents the trajectory of a charged particle with $p_\mathrm{T} = 10$ GeV and $\eta = 0.3$. This track is shown traversing the beryllium beam-pipe, the three silicon pixel layers, the four cyllindrical double layers of the barrel SCT, and approximately 36 axial straws in the TRT.

4.3.1 Pixel Detector

The first component of the ID is the pixel detector. The pixel detector is designed to provide high-precision measurements of tracks close to the interaction point. The pixel detector consists of three layers in the barrel and three disks on both the A and

the C side. The layers are parallel to the beam-line while the disks are perpendicular. This is to ensure that every particle with $|\eta| < 2.5$ will pass at least three pixel layers. The majority of the pixels are 50 μm $\times$400 μm in size while 10% are slightly larger. The pixels are made from 250 μm thick planar silicon. Groups of 47,232 pixels are formed into sensor modules, each 64.4 mm by 24.4 mm [4]. The pixel modules are tilted at an angle to provide overlaps so that tracks will pass through each pixel layer. In total, there approximately 80.4 million readout channels in the pixel detector and the readout time is less than 25 ns to avoid out of time pileup from the tracks resulting from different bunch crossings. A three-dimensional schematic showing the layout of the pixel detector is found in Figure 4.7 [3, 24].
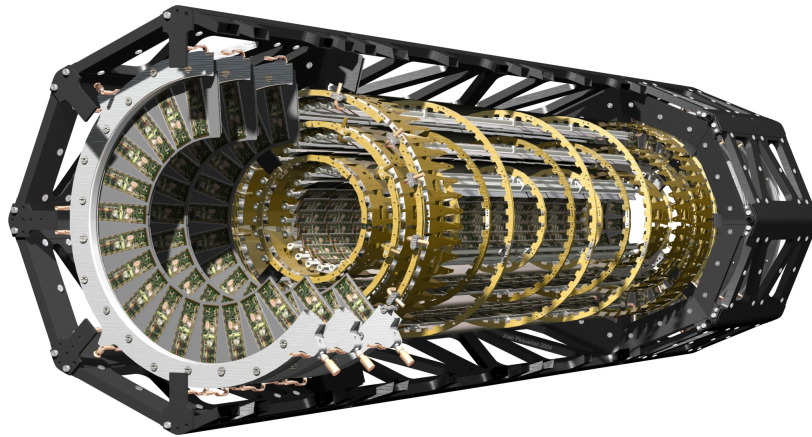
Figure 4.7: A three-dimensional view of the Pixel detector from the ATLAS Inner Detector.

4.3.2 Semiconductor Tracker Detector

The semiconductor tracker is designed to provide additional precision measurements of the charged tracks [3,24]. To this end, the SCT consists of four barrel layers

parallel to the beam-line and nine transverse rings. This geometry is to ensure that every track with $|\eta| < 2.5$ should pass through at least 4 layers in the SCT as seen in Figure 4.5. The SCT detectors themselves are silicon strip detectors using the classic single-sided p-in-n technology with AC-coupled readout strips. The thickness of the detectors is around 285 μm [4]. In the barrel they have a pitch of 80 μm and in the disks the pitch ranges between 56.9 and 90.4 μm. To obtain a second coordinate each SCT layer consists of two semiconductor planes. The strips are placed at a small 40 mrad angle rather than at an orthogonal orientation with respect to each other. This leads to an intrinsic spatial resolution in the barrel of 17 μm in the $r\phi$ plane and a far worse resolution of 580 μm in the z plane. For the disks, this is again 17 μm in the $r\phi$ plane and 580 μm in the r-plane. In total, the SCT detector has 15,912 sensors. Improving the resolution in the $r\phi$ plane at the expense of the z and r planes is done because the magnetic field in the ID curves the tracks in the ϕ direction as discussed in Section 4.2; thus to obtain a precise momentum measurement, it is necessary to have precision measurements of the curvature in the $r\phi$ plane. As with the Pixel detector, the SCT readout time is less than 25 ns to differentiate hits from different bunch crossings.

4.3.3   Transition Radiation Tracker

Unlike the other detector systems in the ID, the transition radiation tracker is not silicon based [3, 4, 24]. The TRT contributes significantly to the ID momentum measurement because it provides a large number of measurements (typically 36 per track) and a longer measured track length than the silicon detectors. Additionally,

when relativistic charged particles pass through the boundary between materials with different dielectric constants, they emit transition radiation. This radiation knocks electrons free in the gas which then cascade producing an ionization proportional to the energy loss. This dE/dx measurement allows for improved particle identification. The gas in the drift-tubes is composed of a mixture of 70% Xenon, 27% CO_2, and 3% O_2 gas. At the center is a 31 μm diameter tungsten wire plated with 0.5-0.7 μm of gold. The central wire is the anode and is kept at ground potential. Meanwhile the walls of the tubes are used as the cathode. The walls are made of polymide film layers that are bonded to each other. This material is chosen for its good electrical and mechanical properties and to minimize the wall thickness. The cathodes are operated at around -1530 V. Typically the time it takes for all the electrons to drift to the anode readout is around 50 ns. The drift time can be converted to a drift radius using a calibration function. Using these drift radii, reconstruction algorithms can determine the most likely track passing through all tubes which were hit. As seen in Figure 4.5, the TRT has three components: the barrel and two end-cap modules (one for side A and one for side B). In total, the TRT system contains almost 300,000 straws and has good coverage for $|\eta| < 2.0$. The typical spatial resolution is ~130 μm per straw.

4.4 Calorimetry

In ATLAS various calorimeters are used to measure the energy of electromagnetic and hadronic showers. These can be categorized as electromagnetic and hadronic calorimeters and each has a barrel and end-cap component [3, 4]. The electromag-

netic calorimeter is located just outside the central solenoid. This calorimeter is made of lead and liquid argon (LAr) and extends to $|\eta| < 3.2$. It is intended to measure the energy of electromagnetic showers. Beyond it, there is the hadronic calorimeter. In the barrel, the hadronic calorimeter uses iron as the absorbing medium to develop the shower and polystyrene scintillating tiles as the active material to measure the energy while in the end-caps a liquid argon technology is again used. Liquid argon based forward calorimeters, which measure both electromagnetic and hadronic showers, extend the calorimeter coverage to $|\eta| < 4.9$. Figure 4.8 shows a diagram of the ATLAS calorimeter system.
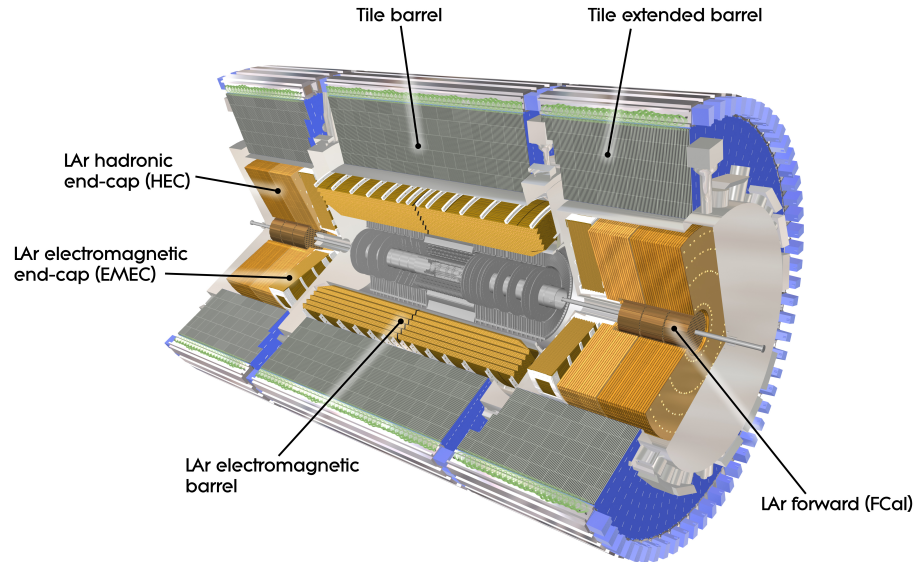
Figure 4.8: A three-dimensional model of the ATLAS hadronic and electromagnetic calorimeter.

4.4.1 Electromagnetic Calorimeter

The ATLAS electromagnetic calorimeter causes electrons, positrons, and photons to shower and then measures the energy contained in those showers [3, 4, 25]. Electromagnetic particles shower through two primary processes: pair-production and bremsstrahlung. Pair-production occurs when a photon produces a positron and an electron. Pair-production must occur before a photon can shower. Once there are charged particles in the shower, bremsstrahlung can occur. Bremsstrahlung is when a charged particle is deflected by the electric field of an atom and emits a photon. These photons can then pair-produce and the cycle starts over.

The EM calorimeter is divided into two parts: the barrel region from $|\eta| < 1.475$ and the end-cap region $1.375 < |\eta| < 3.2$. The detector itself uses liquid argon as the active medium, Kapton electrodes, and lead absorber plates in an accordion shape (see Figure 4.9). Because liquid argon is used as the active medium, the subsystem is very radiation hard but the ability to withstand radiation comes at the price of slow signal processing due to the long time it takes ionization to be read out in the liquid argon medium. The dense materials in the EM calorimeter will help to contain all but the most energetic electromagnetic showers. In the barrel, the calorimeter is between 22 and 30 radiation lengths (X_0) thick while in the end-cap it is between 24 and 33 X_0 thick.

Figure 4.9 shows a schematic of the liquid argon EM calorimeter system which is composed of three layers. The first layer is known as the pre-sampling layer. The presampling layer is necessary because a substantial amount of material exists prior to the EM calorimeter. This presampler uses highly-segmented layers (in η) to determine

the shower shape and estimate the showering which occurred prior to entering the calorimeter. The presampling layer is 4.3 radiation lengths thick and cells in the presampling layer have an angular size of $\Delta\phi \times \Delta\eta = 0.0031 \times 0.098$. The second layer comprises the bulk of the EM calorimeter. It is around 16 radiation lengths thick and the angular dimensions of the cells are $\Delta\phi \times \Delta\eta = 0.0245 \times 0.025$. The last layer of the calorimeter is used to identify EM-showers which punch-through into the hadronic calorimeter. This layer ranges in thickness between 2 and 12 radiation lengths and it has the most coarse angular cell size with $\Delta\phi \times \Delta\eta = 0.0245 \times 0.05$.
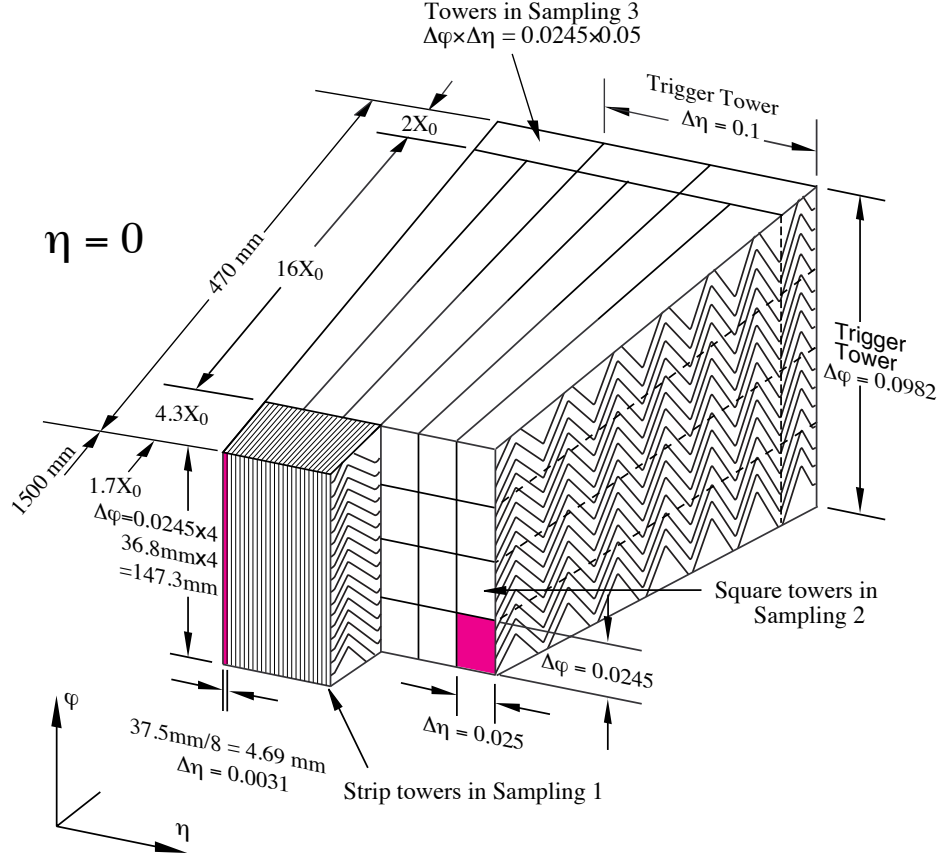
Figure 4.9: A schematic of the LAr barrel accordion geometry. Different layers are delineated and the granularity of the cells in η and ϕ is shown. [4].

4.4.2   Hadronic Calorimeter

The hadronic tile calorimeter covers the barrel region of the ATLAS detector, $|\eta| < 1.7$. The tile calorimeter is divided into two regions, the barrel and the extended barrel. The barrel cylinder region provides coverage until $|\eta| < 1.0$. At this point, there is a vertical space to provide room for services required by the ID and EM calorimeter. The extended barrel provides coverage of the region $0.8 < |\eta| < 1.7$.

In both, steel is used as the absorber while polystyrene scintillating tiles are used as the active material. Each of the tiles are 3 mm thick and they are surrounded by steel. The ratio of steel to scintillator is 4.7 to 1 by volume. The scintillating tiles are read out by wavelength shifting fibers into photomultiplier readouts. This layout can be seen in Figure 4.10. The stopping power of the calorimeters is measured using the "interaction length," λ, which is defined as the mean distance required to reduce the number of relativistic charged particles in a hadronic shower by a factor of $1/e$. The barrel tile calorimeter is segmented into three layers which are 1.5, 4.1, and 1.8 interaction lengths respectively. These start at an inner radius of 2.28 m and extend to 4.25 m. The extended barrel is similarly segmented into three layers of 1.5, 2.6, and 3.3 interaction lengths.

The hadronic end-cap calorimeter utilizes liquid-argon as the active medium. It is comprised of two independent wheels, one in each end-cap. These are physically located behind the end-cap EM calorimeter and the cooling cryostats are shared between the two systems. The HEC is built so that it extends to $|\eta| = 3.2$ in order to overlap with the forward calorimeter discussed in the next section. The wheels closest to the interaction point are constructed from copper plates 25 mm in thickness. Those further away are constructed from copper plates 50 mm in thickness. The inner radius of these plates is 0.475 m while the outer radius is 2.03 m. The copper plates are interspaced with gaps filled with liquid argon which comprises the active medium for the calorimeter.
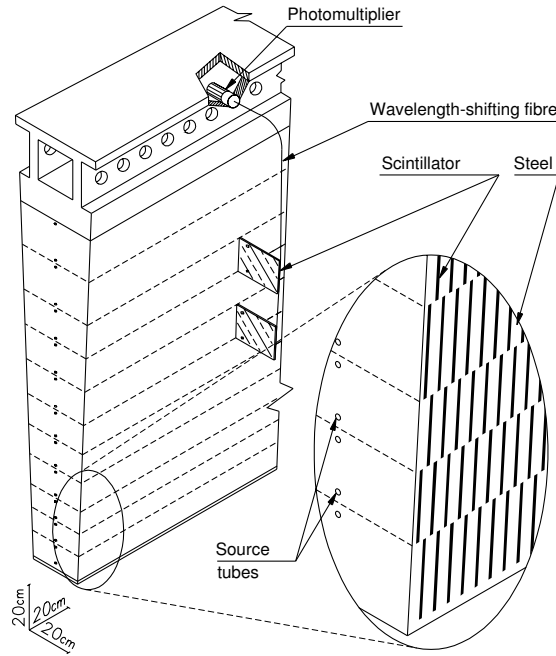
Figure 4.10: A schematic showing the integration of the mechanical assembly and the optical readout of the scintillator in the tile calorimeter. Each tile has holes, 9 mm in diameter, intended for stainless-steel tubes that house the radioactive source calibration system [4, 5].

4.4.3 Forward Calorimeter

The last component of the calorimeter is the forward calorimeter (FCal) [4]. This region has particular challenges because the forward region is exposed to very high levels of radiation. The forward calorimeter uses liquid argon as the active material and is separated into three regions. The first one is made from copper and liquid argon and is dedicated to EM calorimetery while the next two are made from tungsten and liquid argon and are more specialized for hadronic calorimetry. In total, the forward calorimeter is 10 interaction lengths deep. The layout of these calorimeters can be seen in Figure 4.11.

In each of these sections, the calorimeter is composed of a metal matrix with
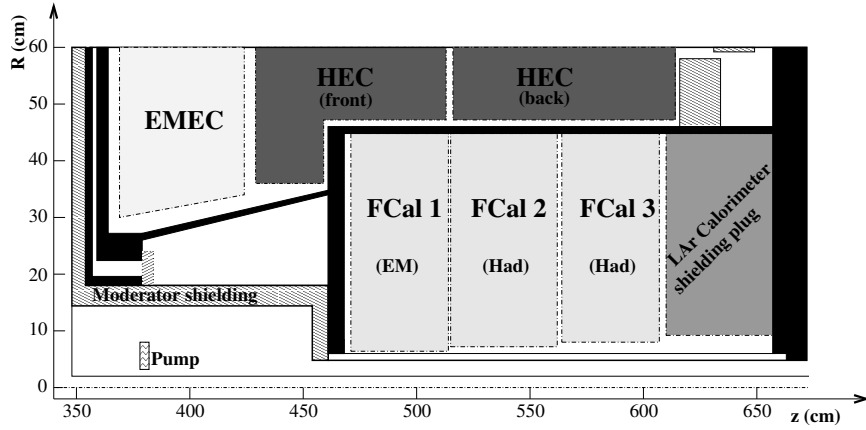
Figure 4.11: A schematic diagram showing the three FCAL models and the EM and Hadronic end-cap calorimeters. The material in front of the FCAL and the shielding behind it are also visible. Black regions are structural parts of the cryostat.

regularly spaced channels with concentric rods and tubes. The tubes function as the ground while the rods themselves are held at high voltage. The liquid argon in the gap between the rods and tubes is the active material. Figure 4.12 shows the structure of the rods and tubes in the first layer of the forward calorimeter that is dedicated to EM calorimetry [3, 25]. The Molière radius represents the characteristic transverse size of an EM shower. It is defined to be the cylindrical radius within which 90% of the shower energy is deposited. In Figure 4.12, the Molière radius is represented by the pink circle for reference.
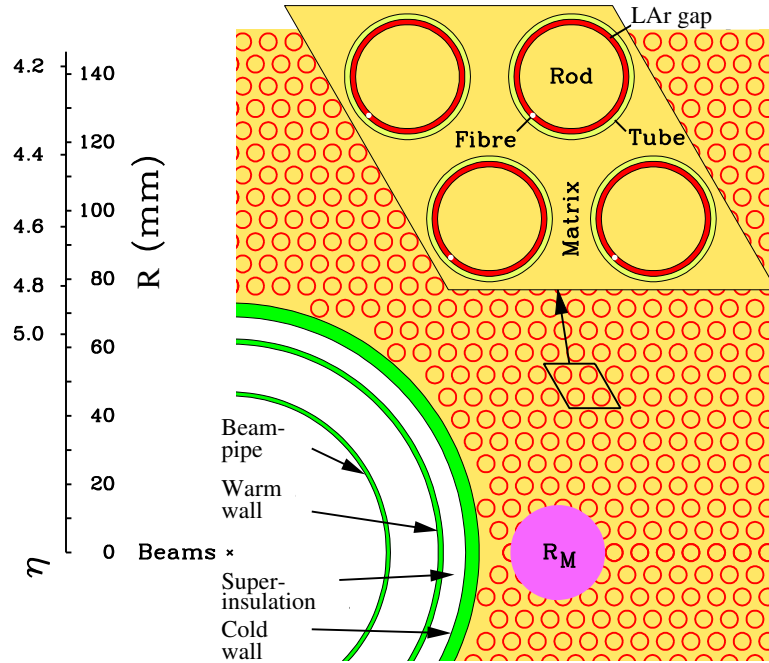
Figure 4.12: Schematic showing the electrode structure of the FCAL1 with the matrix of copper plates, copper tubes, and rods. The gap is filled with the active medium, LAr.

4.5   Muon Spectrometer

Because muons tend to pass through the detector without stopping, the only way to measure the muon momentum is by measuring the curvature of the muon track in a magnetic field [3, 4, 26]. As the strength of the magnetic field increases, the curvature of the track will increase thereby improving the momentum measurement. Of course, it is important that the actual trajectory be well measured. To measure the trajectory of muons, ATLAS uses precision chambers: gas-filled muon drift-tubes (MDTs) and cathode strip chambers (CSCs). Because MDTs have a very slow readout time compared to the bunch crossing rate, a faster triggering system is necessary to specify which, if any, drift-tubes should be read-out for a given bunch crossing. This

triggering system is comprised of faster gas-filled chambers known as the resistive plate chambers (RPCs) and the thin gap chambers (TGCs). As seen in Figure 4.13 there are layers of MDTs sandwiched by RPC or TGC triggering layers. In the barrel, these MDT layers are parallel with the beam-line. In the end-cap, the MDT layers are perpendicular to the beam. In the very forward region, MDTs are replaced by the CSCs. Within the barrel, the RPCs are used as the triggering elements and they are placed around the MDT chambers so that muons will pass through three RPC layers. In the end-cap, the TGCs are used as the triggering layers and they are positioned so that most muons will pass through three TGC layers.
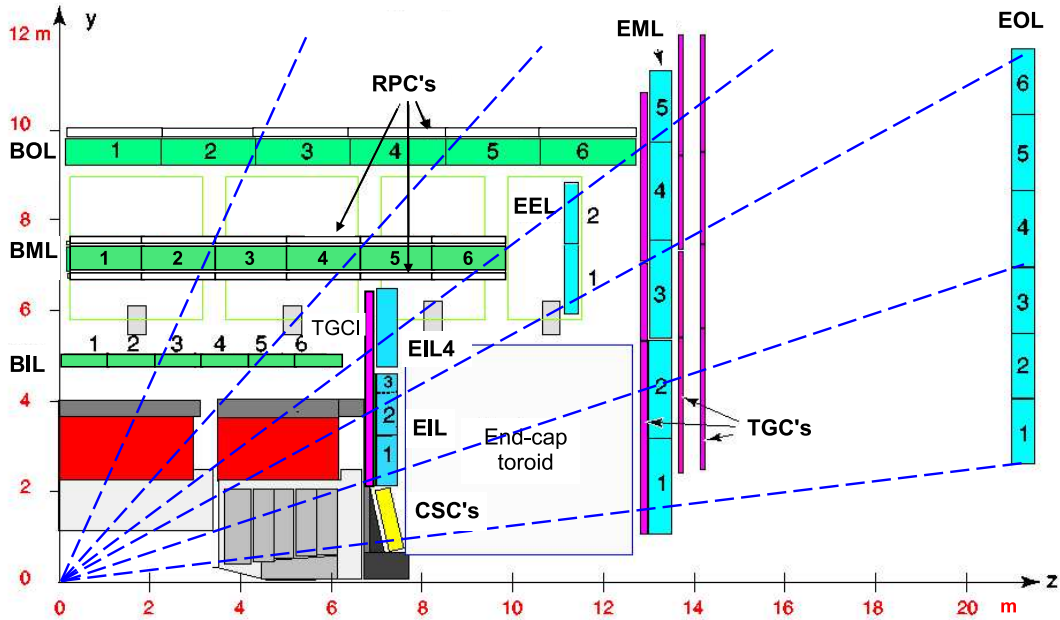
Figure 4.13: A cross-section view of the ATLAS muon spectrometer in a plane containing the beam axis (bending plane). Muons of infinite momentum would propagate unbent by the magnetic fields in straight trajectories illustrated by the dashed lines. Typically these muon tracks will traverse three muon stations [4].

4.5.1   Muon Drift Tubes

The MDT tubes, shown in Figure 4.14, are 29.970 mm diameter aluminum tubes with a 50 μm diameter central Tungsten-Rhenium wire. This wire is held at an operating potential of 3080 V. The gas in the tube is a mixture with 93% Argon and 7% CO_2. When a charged particle passes through, it ionizes the gas. The displaced electrons then drift toward the central wire (the anode) producing a signal. The measurement of the drift time makes it possible to measure how far away from the wire the ionizing particle passed. In the case of the MDTs, the maximum drift time is $\sim$ 700 ns.
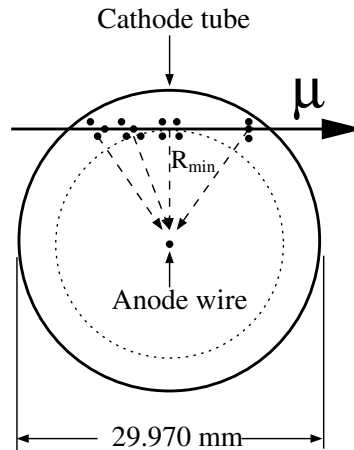
Figure 4.14: A cross-section view of a MDT tube. The anode wire is held at 3080 V while cathode tube is held at ground. In the figure, a muon is shown passing through the tube. The black dots represent the displaced electrons which then drift to the anode wire [4].

The physical layout of the MDT chambers can be seen in Figure 4.15. A single MDT chamber is typically between 1 and 6 meters in length and 1 to 2 meters in width. Each chamber has two multi-layers, each of which is three or four tube layers deep. These are joined together using an epoxy glue. The two multi-layers are

separated by three mechanical spacers. This structure is shown in Figure 4.15. In the figure, the HV side represents where the high voltage is supplied while the RO side is where the drift tubes are read out.
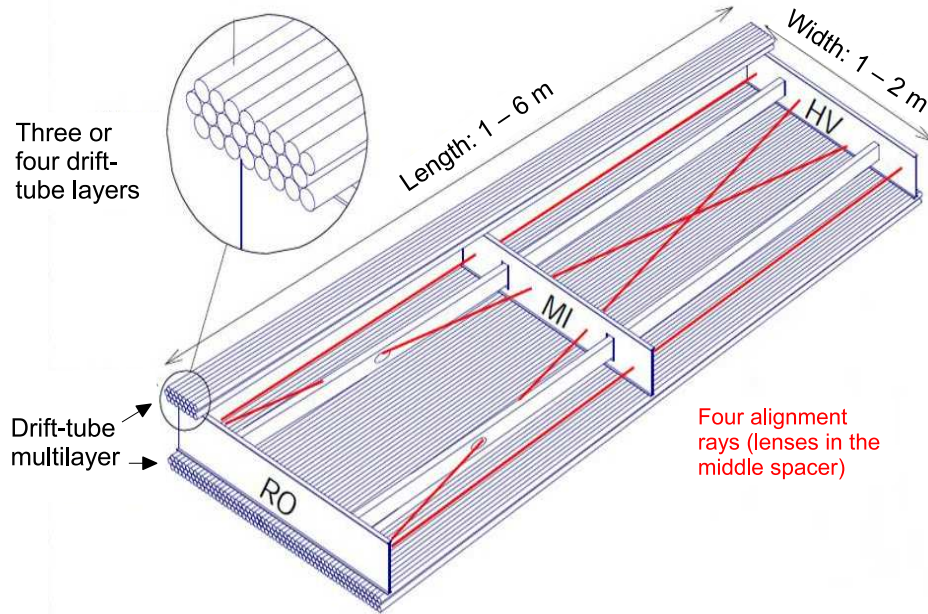
Figure 4.15: A diagram showing the physical structure of an MDT chamber. The three spacer bars (labeled RO, MI, and HV) are connected by longitudinal beams. RO designates the location of the signal readout and HV designates the location of the high voltage supply. The red lines show the optical alignment rays which are used to monitor the internal geometry of the chamber [4].

In total, the ATLAS muon system has 370,000 MDT tubes which are grouped into 1194 chambers. This covers a total area of 5500 m^2 [3, 26].

4.5.2 Cathode Strip Chambers

The CSCs are the MDT counterpart for the very forward region of the muon spectrometer ($2 < |\eta| < 2.7$) [3, 4, 26]. Unlike the drift tubes in the MDTs, the CSCs are multiwire proportional chambers that use a cathode strip to readout signals. A

schematic showing this layout is found in Figure 4.16. The cathodes are segmented strips. One set of strips are perpendicular to the anode wires providing the precision coordinate while the other set runs parallel to the wires and provides the transverse coordinate.
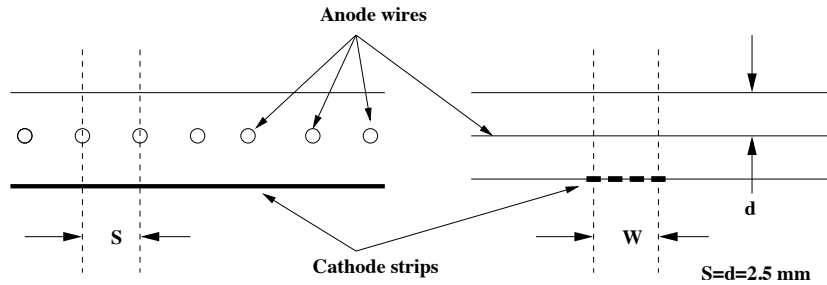
Figure 4.16: A schematic of the CSC detector showing the anode wires and the cathode readout strips. This view shows the structure of the CSC cells when looking down the wires. The wire pitch s is equal to the spacing between the anode and cathodes, d [4].

The distance between the anode wires is 2.5 mm and the distance between the anode and cathode is also 2.5 mm. The wires themselves are gold plated tungsten with a small component of rhenium 30 μm in diameter. The gap between two cathode strips is 0.25 and the strip widths are 1.519 mm and 1.602 mm for the large and small chambers respectively. One out of every three strips is connected to the readout electronics which measure the charge induced on the strips. The gas used in the CSCs is a mixture of 80% Ar and 20% CO_2. The anode wire is held at an operating voltage of 1900 V. The gas gain from this configuration is 6×10^4 and the typical ionization from a normal track is 90 ion pairs. The resulting drift time is generally 40 ns or less which gives a timing resolution of about 7 ns per plane. This small drift time is critical in the forward region because of the high particle flux and background conditions in these areas. As the CSCs are limited to the forward regions of the

49

ATLAS muon spectrometer, there are only 32 CSC chambers and 30,720 readout channels.

4.5.3   Resistive Plate Chambers

The RPCs are a gaseous detectors which function as the trigger for the barrel of the muon subsystem. Their coverage extends to $|\eta| = 1.05$ and there are 606 RPC chambers in total. As shown in Figure 4.17, two of the RPC chambers are located on the top and bottom of the middle MDT layer. The third RPC chamber is located below the outer MDT layer. Individually, the RPC chambers are comprised of two independent detector layers, known as gas volumes. Each gas volume is composed of two parallel resistive plates made from plastic laminate with a 2 mm gas-filled gap in between. The plates themselves are 2 mm thick and coated with a thin graphite layer. The distance between the gap is maintained by a series of insulating spacers. The gas used in the RPCs is 94.7% $C_2H_2F_4$, 5% Iso-$C_4H_1 0$, and 0.3% SF_6. Unlike the drift tubes, the RPCs operate in avalanche mode using a high operating voltage of 9.8 kV. On either side of the resistive plates are metal pick-up strips with a width of 25 to 35 mm. These are insulated from the graphite electrodes by means of thin Polyethylene Terephthalate films that are glued to the graphite surface. The strips on the top and bottom of the gas volumes are orthogonal to each other making it possible to measure the η and ϕ coordinates. In Figure 4.18, a cross-sectional view of the RPCs is shown. Two units are joined to form a chamber, each of these units is comprised of two gas volumes supported by spacers. Paper honeycomb reinforces the gas volumes.

Operating in avalanche mode, the RPCs have very good time resolution producing signals with a time jitter less than 10 ns after including the strip propagation time.
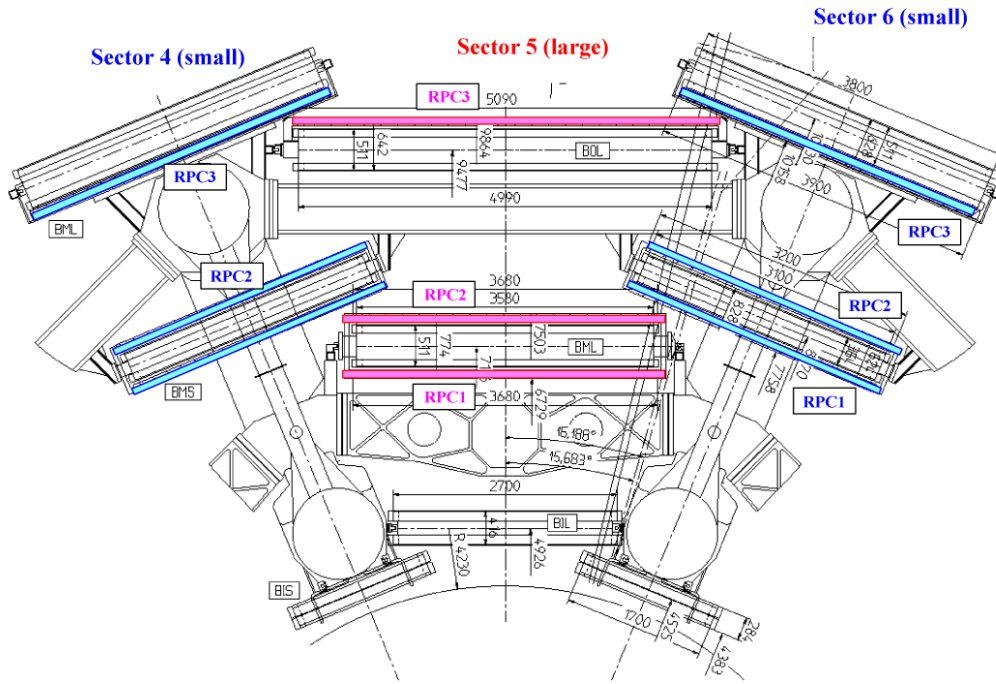
Figure 4.17: Cross-sectional view showing the position of the RPC chambers around the MDT chambers. There are two RPC layers around the middle MDT chambers and on RPC chamber below the outer MDT chambers.
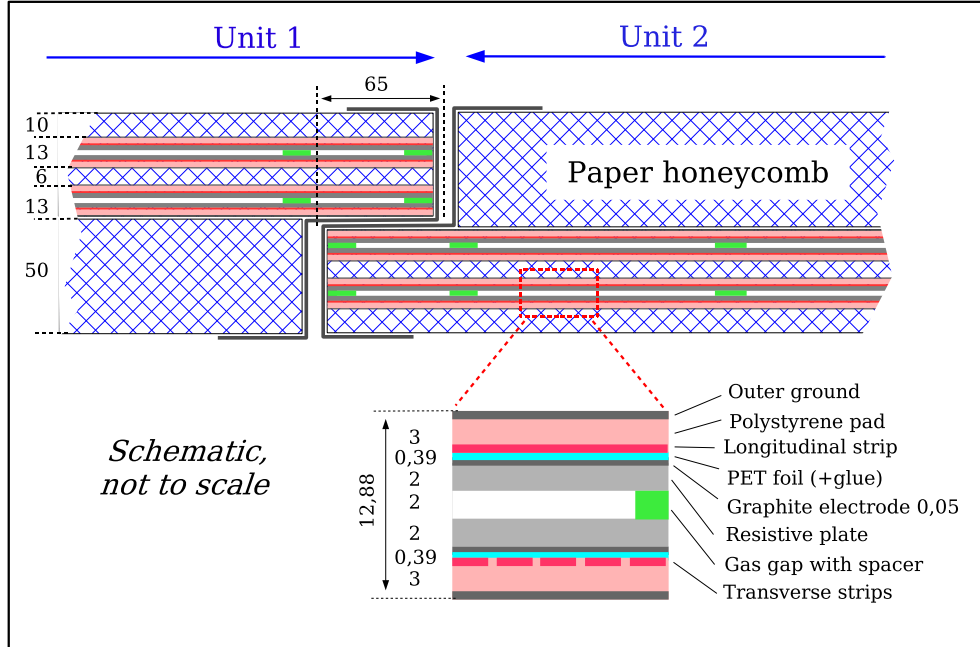
Figure 4.18: Cross-sectional view of an RPC chamber. Visible are two units that have been joined to form a chamber. Each unit has two gas-volumes supported by spacers (shown in green). The readout strips, colored dark pink, are shown: the longitudinal strips are on top of the gas volume and the transverse trips are on the bottom.

4.5.4 Thin Gap Chambers

Like the RPCs, the thin gap chambers provide the triggering elements in the end-cap region of the muon spectrometer and an additional azimuthal coordinate to complement the MDT measurement in the bending plane. Physically, the TGCs are a type of multi-wire proportional chamber [3, 4, 26]. The fundamental difference between the TGC and a typical multi-wire proportional chamber is that the distance between the high voltage anode wires, 1.8 mm, is larger than the distance between the cathode and the anode itself, 1.4 mm. The readout strips are located at the top of the device and are orthogonal to the anode wires. The anode wires are 50 μm in diameter and held at a voltage of $\sim$ 2900 V. A schematic showing this layout is found

in Figure 4.19.
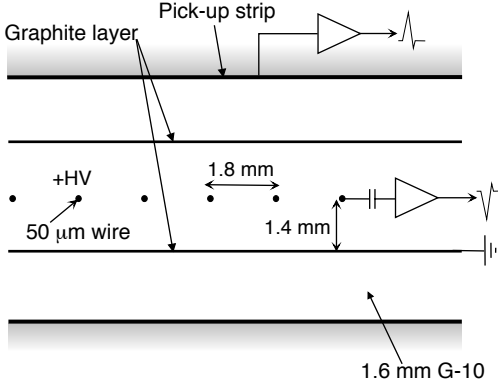
Figure 4.19: A schematic of the TGC structure showing the anode wires and graphite cathodes. The readout strips are orthogonal to the anode wires.

The TGCs are operated with a highly quenching gas mixture comprised of 55% CO_2 and 45% n-pentane. The time resolution is 99% efficient at determining a 25 ns bunch crossing window.

4.6   ATLAS Expected Performance

The expected resolution for the various detector components and their coverage is detailed in Table 4.6. For high-p_T muons, the muon-spectrometer performance is independent of the innder-detector. These values are important because they provide a basis for understanding the lepton detector response functions that will be used to measure the mass and width of the Higgs boson.

The angular performance of tracking in the ATLAS detector is extremely good [4]. The typical azimuthal (ϕ) angular resolution is around 100 μrad while the polar angular resolution on $\cot(\theta)$ is about 1×10^{-3}. These resolutions have a negligible effect on the invariant mass of the Z, typically less than one part in a million. This makes

Table 4.1: General performance design specifications of the ATLAS detector. [4].

Detector Subsystem	Required Resolution	η coverage	
		Measurement	Trigger
Inner Detector	$\sigma_{p_\mathrm{T}}/p_\mathrm{T} = 0.05\% p_\mathrm{T} \oplus 1\%$	$\|\eta\| < 2.5$	
EM Calorimeter	$\sigma_E/E = 10\%/\sqrt{E} \oplus 0.7\%$	$\|\eta\| < 3.2$	$\|\eta\| < 2.5$
HCAL (Barrel and End-cap)	$\sigma_E/E = 50\%/\sqrt{E} \oplus 3\%$	$\|\eta\| < 3.2$	$\|\eta\| < 3.2$
HCAL (Forward)	$\sigma_E = 100\%/\sqrt{E} \oplus 10\%$	$3.1 < \|\eta\| < 4.9$	$3.1 < \|\eta\| < 4.9$
Muon Spectrometer	$\sigma_{p_\mathrm{T}} = 10\%$ at $p_\mathrm{T} = 1$ TeV	$\|\eta\| < 2.7$	$\|\eta\| < 2.4$

it much easier to parameterize the detector response because the three-dimensional response in momentum, η, and ϕ can be reduced to a one-dimensional response in momentum. For muons this one-dimensional momentum response will be affected by the performance of the ID and MS.

4.7   ATLAS Data and Run Periods

The operational period during which data was collected by the ATLAS detector lasted for four years: 2009, 2010, 2011, and 2012. Figure 4.20 shows, in green, the total integrated luminosity delivered by the LHC machine to the ATLAS detector as a function of time in the 2011 and 2012 run periods. In yellow is the total integrated luminosity collected by the ATLAS detector. The data collected by ATLAS is further subdivided into a unit called the "run period." These run periods are blocks of time during which the detector and beam conditions are similar. If the beam conditions change dramatically, a new run will typically be started. In general, the run period lasts anywhere from a few weeks to a month or more. Within each "run period" is the individual "run." A run is a specific block of time during which the ATLAS detector

is continuously collecting data. If the beam is lost, the run will be stopped and the detector data acquisition is put on standby. The LHC is able to produce continuous collisions for a few hours. Thus, the typical length of a run is a few hours. Runs cannot be indefinite because the luminosity of the beam gradually decreases and it becomes advantageous to inject a new beam with the maximum luminosity.
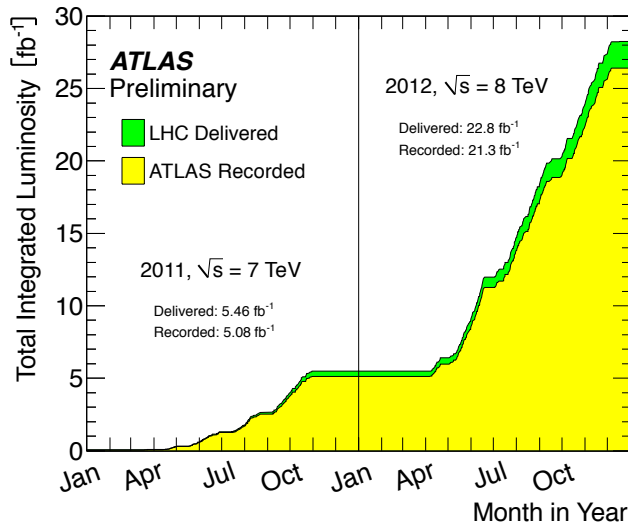
Figure 4.20: Cumulative luminosity versus time delivered to ATLAS (green) and recorded by ATLAS (yellow) during stable beams for *p-p* collisions at 7 and 8 TeV centre-of-mass energy in 2011 and 2012.

Within each run is a further subdivision called the "lumi-block." The lumi-block is an invented subdivision that corresponds to one or two minutes of data collection time. Figure 4.21 shows an example of the instantaneous luminosity profile for an ATLAS run. The "LHC Delivered All" luminosity refers to the LHC collisions produced at ATLAS interaction point in a given lumi-block regardless of whether the collisions occurred while the beams were properly focused and collimated while "LHC Delivered Stable" refers to the collisions provided by the LHC in which the beams were stable. "ATLAS Ready Recorded" refers to the collisions recorded by the ATLAS detector.

From the figure, it is clear that the instantaneous luminosity gradually decreases with time. This decrease is because the beam gradually dissipates as proton-proton collisions and beam-line interactions remove protons from the beam.
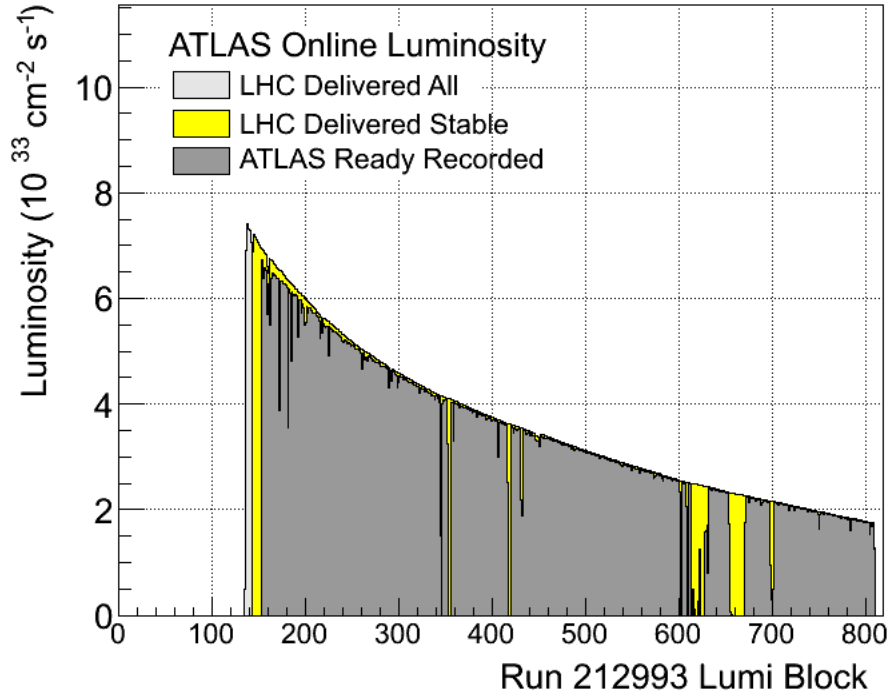
Figure 4.21: The instantaneous delivered (in yellow) and ATLAS recorded (in dark grey) luminosity for an example run.

4.7.1   ATLAS Data Quality

There is an additional down time durring which the ATLAS detector is recording data, but the data is questionable or faulty for some reason. This could be for a multitude of reasons. Oftentimes, a noise burst in the calorimeter will cause the data for a few lumi-blocks to be flawed or an electronic malfunction in the ATLAS end-cap trigger system could cause a few minutes of downtime while the trigger is recovered.
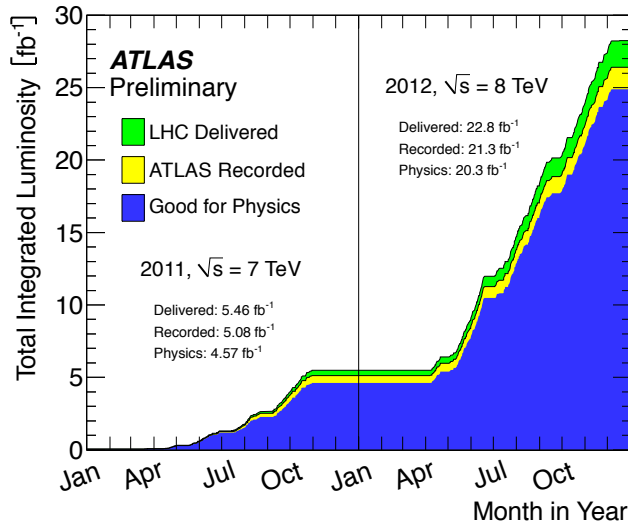
Figure 4.22: Cumulative luminosity versus time delivered to ATLAS (green), recorded by ATLAS (yellow), and certified to be good quality data (blue) during stable beams for *p-p* collisions at 7 and 8 TeV centre-of-mass energy in 2011 and 2012.

These lumi-blocks are flagged by a combination of automatic algorithms and data quality analyzers who check through the runs looking for problems that could have occurred during the data taking. This is a monumental task, but the final result is a data quality database which lists "defects" that are present in various runs and where they occur. When an analysis is selecting data, it need only specify which defects are intolerable for it and it is possible to produce a data set which does not include the lumi-blocks in which these defects are present. In 2012, this 95.5% of recorded ATLAS data could be used for analysis. This efficiency can be seen by comparing the blue and yellow histograms in Figure 4.22.

4.8   ATLAS Triggering

During 2011 and 2012, the LHC operated with a 20 MHz rate of *p-p* collisions. To reduce this to a manageable rate, triggering algorithms are used. This trigger has multiple levels. At Level 1 (L1), the trigger is extremely fast and relies on hardware and hit coincidence to determine what is called a *region of interest* (ROI). This ROI is a physical part of the detector which has a signal consistent with a certain particle and it is used as an input to the higher level triggers. The L1 trigger gives a crude estimate of the momentum/energy using hardware coincidences. For example, if two or three layers of the muon spectrometer have hits in the resistive plate chambers (RPCs), these hits will pass through a fast hardware algorithm that determines, in a coarse way, the curvature of these hits. If the momentum is above the threshold required by the L1 trigger, information is read out of the detector and it passes to the higher Level 2 (L2) trigger. The L2 trigger reduces the rate from 75 kHz to 3.5 kHz. The last stage of the trigger is called the Event Filter. The Event Filter performs the full reconstruction algorithms and the hard reconstruction level p_T and energy cuts are applied. The Event Filter further reduces the data collection rate from 75 kHz to 200 Hz. The fully triggered events, also known as *raw data*, are stored on tape drives that can be accessed to produce Event Data Summary (ESD) files and Analysis Object Data (AOD) files which can then be used for analyses.

Chapter 5

Muon Performance

As discussed in Chapter 4, the ATLAS detector is composed of many different detector subsystems which work together to measure the energy and momentum of particles that pass through. Muon reconstruction utilizes tracking information from the muon spectrometer and inner detector to fully reconstruct the trajectory of muons. For the Higgs analysis, the understanding of the muon performance in ATLAS data and simulated data is essential to properly estimate the event yield and to derive muon detector response functions.

The muon performance measurements fall into one of three categories: efficiency, scale, and resolution. Scale and resolution are related to how the momentum of the particle is measured by the detector while efficiency relates to the rate at which particles are reconstructed or identified using a given algorithm.

The muon reconstruction efficiency is the probability that a muon will pass the requirements from the identification and reconstruction algorithms. If an algorithm identifies every track as a muon it will have a 100% efficiency but this will come at

the expense of another quantity known as the "fake rate." "Fake rate" refers to the percentage of reconstructed muons that are not actual muons. Due to the tradeoff between "efficiency" and "fake rate," different "operating points" are typically specified for reconstruction algorithms which optimize these two quantities for the specific needs of various analyses. These operating points will give a better efficiency at the expense of the fake rate or vice versa.

The efficiency scale factor, defined in Equation 5.1, is used to weight events so that the efficiency in data and simulated events will match.

$$SF_\epsilon = \frac{\epsilon_{data}}{\epsilon_{MC}} \tag{5.1}$$

For example, if the efficiency as measured in data were 80% and the efficiency in MC were 90%, a comparison of data events to MC events would show more MC events than there should be. By weighting the MC events with the scale-factor, the data and MC can be brought into agreement. This weighting can be multiplicatively combined for different muons in an event to give the weight for the entire event. Thus for a 4-muon event, the muon efficiency weight would be $w_\epsilon = \prod_{i=1}^{4} SF_{\epsilon,i}$. Additional weightings such as the luminosity weighting would also need to be applied to compare data and MC. Understanding the efficiency is important for the Higgs analysis because the efficiency with which muons are reconstructed will directly affect the measured normalization of both signal and background. If this measured normalization differs from the expected normalization, it can indicate that the Higgs production cross section differs from the one predicted by the Standard Model.

A muon momentum scale correction refers to the systematic shift in the measured momentum relative to the truth momentum of a muon. If, for example, every muon

was measured by ATLAS to have 2 GeV more momentum than it actually had, a flat 2 GeV scale correction should be applied to correct the data. A scale correction need not be flat, however, and it can depend on many different quantities including the region of the detector the muon passed through or the momentum of the muon itself. If the muon momentum scale is wrong, this will affect the Higgs mass thereby resulting in a systematic shift in the measured Higgs mass.

The resolution of the muon momentum describes the spread in measurements which can be expected if identical muons pass through the detector. Like the scale, the resolution can depend on which region of the detector the muon has passed through and on the momentum of the muon. It is not possible, without adding additional information, to reduce the resolution of a measurement. The goal of resolution corrections is simply to ensure that simulation and data have the same resolution. Simulated muons in Monte Carlo are produced with better resolution than is expected in data. The simulated muon resolution can then be corrected to match the data by adding a randomly distributed number to the momentum of the Monte Carlo muon momentum. In the ensemble of muon momenta, this smearing has the effect of degrading the muon resolution. The amount of smearing can be tuned so that the resolution of muons in Monte Carlo will match the resolution of muons in data. For the Higgs analysis, the smearing of the muon momentum will translate into a smearing of the width of the four-lepton invariant mass. Accordingly, if the resolution is not properly corrected in Monte Carlo, the Higgs width measurement will be biased.

5.1 Low p_T Muon Reconstruction Efficiency

Many ATLAS analyses rely on a proper understanding of muons. Because the $H \to ZZ^{(*)} \to 4\ell$ involves a low-mass off-shell Z-boson which decays to muons, it is vitally important to understand the behavior of low-p_T muons and their reconstruction rate in the ATLAS detector. As mentioned in the introduction, this thesis is reliant on a precise understanding of the muon reconstruction efficiency to properly measure the Higgs cross section.

The goal of this particular measurement is to determine the ATLAS muon reconstruction efficiency at low p_T and the data over Monte Carlo scale factors. The probability to reconstruct a muon will, in general, depend on the kinematic properties of the muon and its trajectory in the detector. The ATLAS muon spectrometer is not hermetic nor is its coverage uniform. Because of this, the efficiency will depend on both the pseudorapidity, η, and the ϕ-coordinate of the muon's track. Muons of different charge deflect in the ATLAS magnetic field in opposite directions thereby causing the reconstruction efficiency to exhibit a charge dependence. To account for these kinematic and detector effects, efficiencies and scale factors will be calculated for different p_T, η, and $q \times \eta$ regions. The effect of the running conditions on the efficiencies was examined by looking for run period or pileup[1] dependence.

To measure the muon reconstruction efficiency at low p_T, tag and probe was performed using the J/ψ resonance. To select J/ψ candidates, events were required to have one fully reconstructed muon, known as the tag, and one track, the probe, which forms an invariant mass with the tag consistent with the mass of a J/ψ. The

---

[1]In this study, pileup is measured by the number of primary vertices in the event.

fully reconstructed tag aids in minimizing track-track backgrounds and increases the probability that the event comes from the J/ψ resonance. Despite this, many di-muon continuum and track combinatoric background events will still pass the tag-probe selection requirements. To remove the backgrounds, the invariant mass of the candidate tag-probe pairs is fitted with a polynomial background plus a Gaussian signal. The efficiency is then calculated by dividing the number of events in the signal Gaussian for reconstructed tag-probe pairs by the total number of events in the signal Gaussian for all tag-probe pairs.

This study was performed using the 2011 data set from p-p collisions at 7 TeV. The details of the measurement and the infrastructure are based on the 2010 measurement done using an integrated luminosity of 42 pb^{-1} detailed in [27] and [28]. Concurrently, a study on higher p_{T} muons was done using a $Z \rightarrow \mu\mu$ sample. The $Z \rightarrow \mu\mu$ measurement is detailed in [29], [30] and was updated for the full 2011 dataset encompassing an integrated luminosity of 5.23 fb^{-1}.

5.1.1   Data and Monte Carlo Samples

Data Samples

The measurement uses data from 2011 after applying a tight good run list (GRL) which requires good detector operating conditions. After applying the GRL, the integrated luminosity is 4.43 fb^{-1}. The trigger used for the analysis is the highly prescaled[2] EF_mu6_Trk_Jspi_loose. Applying the prescales, the luminosity used for

---

[2]Prescaled means that only a fraction of actual triggered events are recorded. The prescale is the fraction of triggered events that are recorded to disk.

the baseline measurement drops to 167.73 pb^{-1}. EF_mu6_Trk_Jspi_loose works at Levels 1 and 2, by requiring a 6 GeV muon. At the Event Filter (EF) level, a track with $p_{\mathrm{T}} > 3.5$ GeV is selected and required to form an invariant mass with the triggered muon in the range 2600 MeV - 3600 MeV. The prescale for EF_mu6_Trk_Jspi_loose is variable and changes both within run periods and within individual runs.

Monte Carlo Samples

For calculating scale factors, Monte Carlo samples are used as shown in Table 5.1. Each of the samples was generated using Pythia [31]. The events were then put through the ATLAS detector and hits were simulated using GEANT4 [32, 33]. Pileup interactions in both the same and nearby bunch crossings are included in the simulation. The pileup and detector conditions were not constant throughout 2011. To simulate this, the Monte Carlo events were produced for four representative "run periods."

Table 5.1: Direct and Indirect J/ψ Monte Carlo samples used in the analysis.

Description	Size (events)
Direct J/ψ Production $p_{\mathrm{T}} > 2.5$ GeV	1M
Direct J/ψ Production $p_{\mathrm{T}} > 4$ GeV	5M
Indirect J/ψ Production $p_{\mathrm{T}} > 2.5$ GeV	2M
Indirect J/ψ Production $p_{\mathrm{T}} > 4$ GeV	5M

5.1.2 Muon Types

To reconstruct muons in the ATLAS detector, complex algorithms are used which incorporate information from many components of the detector. These algorithms can

be tuned to have a higher efficiency or higher fake rejection. The two reconstruction chains used by ATLAS to reconstruct muons are Chain 1, STACO [34] and Chain 2, MUID [35]. The primary muon types used for different analyses are the following:

Combined (CB) Muons are the statistical combination of an inner detector track with a track in the muon spectrometer.

Segment Tagged (ST) Muons are an inner detector track which points to segments in the muon spectrometer. Unlike the combined muons, there is no fully reconstructed track in the muon spectrometer for a segment tagged muon.

Standalone (SA) Muons are those which have no track in the inner detector but a fully reconstructed track in the muon spectrometer. These are particularly useful for high-pseudorapidity (> 2.5) regions where the inner detector does not have coverage.

Calorimeter Tagged (CT) Muons are muons with an inner detector track which points to the calorimeter. If the energy deposit in the calorimeter is found to be consistent with the energy deposition from a muon, the track is said to be calorimeter tagged. These types of muons are particularly useful for the central region of the detector where there is a hole in the muon spectrometer for ID and calorimeter cabling and services.

The $J/\psi \to \mu^+\mu^-$ efficiency study provides the muon reconstruction efficiency and scale factors for CB and ST muons and each of the muon reconstruction chains, STACO and MUID. Calo-tagged muons are also used by the analysis. The specific calo-tagging algorithm used in the $J/\psi \to \mu^+\mu^-$ efficiency study works by preselecting

ID tracks which satisfy a loose track isolation[3] requirement of $\log\left(\sum_{0.45} p_\mathrm{T}^{iso}/p_\mathrm{T}\right) \leq$ 0.9. Next, a calorimetric isolation is put in place. This is done by extrapolating tracks with $p_\mathrm{T} > 4$ GeV into the calorimeter and summing up their corrected energy deposition. The η dependent values for this calorimetric cut are found in Table 5.2. If the energy isolation requirements are not satisfied then a likelihood-ratio (LHR) discriminant is used to determine whether the energy loss around the track is consistent with the energy deposition of a muon (minimum ionizing particle).

Table 5.2: Calo-Tagging isolation requirements. The track isolation cuts are used in preselection while the energy isolation is applied in post-selection.

	Track $|\eta|$ range	Cuts
Track Isolation	$|\eta| \leq 2.5$	$\log\left(\sum_{0.45} p_\mathrm{T}^{iso}/p_\mathrm{T}\right) \leq 0.9$
	$|\eta| \leq 2.5$	$LHR > 0.5$
Energy Isolation	$|\eta| \leq 1.5$	$E_T^{iso,0.4}/p_\mathrm{T} \leq 3$ AND $E_T^{iso,0.4} \leq 17$ GeV
	$1.5 < |\eta| \leq 1.8$	$E_T^{iso,0.4}/p_\mathrm{T} \leq 1.4$ AND $E_T^{iso,0.4} \leq 10$ GeV
	$1.8 < |\eta| \leq 2.5$	$E_T^{iso,0.4}/p_\mathrm{T} \leq 1.6$ AND $E_T^{iso,0.4} \leq 13$ GeV

5.1.3   Method

Tag and Probe Selection

The ATLAS muon reconstruction efficiency is measured by selecting events with a fully reconstructed muon tag, and a probe which does not rely on data from the muon spectrometer. The tag and the probe must form an invariant mass consistent with the mass of the J/ψ. In this analysis, a tag muon is defined to satisfy the following requirements:

---

[3]The expression $\sum_{0.45} p_\mathrm{T}$ refers to the summation of track momentum in a ΔR half-width cone of 0.45 around the track to be calo-tagged.

- Each tag muon must be a combined (CB) muon associated to a good quality, as defined below, Inner Detector (ID) track.

- The tag muon is required to match a muon triggered by EF_mu6_Trk_Jpsi_loose. This is done by extrapolating the tag muon's ID track into the muon spectrometer and matching the η-ϕ region of interest (ROI) to which the extrapolation corresponds to the ROI fired by the triggered muon.

- Tag muon $p_{\mathrm{T}} > 6$ GeV and $|\eta| < 2.5$.

- The distance of closest approach to the primary vertex in the longitudinal plane and transverse plane are required to be $|z_0| < 1.5$ mm and $|d_0| < 0.3$ mm respectively.

- The z_0 and d_0 significance are required to be less than 3.

In an event where a tag muon is selected, each track is considered as a probe if it satisfies the following:

- $p > 3$ GeV, $|\eta| < 2.5$ and a good quality track.

- χ^2 divided by the number of degrees of freedom of the fit to a common vertex (between tag and probe) must be smaller than 6.

- $\Delta R = \sqrt{(\Delta\phi)^2 + (\Delta\eta)^2} < 3.5$ where ΔR is the distance between the tag and probe.

- Probe $p_{\mathrm{T}} > 4$ GeV to avoid selecting tracks that could not fire the EF_mu6_Trk_Jpsi trigger.

- The probe is calo-tagged.

When multiple probes are associated with a certain tag, only the probe with the minimum $\chi^2/ndof$ fit to a common vertex with the tag is considered. As mentioned above both tag and probes must correspond to a "good quality" track. These good quality tracks are inner detector tracks which satisfy a number of quality cuts:

- Number of pixel hits greater than 1.

- Number of SCT hits greater than 6.

- For $|\eta| < 1.9$, the number of probe TRT hits must be greater than 5 of which no more than 90% can be outliers. .

- For $|\eta| \geq 1.9$ if the number of probe TRT hits is greater than 5, no more than 90% can be outliers.

To avoid situations where there is ambiguity as to whether the tag or probe muon fired the LV1 trigger, a set of cuts are applied which prevent the tag and the probe from occurring in the same region of interest. These cuts take into account the size (in η and ϕ) of an ROI and the p_T-dependent bending. The cuts are as follows:

- For probe $p_\mathrm{T} \leq 8$ GeV, $|\eta_{tag} - \eta_{probe}| > 0.4$ and $|\phi_{tag} - \phi_{probe}| > 0.5$.

- For probe $p_\mathrm{T} > 8$ GeV and probe $p_\mathrm{T} \leq 10$ GeV, $|\eta_{tag} - \eta_{probe}| > 0.3$ and $|\phi_{tag} - \phi_{probe}| > 0.35$.

- For probe $p_\mathrm{T} > 10$ GeV, $|\eta_{tag} - \eta_{probe}| > 0.2$ and $|\phi_{tag} - \phi_{probe}| > 0.25$.

Efficiency Measurement

To calculate the ATLAS muon reconstruction efficiency, the tag and probe pairs are divided into two separate populations: one where the probe is matched to a reconstructed muon (matched) and one where it is explicitly not reconstructed (unmatched). Figure 5.1 shows a sample invariant mass distribution for the matched and unmatched populations: The reconstruction efficiency is calculated by dividing
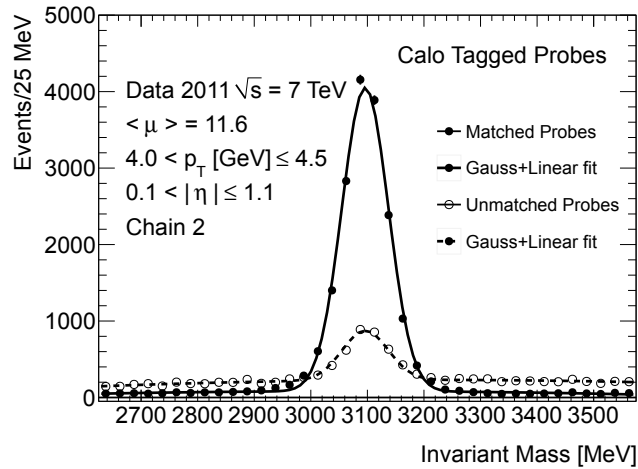
Figure 5.1: Invariant mass of the matched and unmatched tag-probe pairs. CB muons appear as filled circles, CB+ST probes appear as open circles. All probes in the diagram are for Chain 2 muons from the probe kinematic region $0.1 < |\eta| < 1.1$ and 3 GeV $< p_{\mathrm{T}} < 4$ GeV.

the number of reconstructed signal events by the total number of signal events. The number of signal and background tag-probe pairs comes from a simultaneous fitting of the matched and unmatched invariant mass distributions. The fitting process uses the following functions for the matched and unmatched tag-probe pairs.

Matched $\quad f_M(m) = N_{tot}\epsilon S(m, \mu_{matched}, \sigma_{matched}) + B_{matched}(m);$

Unmatched $\quad f_M(m) = N_{tot}(1 - \epsilon) S(m, \mu_{unmatched}, \sigma_{unmatched}) + B_{unmatched}(m).$

Here, N_{tot} represents the total signal normalization (e.g., tag and probe pairs coming from a J/ψ) and ϵ is the efficiency. $S\left(m, \mu_{matched}, \sigma_{matched}\right)$ is the Gaussian signal function for matched tag-probe pairs. $B_{matched}\left(m\right)$ is the polynomial (quadratic) background function for the matched tag-probe pairs. Correspondingly, $S\left(m, \mu_{unmatched}, \sigma_{unmatched}\right)$ is the Gaussian signal function for the unmatched tag-probe pairs and $B_{unmatched}\left(m\right)$ is the background function for the unmatched tag-probe pairs. In the fit, there are twelve free parameters.

- Efficiency (ϵ)

- Total number of signal tag-probe pairs (N_{total})

- Matched/unmatched signal width ($\sigma_{matched}/\sigma_{unmatched}$)

- Matched/unmatched signal mass ($m_{matched}/m_{unmatched}$)

- Matched number of background tag-probe pairs

- Matched background slope

- Matched background quadratic term

- Unmatched number of background tag-probe pairs

- Unmatched background slope

- Unmatched background quadratic term

The parameters and their associated errors are determined using a Minuit χ^2 fit, however, when one or more bins contain zero entries, a log-likelihood fit is used

instead. The uncertainty on the efficiency parameter, ϵ, is quoted as the statistical uncertainty. The invariant mass window is centered near the J/ψ peak at 3100 MeV and has a width of 950 MeV. This choice is made because the EF_mu6_Trk_Jpsi_loose requires the triggered muon and track to have an invariant mass within (2600, 3600) MeV.

5.1.4 Systematic Uncertainties and Checks

Systematic Uncertainties

Systematic uncertainties arising from the signal and background shapes have been added to the statistical errors. The three systematic uncertainties used in this analysis are:

1. **Signal Shape**: The mean and width of the Gaussian, instead of varying freely, are fixed between the matched and unmatched.

2. **Background Shape**: A linear background is used in the fit, instead of the quadratic baseline.

3. **Alternative Fit**: Instead of simultaneously fitting the matched and unmatched tag-probe pair populations, the efficiency is calculated by fitting the matched and total tag-probe pairs.

The systematic uncertainties are calculated by finding the maximal positive and negative deviation from the baseline of these three alternative methods and then adding these maximal positive and negative variations in quadrature to the statistical un-

certainty. For the linear background models, a reduced fitting window (600 MeV) is used for $|\eta| < 1.7$.

Systematic Checks

In addition to the signal and background shape and fitting methods, other systematic checks have been performed to ensure the consistency of the measurement. These include:

1. **Probe Selection**: A cross-check using Inner Detector (ID) tracks as probes is used to verify the baseline calo-tagged probe measurement (see Figure 5.2 and Figure 5.3).

2. **Pileup**: To determine if there is an effect on the efficiency from pile-up, the efficiency was measured for different number of interaction vertices per event, *nvtx* (see Figure 5.4).

3. **Run Period Dependence**: To determine if the efficiency changes with the different conditions present in separate data-taking run periods, a binning with respect to run period was made (see Figure 5.5).

As seen in Figure 5.2 and Figure 5.3, there is good agreement (within errors) between the efficiency as calculated using ID and CT probes. One noticeable feature is that systematic errors tend to be higher for the ID probe based measurement. This is due to having a higher background with more structure than the calo-tagged background which is primarily linear. This non-linear background leads to increased systematics as the different fitting methods give slightly different results.
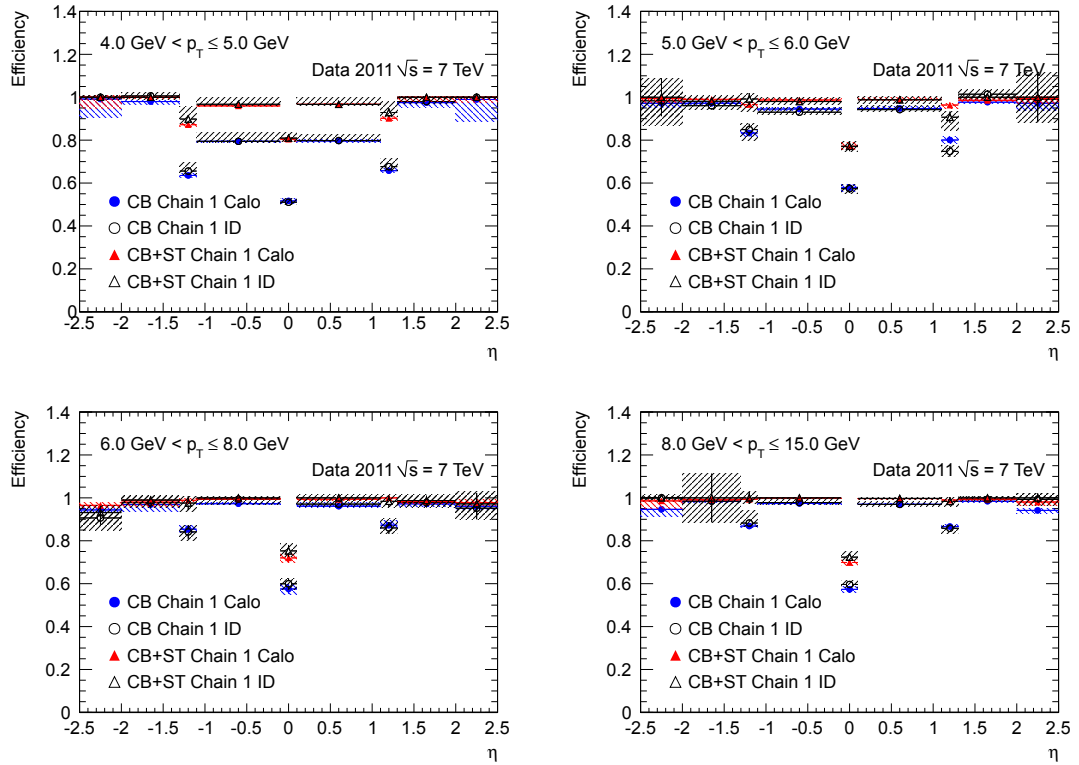
Figure 5.2: Efficiency versus η for STACO CB and CB+ST muons. Circles are for CB muons, triangles are for CB+ST muons. Black open points are for ID-probes while red and blue filled points are for CT-probes. The error bars correspond to the statistical uncertainty and the error bands represent the total (statistical+systematic) uncertainty.
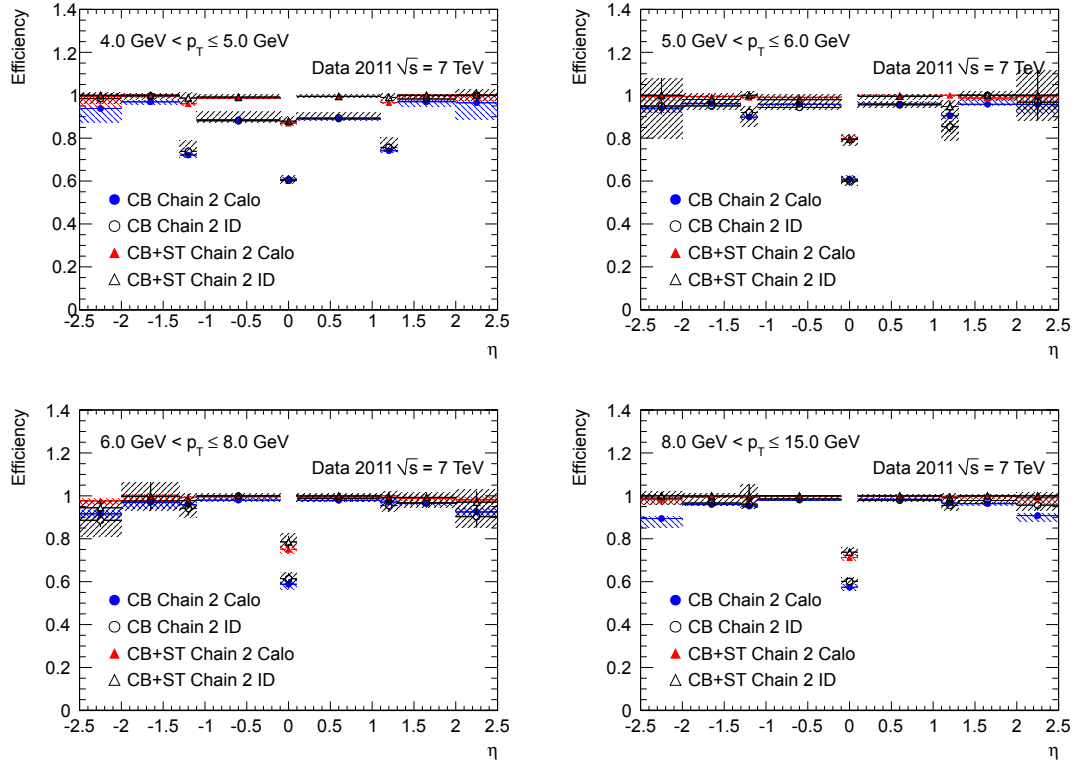
Figure 5.3: Efficiency versus η for STACO CB and CB+ST muons. Circles are for CB muons, triangles are for CB+ST muons. Black open points are for ID-probes while red and blue filled points are for CT-probes. The error bars correspond to the statistical uncertainty and the error bands represent the total (statistical+systematic) uncertainty.

Figure 5.4 depicts the dependence of the efficiency on pileup: measured by the number of primary vertices per event. Although there may indeed be some structure especially noticeable in the crack[4] region, the trend is consistent with flat. As with the baseline measurement, the discrepancy between data and Monte Carlo in the CB muon measurement is recovered by adding ST muons. The binning used has been chosen to ensure a similar number of events per bin so that error bars should remain comparable. Figure 5.5 shows the dependence on run period, which itself is a measure
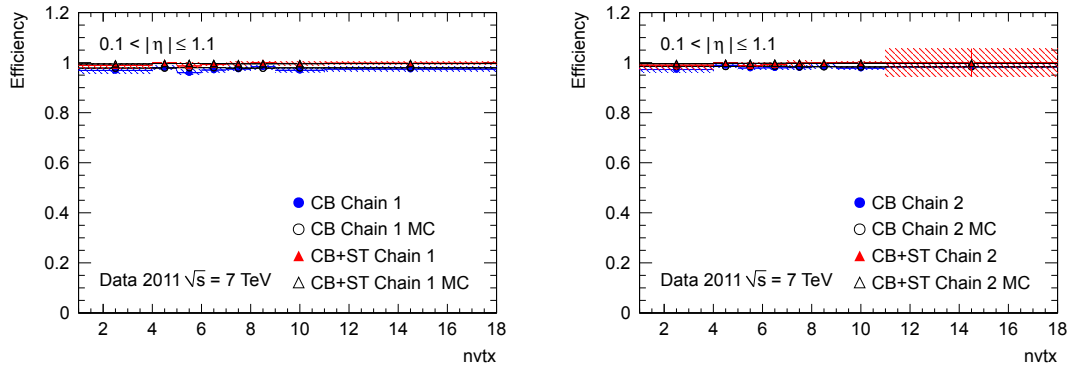
Figure 5.4: Efficiency versus the number of primary vertices (nvtx) for STACO (left) and MUID (right) CB muons for different η regions. The error bars correspond to the statistical uncertainty and the error bands represent the total (statistical+systematic) uncertainty.

of the dependence of the efficiency on both pileup and run conditions. The trend is consistent with being flat within the systematic and statistical errors. In particular, the bulk regions of the detector which have high statistics (barrel $0.1 < |\eta| < 1.1$ and end-cap $1.3 < |\eta| < 2.0$) show good agreement.

---

[4]The region around $\eta \approx 0$ is known as crack region. In this region, there is a hole in the muon spectrometer to allow for cabling for the calorimetry systems.
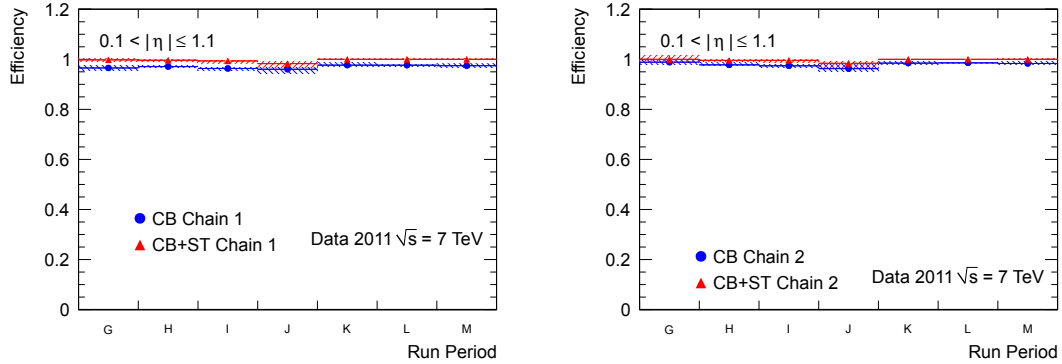
Figure 5.5: Efficiency versus run period for STACO (left) and MUID (right) CB muons for the barrel region. The error bars correspond to the statistical uncertainty and the error bands represent the total (statistical+systematic) uncertainty.

5.1.5 Results

Reconstruction Efficiency

The efficiencies were calculated for Chain 1 (STACO), Chain 2 (MUID), Combined (CB), and Combined+Segment Tagged (CB+ST). No dependence was observed with respect to the run periods. Accordingly, we conclude that the integrated dataset has only minimal sensitivity to the changing conditions during the data-taking.

Figures 5.6, 5.7 (binned in p_{T}) and Figures 5.8, 5.9 (binned in η) represent the CB and CB+ST muon reconstruction efficiency for both data and MC and for chain 1 and chain 2 muons. The colored points represent the data efficiency and the correspondingly shaped black points are the efficiency for the Monte Carlo samples. There is a noticeably lower efficiency in the $|\eta| \approx 0$ region due to the hole in the muon spectrometer used for cabling going through the muon spectrometer to the calorimeter and ID. This drop in efficiency can be recovered by using CT-muons. The CB and CB+ST efficiency in the crack region decreases with increasing p_{T}. This

is because the ATLAS toroidal field is very low in the transition region. The end-cap region shows a very clear efficiency plateau going down to 4 GeV. Most regions other than the crack have a plateau in efficiency between 6 GeV and 8 GeV.

Generally there is good agreement between data and MC. One exception to this is at low p_T in the region $0.1 < \eta < 1.3$ for the STACO reconstruction chain where fewer muons are reconstructed as CB muons in data than in MC. When ST muons are added, the discrepancy between data and MC disappears. Another noticeable feature is the large and asymmetric error bars for CB muons at high η and low p_T. This is because the unmatched signal is, in fact, highly dependent on the background model used as the resolution of the J/ψ is very poor in this p_T - η range and it becomes increasingly difficult to determine the proper background shape. The linear background model gives a smaller efficiency than the quadratic background model.

A plateau efficiency is reached, for both CB and CB+ST muons, at around 6 GeV. The CB muon plateau efficiency is at around 97% for both STACO and MUID. For CB+ST muons, the efficiency plateau is near 99%. In addition there is general agreement between data and MC leading to scale factors largely consistent with unity within one standard deviation. No appreciable pileup or period dependence was found. Efficiencies are generally consistent with being flat as a function of the run period and the number of pileup events.
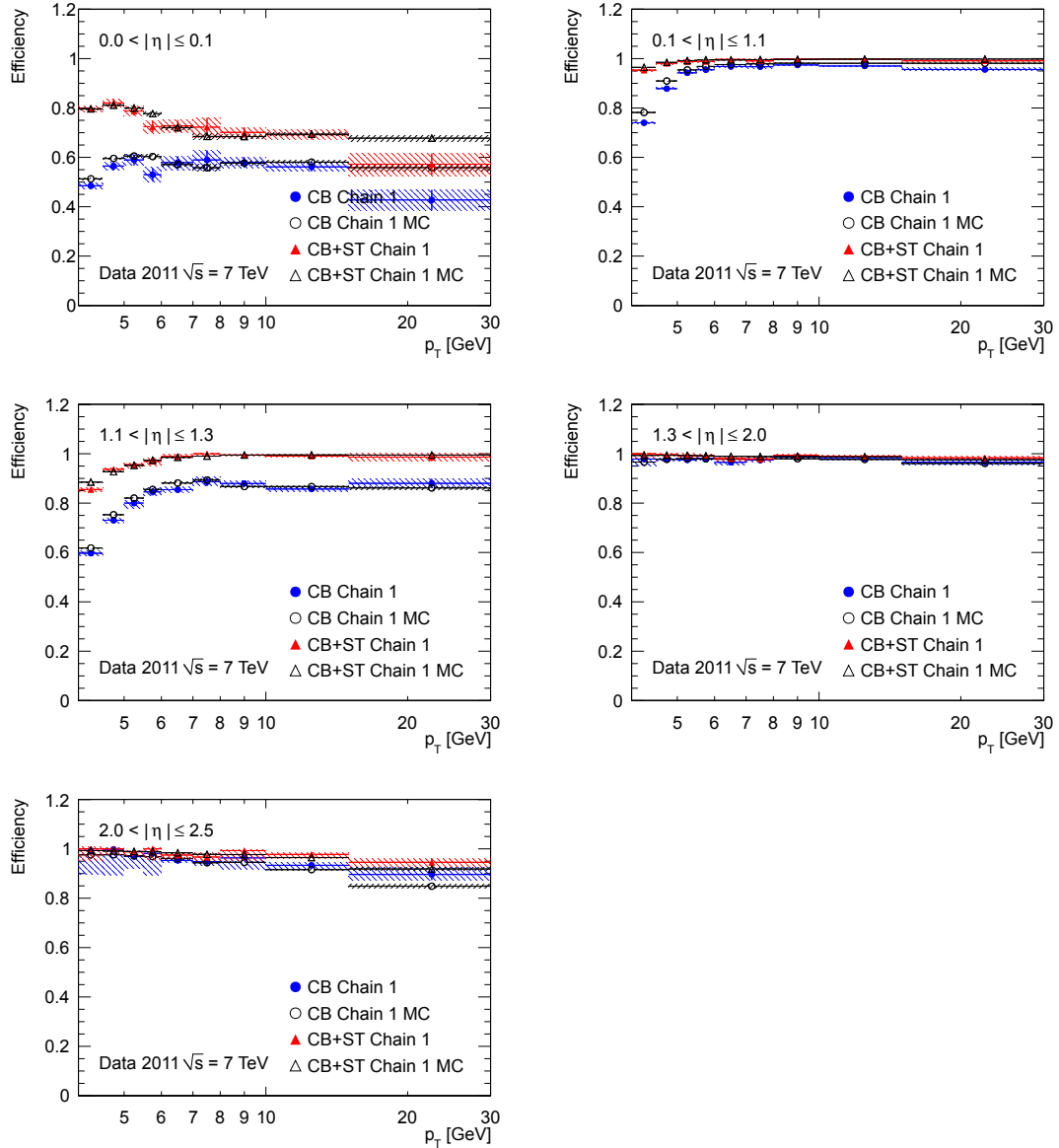
Figure 5.6: Efficiencies versus p_T for STACO CB muons and CB+ST muons from all run periods using the EF_mu6_Trk_Jpsi trigger. The five plots correspond to five slices in $|\eta|$. The error bars correspond to the statistical uncertainty and the error bands represent the total (statistical+systematic) uncertainty
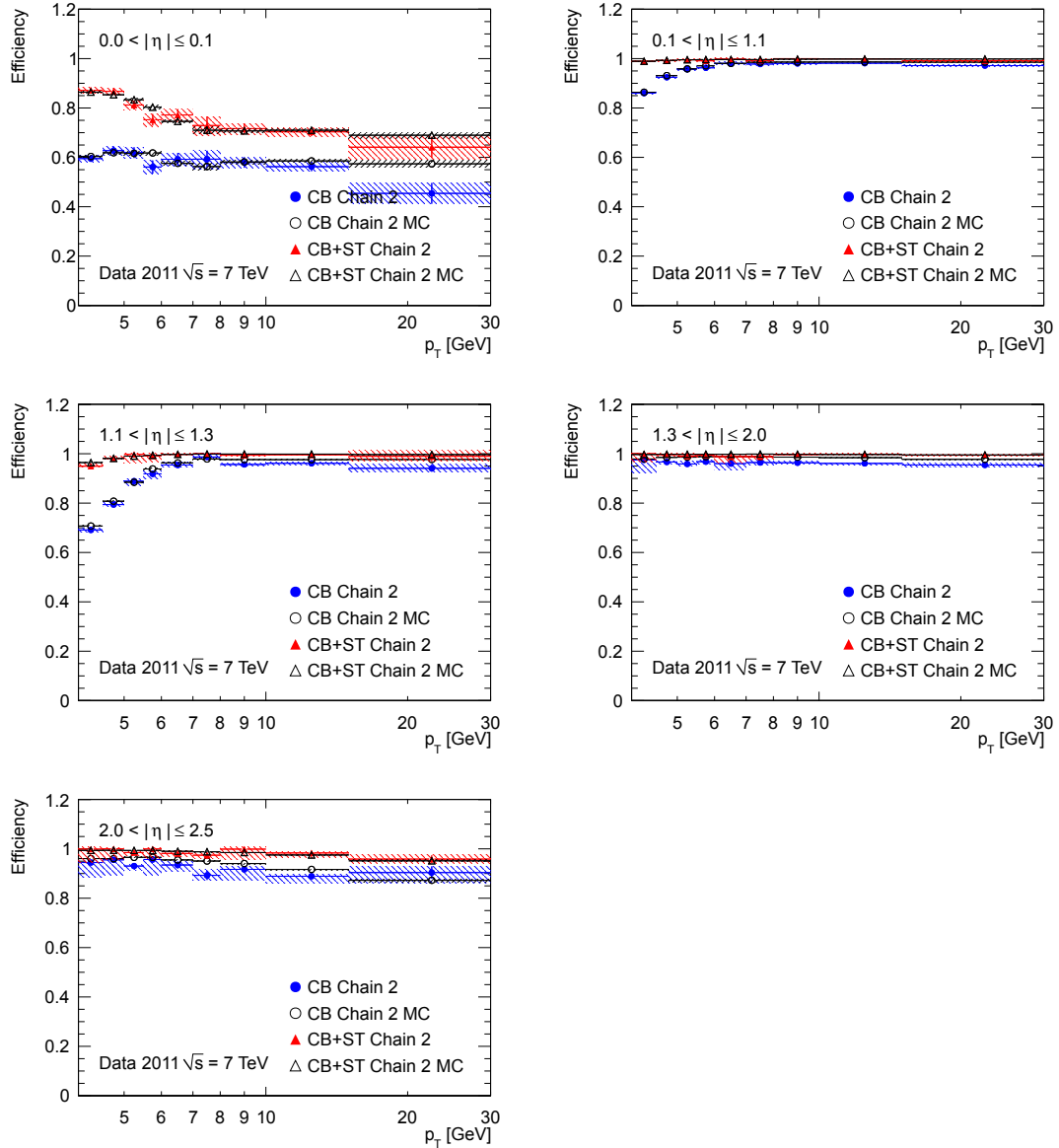
Figure 5.7: Efficiencies versus p_T for MUID CB muons and CB+ST muons from all run periods using the EF_mu6_Trk_Jpsi trigger. The error bars correspond to the statistical uncertainty and the error bands represent the total (statistical+systematic) uncertainty.
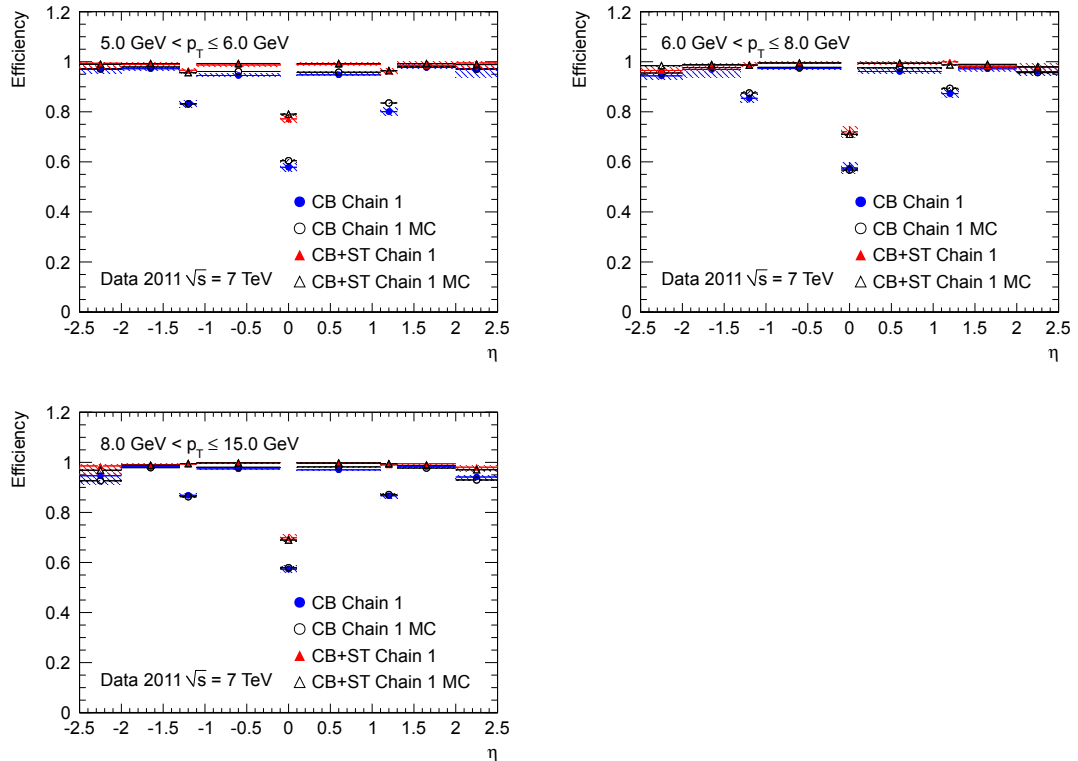
Figure 5.8: Efficiencies versus η for STACO CB muons and CB+ST muons from all run periods using the EF_mu6_Trk_Jpsi trigger. The error bars correspond to the statistical uncertainty and the error bands represent the total (statistical+systematic) uncertainty.
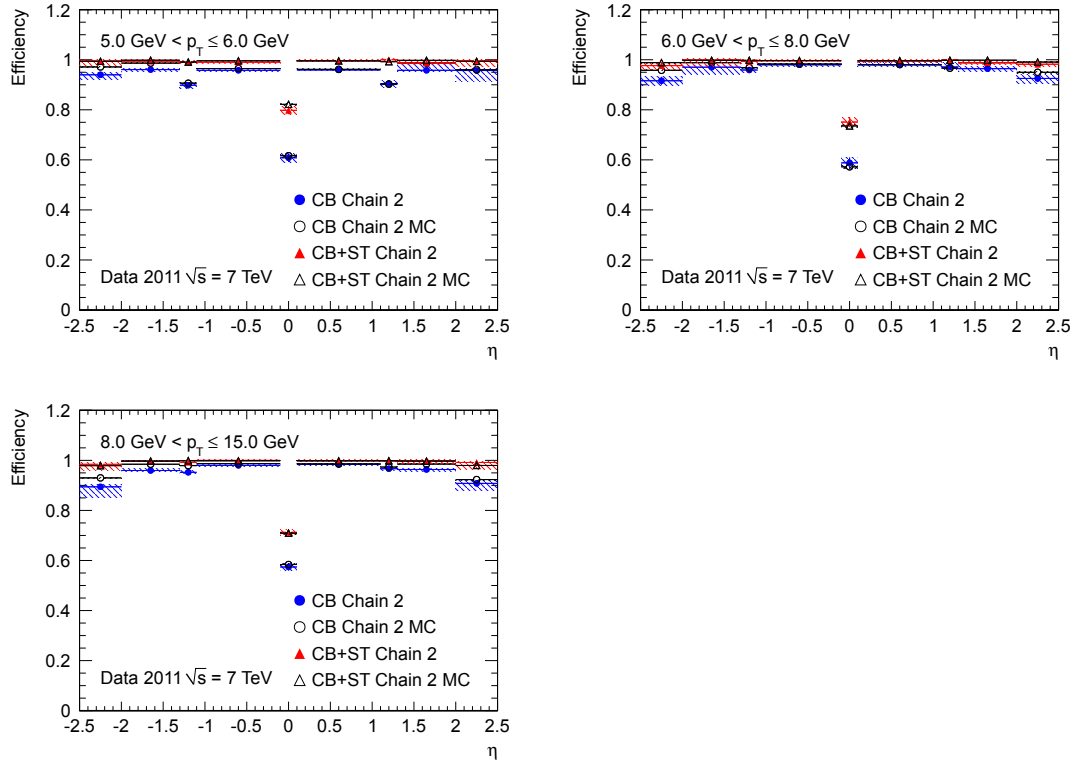
Figure 5.9: Efficiencies versus η for MUID CB muons and CB+ST muons from all run periods using the EF_mu6_Trk_Jpsi trigger. The error bars correspond to the statistical uncertainty and the error bands represent the total (statistical+systematic) uncertainty.

Charge Dependence

The large ATLAS toroid, eponymous with the ATLAS detector itself, is intended to bend muon tracks in η making measurement of the muon momentum possible. This bending is charge dependent. Positive charged particles will be bent toward larger values of η while negative charged particles will be bent in the negative η direction. To see the effect of this bending on the reconstruction efficiency, the efficiency can be measured versus $q \times \eta$ where q is the charge of the probe: probes with a positive $q \times \eta$ bend outward in $|\eta|$ and probes with negative values of $q \times \eta$ bend inward in $|\eta|$.
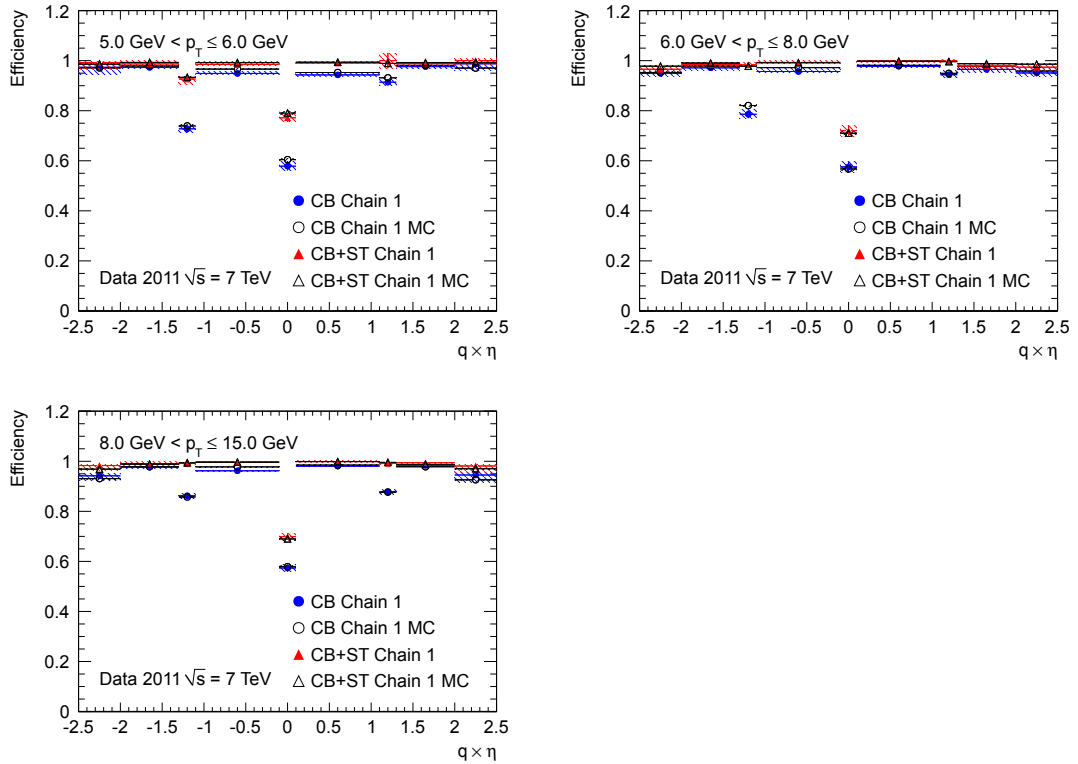
Figure 5.10: Efficiencies versus $q \times \eta$ for STACO CB muons and CB+ST muons from all run periods using the EF_mu6_Trk_Jpsi trigger. The error bars correspond to the statistical uncertainty and the error bands represent the total (statistical+systematic) uncertainty.
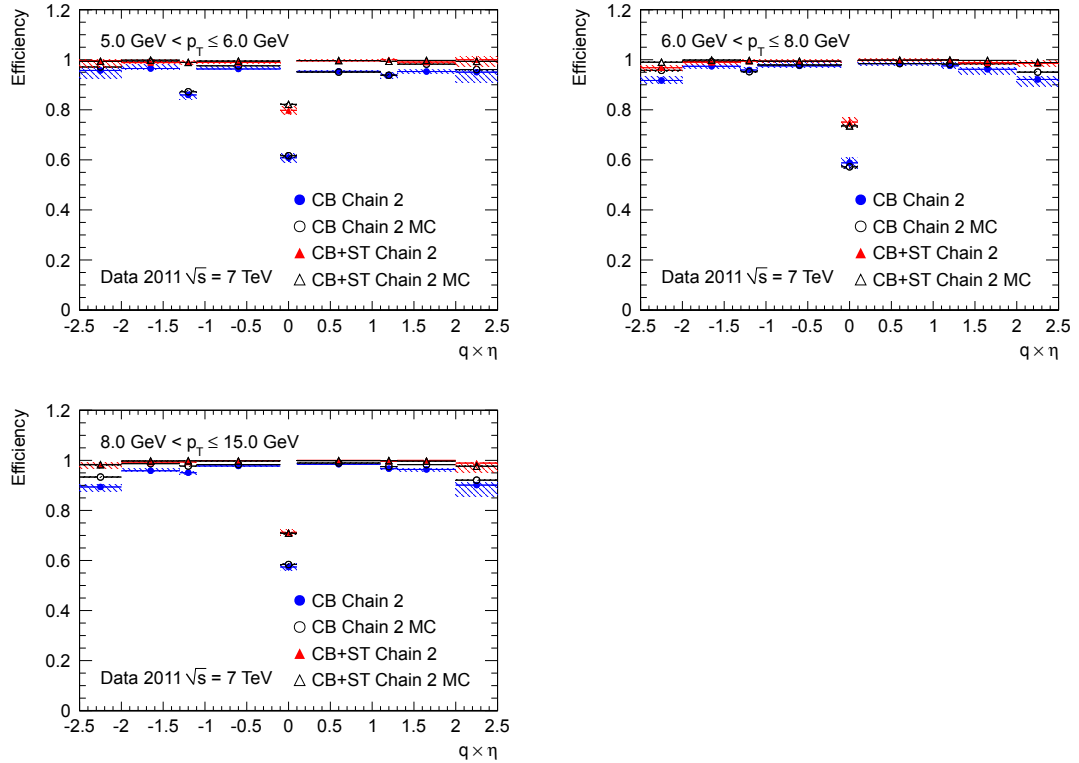
Figure 5.11: Efficiencies versus $q \times \eta$ for MUID CB muons and CB+ST muons from all run periods using the EF_mu6_Trk_Jpsi trigger. The error bars correspond to the statistical uncertainty and the error bands represent the total (statistical+systematic) uncertainty.

Data/MC Scale Factors

Figure 5.12 shows the STACO data over MC scale factors while Figure 5.13 shows the data over MC scale factors. In general, the scale factors are compatible with 1 indicating that the MC models the data in representing the reconstruction efficiency.
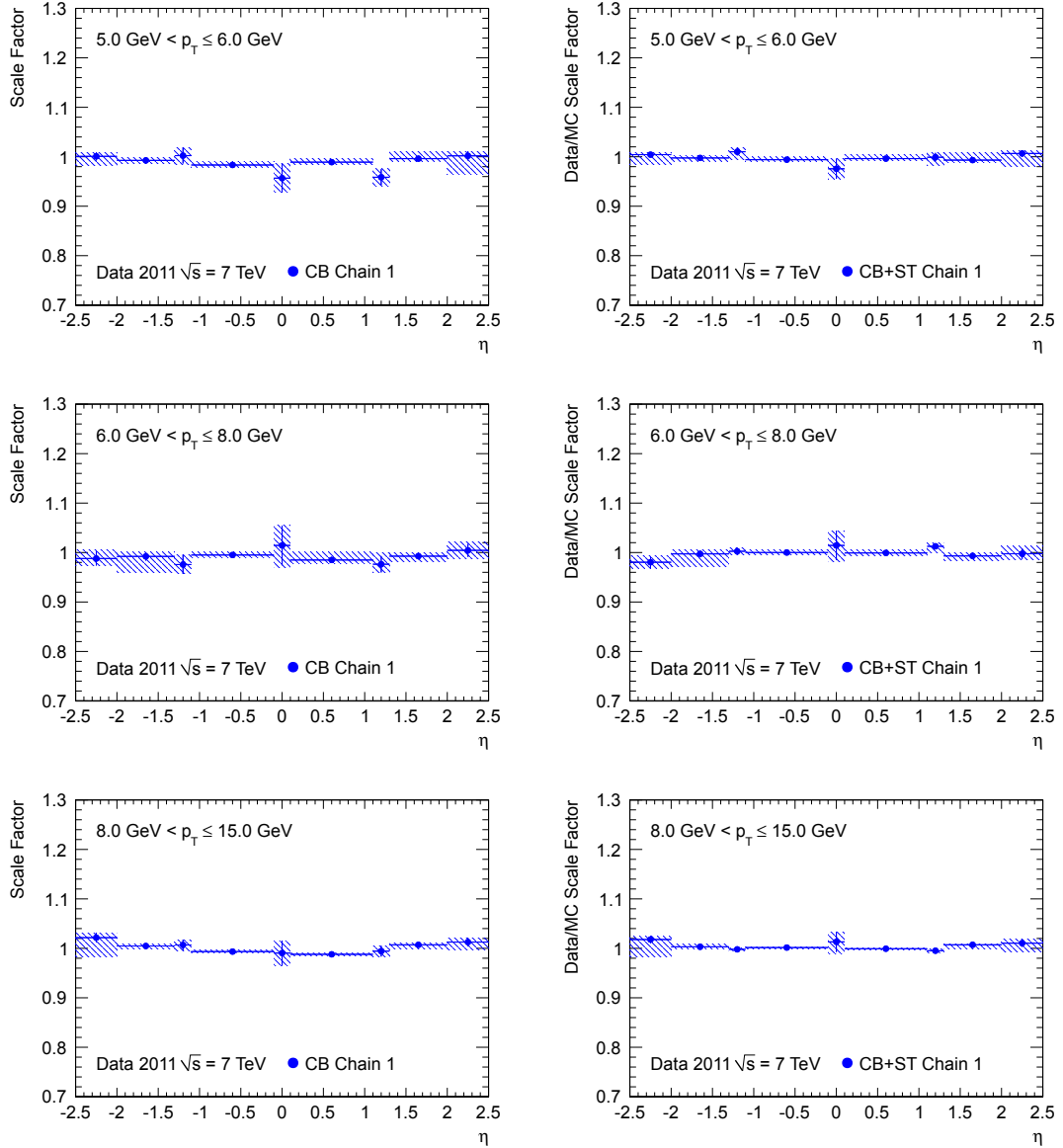
Figure 5.12: Data/MC scale factors versus η for STACO CB muons from all run periods using the EF_mu6_Trk_Jpsi trigger. The error bars correspond to the statistical uncertainty and the error bands represent the total (statistical+systematic) uncertainty.
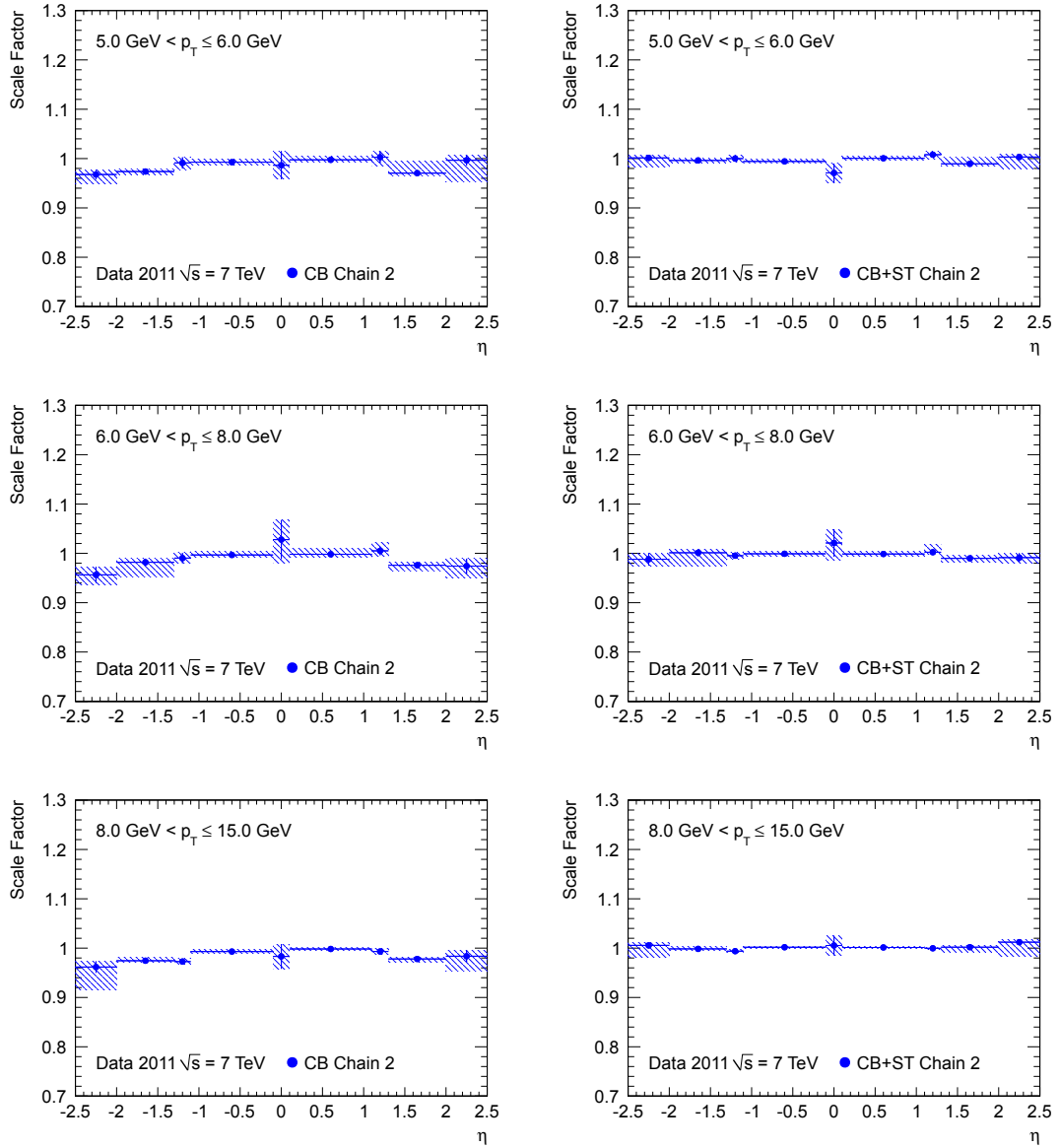
Figure 5.13: Data/MC scale factors versus η for MUID CB muons from all run periods using the EF_mu6_Trk_Jpsi trigger. The error bars correspond to the statistical uncertainty and the error bands represent the total (statistical+systematic) uncertainty.

5.2   High p_{T} Muon Reconstruction Efficiency

5.2.1   Reconstruction Efficiency

To measure the reconstruction efficiency at higher momentum, the Z resonance is used using a similar tag and probe method to that found in the J/ψ analysis. The full details of the high-p_{T} measurement are described in [36] and [6]. Figure 5.14 shows the muon reconstruction efficiency versus pseudorapidity for ID tracks (left) and Combined muons (right) using the STACO reconstruction chain. The ID reconstruction efficiency is very close to 1 for nearly the entire η region. The CB muon reconstruction efficiency is substantially lower but, as mentioned before, the fake rate for CB muons is very small. When measuring the efficiency of the ID track reconstruction, the probe used is a MS track. Similarly, when measuring the MS track efficiency, an ID track is used as the probe. Once these efficiencies are calculated, the efficiency of advanced reconstruction algorithms, such as the STACO or MUID Combined (CB) muon using ID muons as their probes can be measured.
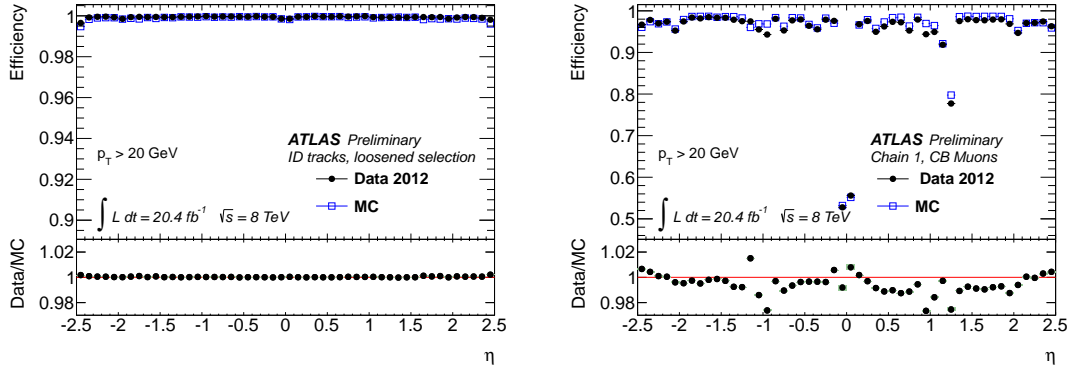
Figure 5.14: Left: measured ID muon reconstruction efficiency as a function of η for muons with $p_T > 20$ GeV. The efficiency is calculated with a relaxed selection requirement on the hit multiplicity in the ID with respect to the standard selection. The panel at the bottom shows the ratio between the measured and predicted efficiencies. Right: reconstruction efficiency for Chain 1 CB only muons as a function of η for muons with $p_T > 20$ GeV. The panel at the bottom shows the ratio between the measured and predicted efficiencies.

5.2.2   Comparison With Low p_T Muon Efficiency

As a validation, a comparison has been made between $J/\psi \to \mu^+\mu^-$ tag and probe and the $Z \to \mu\mu$ tag and probe measurements using 2011 data [30]. The highest p_T-bin from the J/ψ measurement, the 8.0 GeV $< p_T \leq 15.0$ GeV bin, is compared to the lowest p_T-bin from the Z measurement, the 15.0 GeV $< p_T \leq 20$ GeV bin. The two measurements show good agreement within their errors. This indicates that there is continuity between the muon reconstruction efficiency at low p_T and at high p_T. Similar measurements were performed using the J/ψ resonance using data from 2012 [36]. These measurements make it possible to use the low-p_T muons in the $H \to ZZ^{(*)} \to 4\ell$ analysis.
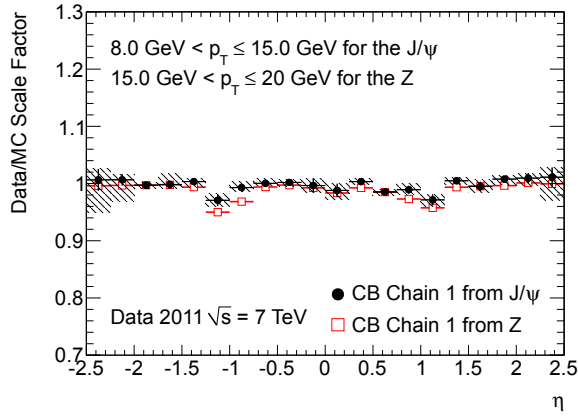
Figure 5.15: Comparison of the reconstruction efficiency from the J/ψ tag and probe and the Z tag and probe analyses using 2011 ATLAS data. The J/ψ measurement is for the p_T range from 8 GeV to 15 GeV while the Z measurement is from the p_T range from 15 GeV to 20 GeV.

5.3   Scale and Resolution

Practically speaking, muon scale and resolution corrections must be parameterized in some way. In ATLAS, the Z-resonance is used to understand the ways in which the muon momentum scale and the resolution should be corrected in Monte Carlo simulated data [6, 36]. Various parameters are used that help correct the invariant mass shape of the $Z \rightarrow \mu\mu$ resonance in Monte Carlo to match the shape in data. Among the parameters, s^{det} functions as a scale correction for the transverse momentum while Δa^{det} and Δb^{det} are resolution smearing parameters which affect the momentum spread. The Δa resolution parameter is a flat resolution smearing correction. This parameter describes the multiple scattering contribution to the resolution. The Δb parameter is a resolution parameter which scales linearly in p_T. It is related to the intrinsic resolution of the detector and any residual misalignment.

Equation 5.2 show how these smearing and scaling parameters are used to correct

the muon momentum.

$$p_{\mathrm{T}}^{Cor,det} = p_{\mathrm{T}}^{MC,det} \cdot s^{det}\left(\eta\right)\left(1 + \Delta a^{det}(\eta)G(0,1) + \Delta b^{det}G(0,1)p_{\mathrm{T}}^{MC,det}\right) \qquad (5.2)$$

The superscript is used to refer to muon momentum as measured by either the Inner Detector, $det = ID$ or the Muon Spectrometer, $det = MS$. Where $G(0,1)$ is a Gaussian distributed random variable with a mean of 0 and a width of 1. To fit for the correction parameters, the $Z \rightarrow \mu\mu$ peak is considered in data and in MC. The data is split into 16 regions in η. A binned likelihood fit is used that varies the correction parameters on the MC muons to get the optimal agreement between data and MC in the $Z \rightarrow \mu\mu$ invariant mass peak. To avoid degeneracy in the corrections, for the initial fit, only muons which are in the same region are used. After corrections have been calculated for muons from a specific η region, muons from that η-region can be used for subsequent fits as their corrections are now determined. The fit is then iterated over all η bins. After calculating all corrections, the fit is iterated twice to ensure the correction parameters are stable.

From other studies, it is found that the Δa^{MS} and Δb^{ID} terms are negligible. This is because the multiple scattering component of the MS tracks and the alignment of the ID are well understood and well modeled in simulated MC events.

The result of applying these corrections to MC is found in Figure 5.16. The upper plot shows the comparison between $Z \rightarrow \mu\mu$ data and MC without any corrections. The lower plot shows the comparison after correcting the MC using the procedure outlined above. This constructed agreement indicates that the correction parameters are properly estimated.
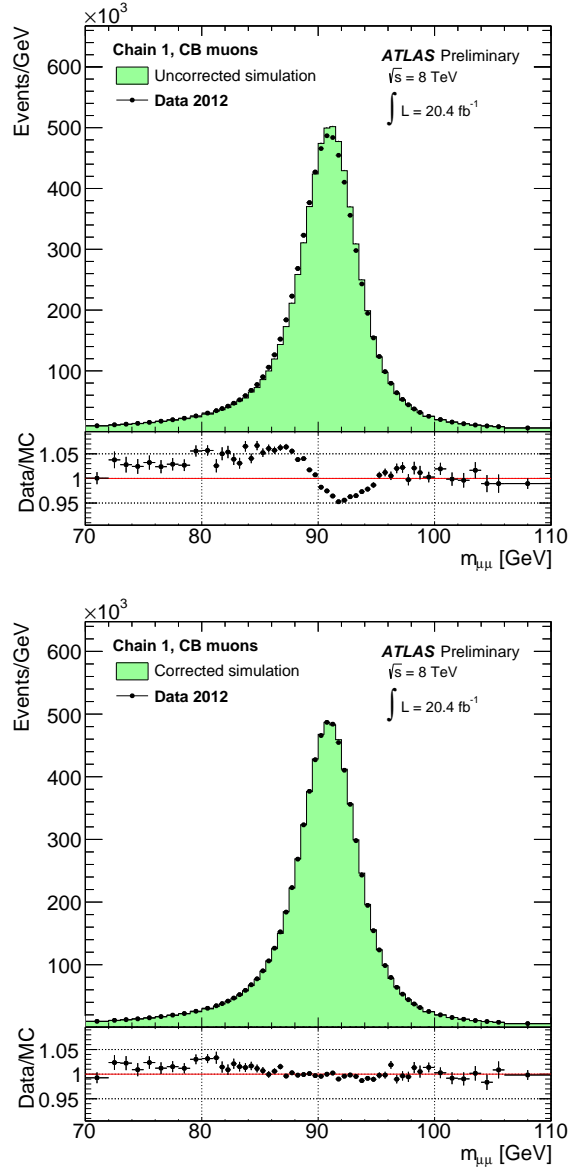
Figure 5.16: The di-muon invariant mass for STACO CB muons, isolated and with $p_T > 25$ GeV. 2012 data is shown in black and the POWHEG simulation of $Z \to \mu\mu$ plus background events is shown in green. On the upper plot, no corrections smearing or scale muon momentum corrections are applied while both smearing and scale corrections are applied to the plot below. [6]

5.4   Conclusions

At low p_T, the muon efficiency was measured in data and MC samples as a function of the muon p_T and η using muons from J/ψ decays. At high p_T, the Z resonance

91

is used for the same purpose. Using the understanding of muon efficiency at low-p_T, the cuts on muon p_T can be relaxed in the Higgs analysis increasing the number of signal events which pass selections. Furthermore, an understanding of the muon reconstruction efficiency makes it possible to compare the expected and observed Higgs event yields and determine whether the observed Higgs cross section agrees with the Standard Model predictions.

Muon scale and resolution corrections are derived using the Z resonance in order to bring the simulated MC and ATLAS data into agreement. These corrections have various terms which are either linear or constant in p_T. When applied the $Z \rightarrow \mu\mu$ line-shape agrees well between MC and data. These corrections will be very important for the Higgs analysis when estimating the width and mass of the Higgs boson.

The systematic uncertainties for these corrections are later included in the Higgs mass, width, and normalization fit as nuisance parameters which can vary providing additional systematic uncertainty on the Higgs parameters. This is discussed at length in Section 7.8.

Chapter 6

Higgs $\rightarrow ZZ^{(*)} \rightarrow 4\ell$ Analysis

6.1 Introduction

This chapter describes the event selection for the Higgs analysis. The goal is to select events with two same-flavor opposite-sign dilepton pairs, henceforth called the quadruplet. The Higgs candidates are categorized into four subchannels: $4e$, 4μ, $2\mu2e$, and $2e2\mu$. $4e$ is when both Z-bosons decay to electrons and 4μ is when both Z-bosons decay to muons. In the mixed channels, the leading dilepton pair is the one with an invariant mass closer to the Z-boson mass, this is the one listed first. For $2\mu2e$, the dimuon pair is closer to the Z-boson mass and for $2e2\mu$ the dielectron pair is closer to the Z-boson mass. One advantage of the analysis is that there is a relatively small amount of background contamination. The dominant background is from $(Z^{(*)}/\gamma^*)(Z^{(*)}/\gamma^*) \rightarrow 4\ell$ production, henceforth called the "$ZZ^{(*)}$ background." The production of a Z boson in conjunction with jets where leptons are reconstructed from the jets is another source of background, this is referred to as Z+jets. Di-top

production, $t\bar{t}$, can produce leptons in the top decay chain, and lastly, WZ production with a lepton from b-quark or c-quark jets can mimic the signal.

Because of the low level of background and the very good lepton resolution, the $H \to ZZ^{(*)} \to 4\ell$ channel is ideal for measuring the mass of the Higgs resonance and setting direct limits on the decay width using the four-lepton invariant mass, m_{4l}.

6.2 Data Samples

The measurement is based on a dataset corresponding to an integrated luminosity of 4.6 fb^{-1} at $\sqrt{s} = 7$ TeV and 20.3 fb^{-1} at $\sqrt{s} = 8$ TeV of p-p collisions collected in 2011 and 2012 respectively.

6.3 Simulation Samples

Simulated data is a vital component of the $H \to ZZ^{(*)} \to 4\ell$ analysis. This simulated data is used to determine which selections can be used to select signal events and improve the signal significance $(S/\sqrt{B})$ assuming a Higgs with a mass in the 120-130 GeV range.

The signal $H \to ZZ^{(*)} \to 4\ell$ is modeled using the PowHeg Monte Carlo generator [37, 38]. The primary Higgs production modes of gluon-gluon fusion (ggF) and vector boson fusion (VBF) are calculated independently using next to leading order (NLO) matrix elements. The Higgs transverse momentum (p_T) spectrum is reweighted to a p_T spectrum calculated using higher order theory corrections. The showering and hadronization is done using Pythia 8.1 [39] which is subsequently

interfaced to PHOTOS [40] for final state radiation (FSR) quantum electrodynamic (QED) corrections.

The $ZZ^{(*)}$ background is modeled using the POWHEG generator for the quark quark production mode and using GG2ZZ for the gluon gluon fusion production mode [41]. The Z+jets background is modeled with ALPGEN [42] and then interfaced to PYTHIA 8.1 for hadronization and parton showering [39]. Due to the difficulty in modeling the Z+jets background, data is used to normalize the background using control regions. This procedure is discussed in Section 6.4.4. The last two backgrounds are $t\bar{t}$ and WZ. The $t\bar{t}$ background is modeled with POWHEG and then interfaced with PYTHIA 8.1 for hadronization and parton showering. WZ is modeled with SHERPA [43].

After generation and parton shower hadronization, the events must be run through a simulation which models the interaction of these "generator level" particles with the ATLAS detector. GEANT4 is the program used for detector simulation [32]. GEANT4 takes the particles and simulates their interaction with matter and the magnetic field found in the ATLAS detector. Minimum bias (pile-up) events are simulated separately and these pile-up events are superimposed onto the simulated events.

6.4 Event Selection

The analysis uses a large number of trigger paths. The analysis requires events with multiple leptons at different momenta. To improve the overall triggering efficiency, the OR of many lepton triggers is used. The $p_{\mathrm{T}}/E_{\mathrm{T}}$ thresholds used in the 2011 data is detailed in Table 6.1. Halfway through 2011, the E_{T} threshold for the

electron triggers changed leading to two different triggers for the early and later run periods. Table 6.2 shows the trigger p_T/E_T thresholds used for 2012 data. The different trigger paths include additional criteria in excess of the the simple p_T/E_T thresholds. These additional criteria explain why multiple single lepton triggers are used despite having overlapping thresholds. The 2012 run has higher luminosity than 2011, accordingly the p_T threshold of the lowest p_T single lepton trigger was raised with respect to 2011 to keep data collection rates manageable.

Table 6.1: Trigger thresholds used in 2011 data for the $H \rightarrow ZZ^{(*)} \rightarrow 4\ell$ analysis.

Single Lepton Triggers	
Channel	Threshold
4μ	$p_T > 18$ GeV
$4e$	$E > 20$ GeV (early run periods) $E > 22$ GeV (later run periods)
$2\mu 2e$	Single lepton trigger used for 4μ OR $4e$

Dilepton Triggers		
Channel	Threshold 1	Threshold 2
4μ	$p_{T1} > 10$ GeV	$p_{T2} > 10$ GeV
$4e$	$E_1 > 12$ GeV	$E_2 > 12$ GeV
$2\mu 2e$	$p_{T,\mu} > 10$ GeV	$E_e > 10$ GeV
	Dilepton trigger used for 4μ OR $4e$	

The triggering efficiency, as calculated using $m_H = 130$ GeV MC, was found to be 97.6% for the 4μ channel, 97.3% in the $2e2\mu$ mixed channel, and 99.7% in the $4e$ channel.

Table 6.2: Trigger thresholds used in 2012 data for the $H \to ZZ^{(*)} \to 4\ell$ analysis.

Single Lepton Triggers	
Channel	Threshold
4μ	$p_{\mathrm{T}} > 24$ GeV (low p_{T} trigger)
	$p_{\mathrm{T}} > 36$ GeV (high p_{T} trigger)
$4e$	$E > 25$ GeV (low E trigger)
	$E > 60$ GeV (high E trigger)
$2\mu2e$	Single lepton trigger used for 4μ OR $4e$

Dilepton Triggers		
Channel	Threshold 1	Threshold 2
4μ	$p_{\mathrm{T}1} > 13$ GeV	$p_{\mathrm{T}2} > 13$ GeV
	$p_{\mathrm{T}1} > 18$ GeV	$p_{\mathrm{T}2} > 8$ GeV
$4e$	$E_1 > 12$ GeV	$E_2 > 12$ GeV
$2\mu2e$	$p_{T,\mu} > 8$ GeV	$E_e > 12$ GeV
	$p_{T,\mu} > 8$ GeV	$E_e > 24$ GeV
	Dilepton trigger used for 4μ OR $4e$	

6.4.1 Muon Preselection

There are four primary types of muons used by the $H \to ZZ^{(*)} \to 4\ell$ analysis. These are combined muons, segment tagged muons, stand-alone muons, and calorimeter tagged muons. These muon types are introduced in Section 5.1.2. The best measured muons are the combined and the segment tagged muons and these muon types are used when possible. Calorimeter tagged and stand alone muons are included primarily to improve the signal yield in regions of the detector where combined muons cannot be reconstructed.

Combined and segment tagged muons are accepted when they have a $p_{\mathrm{T}} > 6$ GeV and and $|\eta| < 2.7$. Calorimeter tagged muons are used only for the region in which there is no coverage from the muon spectrometer. This is the central region and thus calorimeter tagged muons are accepted when they have $p_{\mathrm{T}} > 15$ GeV and $|\eta| < 0.1$.

Stand-alone muons are only used in the forward regions where the inner detector has no coverage, thus these muons are required to have $p_{\mathrm{T}} > 6$ GeV, $|\eta| > 2.5$, and $|\eta| < 2.7$. For the muons which have an inner detector component (CB, ST, and CT), certain ID hit conditions are required in addition to the conventional ID track reconstruction. These inner detector (ID) hit requirements are detailed in Table 6.3. The transverse impact parameter cut, $|d_0| < 1$ mm and longitudinal impact param-

Table 6.3: ID hit requirements for muons in the $H \rightarrow ZZ^{(*)} \rightarrow 4\ell$ analysis.

ID Hit requirements 2011	
ID Si hit requirement	Expect B-layer hit = false or Number of B-layer hits ≥ 1
	No. of Pixel hits + No. of crossed dead Pixel sensors > 1
	No. of SCT hits + No. of crossed dead SCT sensors > 5
	No. of Pixel holes + No. of SCT holes < 3
TRT Hit Requirements: $|\eta| < 1.9$	Hits + Outliers > 5 & $\frac{Outliers}{Hits+outliers} < 0.9$
TRT Hit Requirements: $|\eta| \geq 1.9$	if (Hits + Outliers > 5): $\frac{Outliers}{Hits+outliers} < 0.9$
ID Hit requirements 2012	
ID Si hit requirement	No. of Pixel hits + No. of crossed dead Pixel sensors > 0
	No. of SCT hits + No. of crossed dead SCT sensors > 4
	No. of Pixel holes + No. of SCT holes < 3
TRT Hit Requirements: $0.1 < |\eta| \leq 1.9$	Hits + Outliers > 5 & $\frac{Outliers}{Hits+outliers} < 0.9$

eter cut, $|z_0| < 10$ mm, are used to reject cosmic muons. The primary vertex is defined as the vertex with the highest $\sum p_{\mathrm{T}}^2$ of associated tracks. A ΔR overlap cut is applied which rejects stand alone or calorimeter tagged muons which are too close to a combined or segment-tagged muon. For CT muons the cut is $\Delta R < 0.1$ and for SA muons the cut is $\Delta R < 0.2$. In Monte Carlo certain p_{T} smearings are applied that are intended to improve the agreement between the Monte Carlo and data. These corrections are discussed in Chapter 5.

6.4.2 Electron Preselection

Electrons from 7 TeV data are required to pass a cut-based selection which uses tracking and shower profile criteria [44]. For the 8 TeV data, an improved reconstruction algorithm was used. This improved algorithm utilizes a likelihood-based electron identification that lowers the fake rate and increase the electron reconstruction efficiency [45].

Regardless of how they were reconstructed, the electrons in the $H \rightarrow ZZ^{(*)} \rightarrow 4\ell$ analysis are required to have $E_T > 7$ GeV and a pseudo-rapidity cut of $|\eta_{cluster}| < 2.47$. As with the muons, there is a cut on the longitudinal impact parameter, $|z_0| < 10$ mm to reject cosmic tracks.

6.4.3 Quadruplet Selection

The goal is to select events with four or more leptons comprising two opposite-sign same-flavor dilepton pairs. For the $m_H < 184$ GeV region, one of these dilepton pairs should be consistent with the decay of an on-shell Z-boson. Furthermore, only one stand-alone or calorimeter-tagged muon is allowed in a quadruplet. This is to prevent too many poorly measured or heavy flavor decay muons in a candidate event. The leptons in the primary dilepton pair are required to have $p_{T,1} > 20$ GeV and $p_{T,2} > 15$ GeV. The highest p_T lepton in the secondary dilepton pair is required to have $p_{T,3} > 10$ GeV. The lowest p_T lepton in the secondary dilepton pair is simply required to pass the lepton preselections: $p_T > 6$ GeV for muons and $E_T > 7$ GeV for electrons. The primary dilepton pair is required to have an invariant mass of 50 GeV $< m_{12} < 106$ GeV. The secondary dilepton pair is required to pass a cut of

$m_{min} < m_{34} < 115$ GeV. The parameter, m_{min}, takes the value of 12 GeV for $m_{4l} <$ 140 GeV and increases linearly between 12 and 50 GeV for $140 < m_{4l} < 190$ GeV. When $m_{4l} \geq 140$ GeV, $m_{min} = 50$ GeV. To prevent overlap, a ΔR separation is enforced, for same flavor leptons this cut is set at $\Delta R_{l_i,l_j} > 0.1$ and for opposite flavor leptons the cut is $\Delta R_{l_i,l_j} > 0.2$. Lastly, a J/ψ veto is applied: if any dilepton same flavor opposite charge pair has an invariant mass of $m_{l_i,l_j} < 5$ GeV the event is removed. To help reject events where the lepton was produced from a b-jet or other non-prompt process, track and calorimeter isolation cuts are applied. The track isolation variable is the sum of the transverse momentum of tracks in a certain ΔR cone around a particle divided by the p_T (or E_T for electrons) of the particle in question. This definition is given by Equation 6.1.

$$\frac{\sum_{\Delta R_{i,l}} p_{T,i}}{p_{T,l}} \tag{6.1}$$

The definition of calorimeter isolation is similar. The calorimeter isolation is the sum of the energy deposited in the calorimeter in a cone around a particle divided by the transverse momentum (or energy for electrons) of the particle.

$$\frac{\sum_{\Delta R_{i,l}} E_i}{p_{T,l}} \tag{6.2}$$

The values of the cuts on track and calorimeter isolation are found in Table 6.4.

In addition to the isolation requirements, both electrons and muons must pass impact parameter significance cuts: for muons, $\frac{|d_0|}{\sigma_{d_0}} < 3.5$ and for electrons, $\frac{|d_0|}{\sigma_{d_0}} < 6.5$. This cut is to prevent non-prompt electrons and muons, typically from heavy-flavor decay, from being included in the analysis.

Four muon and four electron candidates have multiple ways in which they can be paired. Also in events with five or more leptons there are multiple quadruplet pairings.

Table 6.4: Track and calorimeter isolation cuts.

	Track Isolation
2011	(Cone $\Delta R < 0.2$) $< 15\%$ for muons and electrons
2012	(Cone $\Delta R < 0.2$) $< 15\%$ for muons and electrons
	Calorimeter Isolation
2011	(Cone $\Delta R < 0.2$) $< 20\%$ for electrons
	(Cone $\Delta R < 0.2$) $< 30\%$ for CB, ST, CT muons
	(Cone $\Delta R < 0.2$) $< 15\%$ for SA muons
2012	(Cone $\Delta R < 0.2$) $< 30\%$ for electrons
	(Cone $\Delta R < 0.2$) $< 30\%$ for CB, ST, CT muons
	(Cone $\Delta R < 0.2$) $< 15\%$ for SA muons

If multiple quadruplets pass the selections for different channels from a single event, the quadruplet from the channel with the highest expected rate is selected, this is, in order: 4μ, $2e2\mu$, $2\mu2e$, and $4e$. Otherwise, the quadruplet with leading dilepton mass closest to the Z mass is selected. If two quadruplets have the same leading dilepton mass, the one with the larger sub-leading dilepton mass is chosen.

6.4.4 Background Estimation
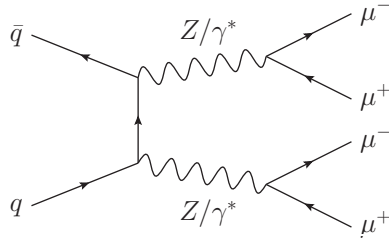
Figure 6.1: The primary leading order Feynman diagram for the Standard Model ZZ background and its decay to muons.

The primary background to the analysis is the $ZZ^{(*)}$ background. The leading Feynman diagram for this background is seen in Figure 6.1. Because the topology is

the same as the signal, this background is referred to as an irreducible background. The $ZZ^{(*)}$ background has four real leptons and can be reliably estimated from Monte Carlo. The shape of the $ZZ^{(*)}$ background is taken from simulated events and normalized to NLO calculations [46].

The reducible background production modes are Z+jets, $t\bar{t}$, and WZ. Each of these backgrounds typically involves at least one lepton reconstructed from a jet or other hadronic process. These reducible backgrounds are difficult to model in MC and they are estimated with data-driven techniques. This is done separately by splitting the final states into $ll + \mu\mu$ and $ll + ee$.

In the $ll + \mu\mu$ final state, the dominant contribution from Z+jets is $Z+b\bar{b}$ in which the b-quarks semileptonically. A small contribution also comes from π/K in-flight decays. The Z+jets and $t\bar{t}$ backgrounds can be distinguished from one another using the m_{12} distribution. Z+jets will be sharply peaked near the Z-mass whereas $t\bar{t}$ appears much more broad. Four control regions are defined with respect to the baseline analysis cuts as follows:

- At least one subleading muon with the impact parameter significance cut inverted. This is to enhance the heavy flavor contribution.

- At least one subleading muon with the isolation cut inverted to enhance the contribution of π/K decays in flight.

- Require the subleading muons to be same-sign. This includes all contributions except the normal SM $ZZ^{(*)}$ background.

- Require the leading dilepton pair to be opposite flavor, $e\mu$, with either a same

or opposite sign subleading muon pair. This removes the Z+jets contribution.

The yields from these different control regions are extrapolated to the signal region using efficiencies obtained from MC simulation. The small component from WZ decay is estimated directly from MC.

The electron backgrounds in the $ll + ee$ final states tend to arise from jets that are misidentified as electrons. This can happen in three ways: 1) light flavor hadrons such as the $\pi^{\pm}$ misidentified as electrons 2) photon conversion to electron pairs 3) electrons from heavy flavor decay. These shapes are evaluated using a "3l+X" control region. The control region requires the three highest p_{T} leptons to satisfy the full analysis selections. The fourth lepton (X) is chosen so that the electron identification requirements are fully relaxed. The only requirement is that there be seven or more hits in the silicon layers of the ID with at least one of them occurring in the pixels. To minimize the contribution from the $ZZ^{(*)}$ background, the X and the other subleading electron are required to have the same sign. The normalizations of the three background components of X are extracted with a fit to the number of hits in the B-layer (the first layer of the pixels) and the high-threshold to low-threshold TRT hit ratio. The light-flavor hadrons will have a different high-threshold to low-threshold TRT hit ratio than the real electrons from heavy flavor decay. Meanwhile, photon conversions will be unlikely to leave any hits in the B-layer. The normalizations from different background components in the control region are extrapolated to the signal region using efficiencies determined using a large sample of Z bosons which were produced with a single additional candidate satisfying the relaxed selections detailed above.

The normalizations for the backgrounds using the above techniques are presented in Section 6.5 in Table 6.5 for the 120-130 GeV invariant mass range.

6.4.5   Final State Radiation Recovery

In the analysis, two types of final state radiation (FSR) are considered and corrected for. Collinear FSR is angularly close to the particle from which it originated while far FSR (also called non-collinear FSR) occurs when the FSR candidate is produced at a large angle relative to the parent particle. Collinear FSR is only considered for muons while far FSR can be added back to both electrons and muons. To account for collinear FSR, a search is performed on each muon looking for FSR candidates. A candidate can be a standard reconstructed electron or photon cluster which satisfies the following requirements:

- The transverse energy of the cluster is greater than 3.5 GeV.

- The cone between the cluster and the muon is $\Delta R_{cluster,\mu} < 0.15$.

- The fraction of the cluster energy deposited in the pre-sampling layer of the electromagnetic calorimeter divided by the total energy is greater than 10%.

Additionally, a candidate can be a simple 3×5 energy cluster provided it satisfies the following requirements:

- The transverse energy of the cluster is $1.5 \text{ GeV} < E_{\text{T}} < 3.5 \text{ GeV}$.

- The cone between the cluster and the muon $\Delta R_{cluster,\mu} < 0.15$.

- The fraction of the cluster energy deposited in the pre-sampling layer of the electromagnetic calorimeter divided by the total energy is greater than 10%.

A search is also performed which looks for far FSR candidates. Far FSR candidates must be photon objects which pass tight identification criteria and the following cuts:

- The cone between the cluster and the lepton is $\Delta R_{cluster,l} > 0.15$.

- The transverse energy of the cluster must pass $E_{\mathrm{T}} > 10$ GeV

- The FSR candidate must be isolated $\sum_{\Delta R < 0.40} E_{\mathrm{T}} < 4$ GeV.

A maximum of one FSR candidate is used per event. Priority is given to collinear FSR candidates provided the invariant mass of the corresponding dilepton pair to which the FSR candidate is associated satisfies $66 < m_{\mu\mu} < 89$ GeV and after the correction, the three-body invariant mass satisfies $m_{\mu\mu\gamma} < 100$ GeV. Only FSR candidates corresponding to leptons from the leading dilepton candidate will be considered. If multiple FSR candidates exist, the one with the highest cluster E_{T} is selected.

If no collinear FSR candidates are added into the event, the highest far FSR photon with the highest E_{T} passing $m_{ll} < 81$ GeV and $m_{\ell\ell\gamma} < 100$ GeV will be selected. The FSR candidate must be associated with the leading dilepton pair.

From MC-studies, it is expected that around 4% of events will have a collinear FSR-correction applied and 1% will have a non-collinear FSR-correction applied. These same studies show that around 85% of corrected events have a genuine FSR photon while the remaining FSR-candidates originated from pile-up or muon-ionization.

6.4.6 Z Mass Constraint

The mass resolution of the 4-lepton invariant mass is limited by the intrinsic width of the Z-boson which is an intermediate decay product. The probability distribution of the true mass of the Z-boson, m_Z^{true}, given the measured dilepton mass, m_Z^{reco}, can be written as follows:

$$p\left(m_Z^{true}|m_Z^{reco}\right) \propto p\left(m_Z^{reco}|\sigma_{m_Z^{reco}}, m_Z^{true}\right) \cdot p\left(m_Z^{true}|m_Z, \Gamma_Z\right) \qquad (6.3)$$

On the right hand side, we have $p\left(m_Z^{reco}|\sigma_{m_Z^{reco}}\right)$ which can be thought of as an invariant mass response function. Meanwhile the second term: $p\left(m_Z^{true}|m_Z, \Gamma_Z\right)$ can be thought of as the relevant truth distribution which should be a Breit-Wigner.

To apply a mass-constraint on a very narrow resonance such as the J/ψ, one can simply replace the m_Z^{reco} with the mass of the resonance. For the Z resonance, however, the natural width is not negligible compared to the detector resolution. In fact, both are on the GeV scale. To perform a Z-boson mass constraint constraint in this regime the goal is to not just select the pole Z mass but to find the maximum likelihood value of the m_Z^{true} for a given reconstructed mass value. This method tries to correct the particle momenta to the most likely true Z mass using a gaussian resolution model for the uncertainty on the momenta and a Breit-Wigner distribution for the distribution of the m_Z^{true}.

The effect of the Z-boson mass constraint on the mass of the leading Z and on the 4-lepton invariant mass is seen in Figure 6.2. The effect is to narrow the peak in the 4-lepton invariant mass distribution while in the leading Z-boson mass, the effect is to bring the values closer to the pole mass of the Z-boson.

Although the Z-boson mass constraint is very useful in decreasing the width of a
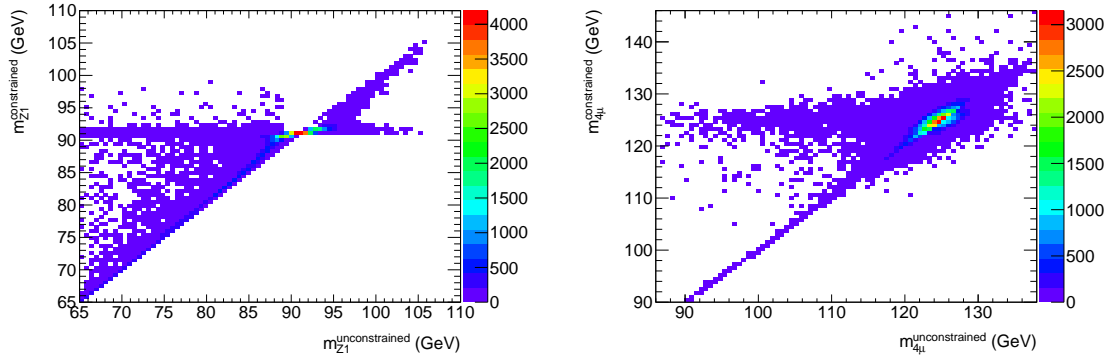
Figure 6.2: Left: the effect of the Z-boson mass constraint on the reconstructed mass of the leading Z for the 4μ channel, the y-axis shows the reconstructed Z-boson mass after constraint and the x-axis is the reconstructed Z-boson mass before constraint. Right: the effect of the Z-boson mass constraint on the reconstructed 4-lepton invariant mass system, the y-axis shows the reconstructed 4-lepton mass after constraint and the x-axis is the 4-lepton mass before constraint.

Monte Carlo based template signal model, the Z-boson mass constraint is not used in a per-event framework because the mass constraint makes it difficult to parameterize the response functions.

6.4.7 ZZ Discriminant

To help differentiate between signal and background events, a boosted decision tree (BDT) is used to increase the separation between the signal and the irreducible $ZZ^{(*)}$ background [47]. This BDT is later used in the mass and width fitting as a second dimension to be used in conjunction with the invariant mass. Because the BDT uses the kinematic information from each event, it can be thought of as an encapsulation of the kinematics for the event. The BDT is trained on signal and background MC samples. Higgs MC with $m_H = 125$ GeV is used as the signal sample while SM $ZZ^{(*)}$ MC is used for the background. All events are required to pass the analysis selections

and only events in the invariant mass window of $115 < m_{4l} < 130$ GeV are used. The BDT uses three variables: the η of the 4-lepton system, the p_T of the 4-lepton system, and a Matrix-Element based kinematic discriminant (KD). Mathematically the expression for the KD is seen in Equation 6.4.

$$KD = log\left(\frac{ME_{sig}^2}{ME_{ZZ}^2}\right) \tag{6.4}$$

Where ME_{sig} is the Matrix-Element of the Higgs signal and ME_{ZZ} is the Matrix-Element of the $ZZ^{(*)}$ background. Because these Matrix-Elements are based on the four 4-vectors of the leptons, this KD encapsulates the kinematic information about the event as it pertains to signal-background discrimination. The Matrix-Element itself is calculated at lowest order using MADGRAPH [48] by using the $H \rightarrow ZZ^{(*)} \rightarrow 4\ell$ process as the signal process and $q\bar{q} \rightarrow 4\ell$ as the background process. On an event-by-event basis, the Higgs mass variable is set to be the reconstructed m_{4l} before FSR corrections and the Z-mass constraint of the event. Figure 6.3 shows the inputs on which the BDT is trained.

Figure 6.4 shows the boosted decision tree discriminant and its value for both signal and background Monte Carlo samples. This BDT discriminant ranges from -1 to 1 with -1 being most background-like and 1 being most signal-like. As is seen in Figure 6.4, the BDT discriminant provides very good separation between the signal and background. The BDT is trained separately for $4e$, 4μ, and the mixed $2e2\mu$ and $2\mu2e$ channels.
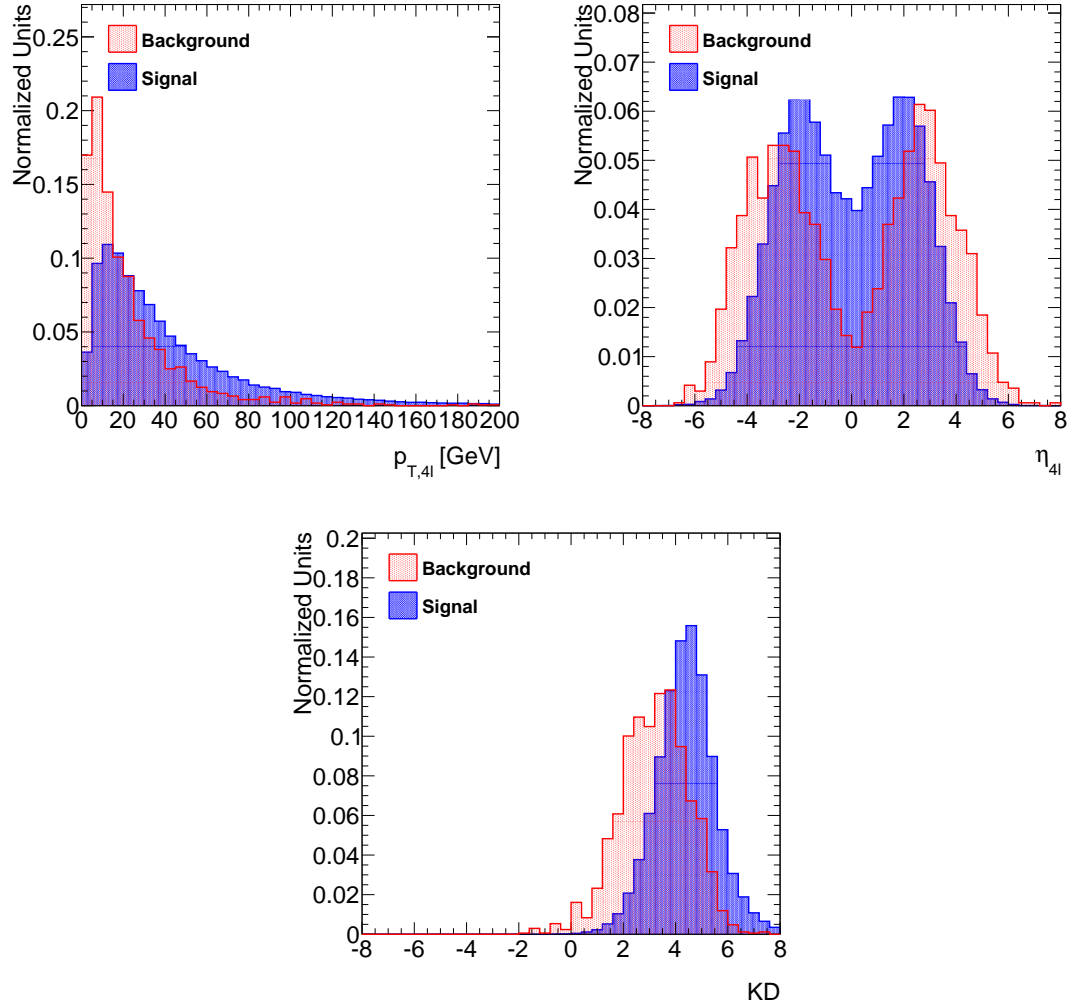
Figure 6.3: Plots of $p_{T,4l}$, η_{4l}, and KD for Higgs signal MC and $ZZ^{(*)}$ background MC. These variables are the inputs on which the BDT is trained.
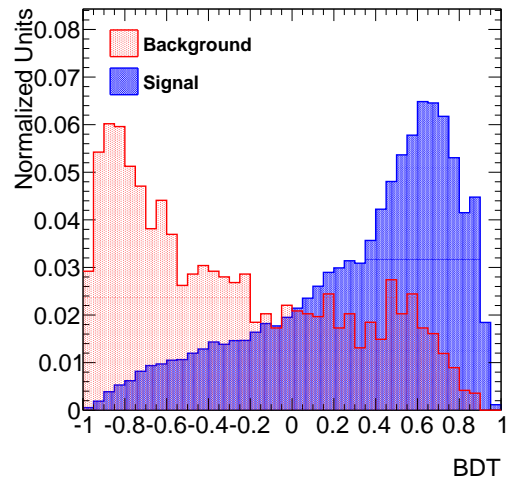
Figure 6.4: Boosted decision tree (BDT) variable for Higgs signal MC and $ZZ^{(*)}$ background MC.

6.5   Conclusions

The event yields in the 120 GeV $< m_{4l} <$ 130 GeV range after the Z-mass con-
straint are presented numerically in Table 6.5 with the total systematic uncertainty
stated. Assuming the existence of a SM Higgs with a mass of 125 GeV, we expect
26.5±1.7 events in the 120-130 GeV range. An excess of 10 events is observed in data,
resulting in a higher than expected production cross section for the $H \rightarrow ZZ^{(*)} \rightarrow 4\ell$
analysis.

Table 6.5: The number of expected signal ($m_H = 125$ GeV), expected background,
and observed data events after the event selection cuts within the 120 GeV $< m_{4l} <$
130 GeV range after the Z-mass constraint. The quoted uncertainties represent the
systematic uncertainty on the various signal and background normalizations.

Final State	Signal	$ZZ^{(*)}$	Z+jets,$t\bar{t}$	s/b	Expected	Observed
			$\sqrt{s} = 7$ TeV			
4μ	0.91 ± 0.09	0.46 ± 0.02	0.10 ± 0.04	1.7	1.47 ± 0.10	2
$2e2\mu$	0.58 ± 0.06	0.32 ± 0.02	0.09 ± 0.03	1.5	0.99 ± 0.07	2
$2\mu2e$	0.44 ± 0.04	0.21 ± 0.01	0.36 ± 0.08	0.8	1.01 ± 0.09	1
$4e$	0.39 ± 0.04	0.19 ± 0.01	0.40 ± 0.09	0.7	0.98 ± 0.10	1
Total	2.32 ± 0.23	1.17 ± 0.06	0.96 ± 0.18	1.1	4.45 ± 0.30	6
			$\sqrt{s} = 8$ TeV			
4μ	5.28 ± 0.52	2.36 ± 0.12	0.69 ± 0.13	1.7	8.33 ± 0.6	12
$2e2\mu$	3.45 ± 0.34	1.67 ± 0.08	0.60 ± 0.10	1.5	5.72 ± 0.37	7
$2\mu2e$	2.71 ± 0.28	1.17 ± 0.07	0.36 ± 0.08	1.8	4.23 ± 0.30	5
$4e$	2.38 ± 0.25	1.03 ± 0.07	0.35 ± 0.07	1.7	3.77 ± 0.27	7
Total	13.8 ± 1.4	6.24 ± 0.34	2.00 ± 0.28	1.7	22.1 ± 1.5	31
			$\sqrt{s} = 7$ TeV and $\sqrt{s} = 8$ TeV			
4μ	6.20 ± 0.61	2.82 ± 0.14	0.79 ± 0.13	1.7	9.81 ± 0.64	14
$2e2\mu$	4.04 ± 0.40	1.99 ± 0.10	0.69 ± 0.11	1.5	6.72 ± 0.42	9
$2\mu2e$	3.15 ± 0.32	1.38 ± 0.08	0.72 ± 0.12	1.5	5.24 ± 0.35	6
$4e$	2.77 ± 0.29	1.22 ± 0.08	0.76 ± 0.11	1.4	4.75 ± 0.32	8
Total	16.2 ± 1.6	7.41 ± 0.40	2.95 ± 0.33	1.6	26.5 ± 1.7	37

Using the selections and background modeling briefly discussed in this section, the
data can be compared to the background shapes and normalizations. This comparison

is shown in Figure 6.5. On the left, the m_{4l} distribution of data events (shown in black) is compared to the $ZZ^{(*)}$ background in red, the reducible backgrounds in purple, and the Higgs MC ($m_H = 125$ GeV) signal in blue. The signal model is scaled up by a signal strength of 1.66 to account for the excess of observed events in data. This signal strength was measured using a 2D-template approach detailed in [7]. On the right, the same comparison between data and signal/background shapes is shown in 2D using the m_{4l} and BDT as observables.
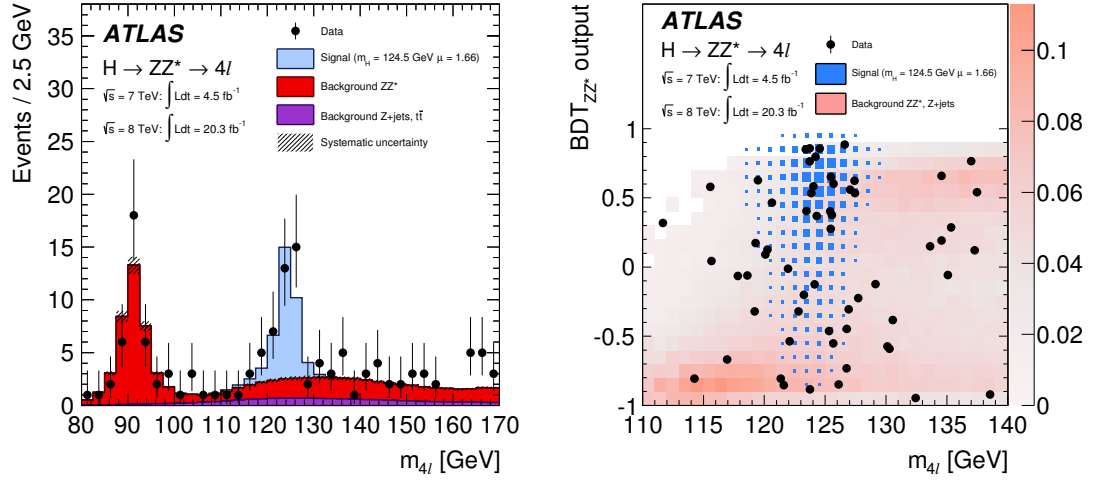
Figure 6.5: Left: distribution of the four-lepton invariant mass for the selected candidates in the m_{4l} range $80 - 170$ GeV for the combined 7 TeV and 8 TeV data samples. Superimposed are the expected distributions of a SM Higgs boson signal with $m_H = 124.5$ GeV normalized to the measured signal strength, as well as the expected $ZZ^{(*)}$ and reducible backgrounds. Right: distribution of the BDT output, versus m_{4l} for the selected candidates in the $110 - 140$ GeV m_{4l} range for the combined 7 TeV and 8 TeV data samples. The expected distribution for a SM Higgs with $m_H = 124.5$ GeV is indicated by the size of the blue boxes, and the total background is indicated by the intensity of the red shading [7].

Chapter 7

Mass and Width Measurement

7.1 Introduction

To measure the width and mass of the Higgs resonance, it is necessary to understand how these parameters affect the observables measured by the ATLAS detector. The observables are the four-lepton invariant mass and the kinematics of the four leptons while the parameters of interest are the Higgs mass, width, and signal strength. To relate these observables to the parameters of interest, we write a probability density function (PDF) which gives the probability that a specific set of observables will be measured for given values of the Higgs parameters.

To construct such a PDF, two approaches can be used. In one, MC simulated data are generated for different values of the parameters. The shape of the MC for a specific observable is used to construct the PDF. Morphings between the MC shapes for different values of the parameters can be performed so that the PDF is continuous.

A second approach starts from the ground up. It works by choosing a class of

functions that describe the shape of the observables and take the parameters of the Higgs as inputs. Because the Higgs boson is an unstable particle, the invariant mass distribution of its decay products can be described by the Breit-Wigner distribution. Furthermore the Breit-Wigner has, as inputs, the mass of the resonance and the width of the resonance. As such it is is a perfect candidate to use for the signal PDF of the Higgs boson. There are, however, a few complications. As discussed in Chapter 4, the ATLAS detector measures the momentum and energy of particles using tracking and calorimetry. These techniques have an intrinsically statistical component that causes the measured momentum/energy to differ from the true momentum or energy of the particle. Accordingly, the reconstructed four-lepton invariant mass will differ from the true four-lepton invariant mass. The function that relates the measured four-lepton invariant mass to the true four-lepton invariant mass is called the mass response function. By convolving the mass response with the Breit-Wigner, it is possible to transform the underlying Breit-Wigner distribution into a distribution that describes the shape of the four-lepton invariant mass at reconstruction level. This procedure is used to describe the shape of the reconstruction level signal distribution and relate the observables to the Higgs parameters. In addition, some leptons may emit radiation before being measured in the detector. This radiation will reduce the measured momentum/energy thereby reducing the reconstructed four-lepton invariant mass. A radiative tail is convolved with the signal model to account for this FSR energy loss. This approach is known as the event-by-event approach because it utilizes resolution information on a per-event level so that the PDF will be tuned specifically to the data events being fit.

The structure of this Chapter is as follows. In Section 7.2, we present the mass response function obtained by combining the lepton momentum response functions. After discussing the math behind this combination, we turn to the calculation of the individual lepton momentum response functions using leptons from MC simulated data in Section 7.2.1 for muons and Section 7.2.2 for electrons. The response functions are then validated with MC and data using the Higgs and Z resonances.

In Section 7.3, the derivation of the signal mass model is considered. As discussed above, this model is formed by convolving the detector mass response function with the truth distribution. The truth invariant mass distribution, which is fundamentally a Breit-Wigner, is shaped by the acceptance effects from the analysis cuts (Section 7.3.1) and the final state radiation that creates a radiative tail (Section 7.3.2). The numerical convolution techniques that are used to speed up the convolution of this modified truth distribution with the mass response are detailed in Section 7.3.4. Finally the signal model is validated using MC.

To further differentiate between signal and background, a ZZ discriminant is computed using various observables as inputs. This ZZ discriminant, also known as the BDT, is used as a second observable in the likelihood maximization along with the invariant mass. Accordingly signal and background models are needed for the BDT. The signal BDT model is derived using smoothed MC based templates in Section 7.4. Similarly, the invariant mass and BDT background models are made using smoothed MC or data-driven templates as discussed in Section 7.5 and Section 7.6.

With all the models used for the likelihood maximization in place, we discuss the relevant systematic uncertainties and how they are treated in the fit. In Section 7.8,

a ranking of these systematic uncertainties is provided and their relative effect on the mass and signal strength measurements is discussed. Lastly, the estimated values of the Higgs mass, width, and signal strength for data and MC are presented in Section 7.10.

7.2 Detector Response Functions

To fit the Higgs mass using event-by-event response information, it is necessary to understand how the Higgs decay products interact with the ATLAS detector. In this analysis, these are the four leptons. It is possible to factorize the Higgs mass response as a combination of the individual kinematic responses of the four leptons.

When a lepton passes through the detector, it will leave a track in the inner detector. Electrons deposit their energy in the electromagnetic calorimeter while muons pass through the calorimeter and leave a track in the muon spectrometer. Using the energy deposited or the hits from these tracks, it is possible to measure the momentum or energy and direction of the lepton. The difference between these measured kinematics and the actual kinematics is known as the lepton detector kinematic response. There is a statistical component to this response. In other words, if identical leptons pass through the exact same portion of the detector, a different set of kinematics will be measured. The ensemble of the difference between the measured and true kinematics comprises the lepton detector response function.

In practice, a few simplifying assumptions are made that reduce the complexity of understanding the lepton response. As seen in Section 4.6, the angular resolution of the ATLAS tracking is very good and the effect of its uncertainty on the invariant mass

is negligible. Because of this, the lepton kinematic response can be approximated by a one dimensional lepton response in momentum or energy. Using this approximation, it is possible to derive a relatively simple expression for the Higgs mass response using individual muon momentum responses. In the following derivation x_i represents a random variable from the momentum weighted lepton momentum/energy response function for the ith lepton, x_H is a random variable from the Higgs mass response, p_H is 4-momentum of the Higgs, p_i is the 4-momentum of the ith muon, and m_H is the mass of the Higgs candidate. The mass response of the Higgs can be related to the individual momentum responses through the following derivation:

$$(p_H)^2 = (m_H)^2 = (p_1 + p_2 + p_3 + p_4)^2 \tag{7.1}$$

$$m_H^2 = \left(\sum_{i=1}^{4} p_i \right)^2 \tag{7.2}$$

$$m_H^2 = \sum_{i=1}^{4} \left(p_i^2 + \sum_{j \neq i} p_i \cdot p_j \right) \tag{7.3}$$

$$m_H^2 = \sum_{i=1}^{4} \left(m_\ell^2 + 2 \sum_{j > i} p_i \cdot p_j \right) \tag{7.4}$$

As the quantities are generic, it holds true for either reconstructed or truth quantities:

$$(m_H^{reco})^2 = \sum_{i=1}^{4} \left(m_l^2 + 2 \sum_{j > i} p_i^{reco} \cdot p_j^{reco} \right) \tag{7.5}$$

The following relations $p_i^{reco} = p_i^{true} (1 + x_i)$ and $m_H^{reco} = m_H^{true} (1 + x_H)$ are used to make substitutions.

$$\left(m_H^{true} (1 + x_H) \right)^2 = \sum_{i=1}^{4} \left(m_l^2 + 2 \sum_{j > i} p_i^{true} (1 + x_i) \cdot p_j^{true} (1 + x_j) \right) \tag{7.6}$$

Because the typical Higgs mass resolution is 1-2 GeV and the m_{4l} values are around 125 GeV, a typical random variable from the Higgs mass response, x_H, is ~ 0.01 and

thus x_H^2 will be on the order of 0.0001 which indicates that the squared terms can be safely ignored.

$$\left(1 + 2x_H + \cancel{x_H^2}^{\;0}\right)\left(m_H^{true}\right)^2 = \sum_{i=1}^{4}\left(m_\ell^2 + 2\sum_{j>i} p_i^{true} \cdot p_j^{true}\left(1 + x_i + x_j + \cancel{x_i x_j}^{\;0}\right)\right)$$
(7.7)

We use equation (7.4) to cancel terms:

$$2x_H\left(m_H^{true}\right)^2 = \sum_{i=1}^{4}\left(2\sum_{j>i} p_i^{true} \cdot p_j^{true}\left(x_i + x_j\right)\right)$$
(7.8)

The final equation for a random variable from the Higgs mass response function is thus:

$$x_H = \frac{1}{\left(m_H^{true}\right)^2}\sum_{i=1}^{4}\left(\sum_{j>i} p_i^{true} \cdot p_j^{true}\left(x_i + x_j\right)\right)$$
(7.9)

To measure the lepton response functions, MC simulated data is used. Later, checks are done to ensure that these response functions can be used in ATLAS data. Leptons are grouped into regions that have a similar response. It is known that passing through physically different regions of the ATLAS muon spectrometer, ATLAS calorimeter, or the ATLAS inner detector will result in a different average response. To account for this, the response is binned in slices of η. Furthermore, leptons of different momenta (or energy for electrons) are likely to have a different response and a second binning axis of p_T (E_T for electrons) is also used. Rather than measure the actual momentum response which would be given by $p_{reco} - p_{truth}$ ($p \to E$ for electrons), the weighted response is used: $\frac{p_{reco} - p_{truth}}{p_{truth}}$. This weighted response accounts for a first order linear dependence on the momentum. Practically speaking, for each lepton, the weighted response, $\frac{p_{reco} - p_{truth}}{p_{truth}}$, is calculated and put into a histogram corresponding to the η and p_T (or E_T for electrons) of the lepton. An additional binning in charge is used

for muons. A functional form is chosen to describes the shape of these response histograms and the response histograms are fit using this chosen function.

7.2.1 Muon Response Functions

Fitting

The function chosen to fit the muon response histograms must be able to describe the main features of this distribution. Looking at a few examples in Figure 7.1, it is clear that the peak is largely Gaussian with a sometimes asymmetric tail. The chosen function must be easy to convolve with other muon momentum response functions using Equation (7.9) to derive the mass response function. Because the peak is already Gaussian and Gaussians are easy to convolve with each other, a sum of Gaussians is an ideal choice when parameterizing the individual muon response functions. For the muons, two Gaussians are sufficient to describe the peak and the tail of the muon momentum response functions. In Figure 7.1, four example fits are shown. The position and width of the tail and peak Gaussians show a certain degree of variability although in general, the tail Gaussian is much smaller and wider than the peak Gaussian. In order to improve the fit stability, a fit function is used which relates the position and width of the tail Gaussian to the width of the peak Gaussian respectively. The formula describing the fitting function is given by Equation 7.10.

$$f(p_T, \eta, q) = f \cdot G(\mu_1, \sigma_1) + (1 - f) \cdot G(\alpha \cdot \sigma_1, \beta \cdot \sigma_1) \qquad (7.10)$$

Where μ_1 is the position of the peak Gaussian, σ_1 is the width of the peak Gaussian, f is the fractional normalization of the peak Gaussian, and α and β are scaling factors
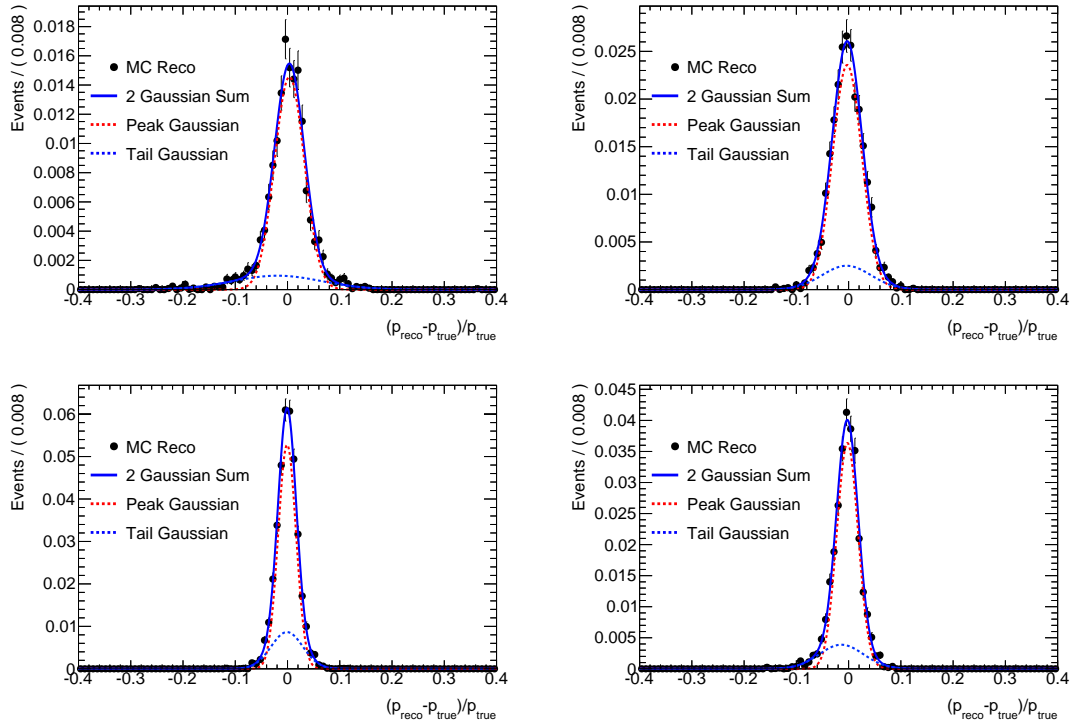
Figure 7.1: Sample response histograms for muons from 8 TeV MC using a 2-Gaussian fit function. Upper left is for is for positively charged muons with $\eta = 2.7$ to 2.4 and $p_T = 6$ GeV to 10 GeV. Upper right is for is for positively charged muons with $\eta = 1.3$ to 1.4 and $p_T = 25$ GeV to 30 GeV. Bottom left is for is for positively charged muons with $\eta = -0.2$ to -0.1 and $p_T = 35$ GeV to 40 GeV. Bottom right is for is for negatively charged muons with $\eta = 0.9$ to 1.0 and $p_T = 30$ GeV to 35 GeV.

which relate σ_1 to the position and width of the tail Gaussian. Constraints are set on β to ensure that the tail Gaussian will always be wider than the peak Gaussian. Additionally, f is constrained to be greater than 0.6 to ensure that the bulk of the distribution will be captured by the peak Gaussian.

The resulting two dimensional map in p_T and η is shown in Figure 7.2 for charge minus CB muons from a variety of 8 TeV Higgs MC samples with masses of 120, 121, 122, 123, 123.5, 124, 124.5, 125, 125.5, 126, 127, 128, 129, and 130 GeV. The muons are from events that have passed the reconstruction level analysis selections

described in Chapter 6. The assumption that the source of the muons does not matter is tested when the muon response functions derived from Higgs samples are validated with the Z-resonance in Section 7.2.1. From this map, it is clear that the peak and tail Gaussians are wider in the high-η and transition regions as would be expected. White areas are those in which insufficient statistics exist to calculate a response function. In these regions, the nearest response function, in p_T, is used. Separate maps are made for muons from the 7 TeV and 8 TeV MC samples. MC is used to populate the response histograms. The muons used are from different Higgs MC samples with different values of m_H. All muons have passed the Higgs selections detailed in Chapter 6.

Equation (7.9) defines the relationship between a random variable in the Higgs mass response and the random variables for the individual lepton momentum responses. This relation is used to combine the muon responses together into a Higgs mass response. This combination gives a 2^4 (16) Gaussian sum, an example of which is seen in Figure 7.3.
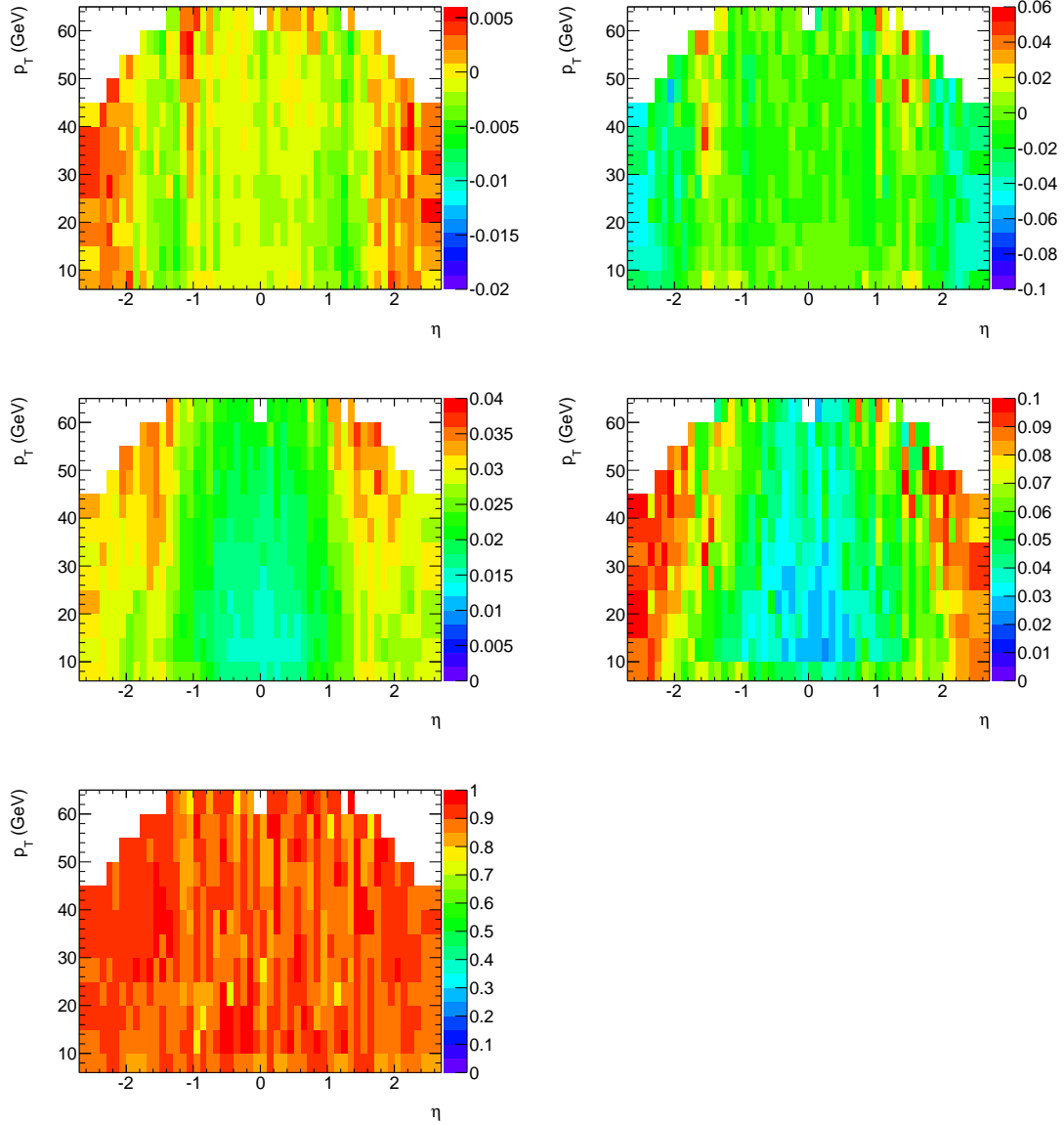
Figure 7.2: The map of the parameters for the two Gaussians in the muon response functions for muons from 8 TeV Higgs MC samples with different m_H. These are binned in p_T and η. The maps shown are for negatively charged muons. The upper left shows mean of the peak Gaussian while the upper right shows the mean of the tail Gaussian. The middle left shows the width of the peak Gaussian while the middle right shows the width of the tail Gaussian. The bottom plot shows the fraction of events in the peak Gaussian.
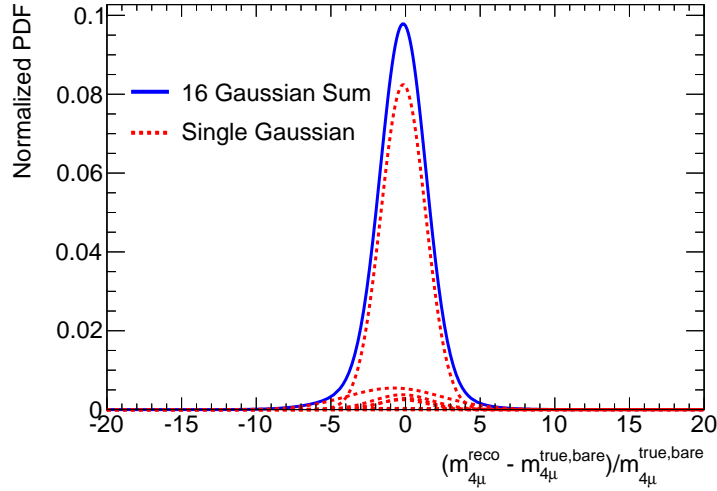
Figure 7.3: Sixteen Gaussian mass response for a single Higgs candidate from MC simulated data.

Validation

After computing the response functions, they can be validated on various MC samples and on data from the ATLAS detector. In MC this validation is done by smearing the truth mass with the mass response calculated for that specific parti-cle: $m_{4l}^{smear} = m_{4l}^{true}(1+x)$ where x is a random number from the mass response function for that particle. Figure 7.4 shows the smeared truth m_{4l} compared to the reconstructed m_{4l} from an 8 TeV Higgs MC sample with $m_H = 125$ GeV. There is good agreement to within the 5% level for the bulk of the distribution. Using the same procedure, a similar validation was done using 8 TeV $Z \to \mu\mu$ MC as shown in Figure 7.5. Again, there is good agreement between the reconstruction mass and the smeared truth model.

The validation can be extended using ATLAS data to ensure that the MC-derived response functions can be used in data. As the ATLAS detector has collected many
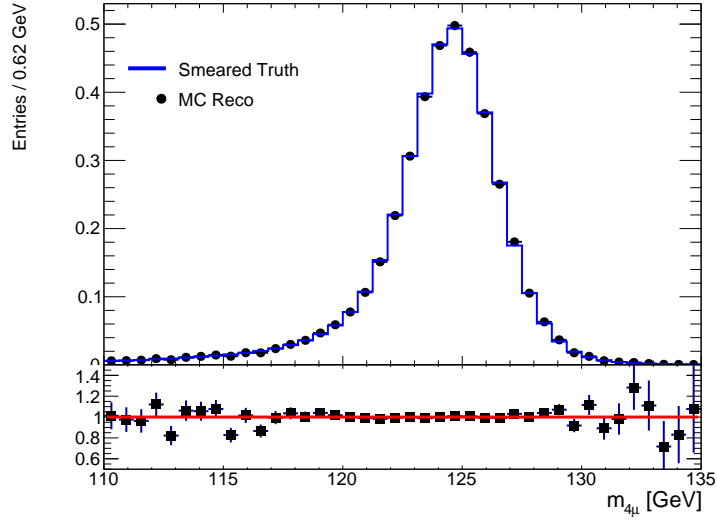
Figure 7.4: Comparison of the truth $m_{4\mu}$ distribution smeared using the muon response functions with the reconstructed $m_{4\mu}$ from 125 GeV Higgs MC generated at 8 TeV.
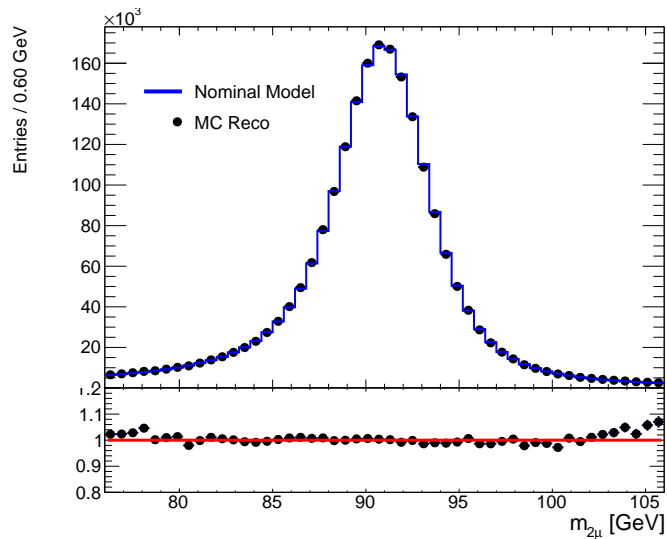
Figure 7.5: Comparison of the truth $m_{2\mu}$ distribution smeared using the muon response functions with the reconstructed $m_{2\mu}$ from 8 TeV $Z \rightarrow \mu\mu$ MC.

millions of di-muon events from the decay of Z-bosons, this resonance is ideal to test the validity of the model. Due to the obvious lack of truth information in ATLAS data, it is not possible to do a simple truth-smearing as was done for the MC. Instead, the truth Z-lineshape, derived from MC simulation, is convolved with the mass-response for each event. The convolutions are then summed together to create the reconstruction-level invariant mass model. Doing a full convolution for millions of events is time consuming and certain speed-ups are possible to reduce the computation time. In particular, using a Monte-Carlo integration rather than a discrete numerical integration greatly speeds up the process. The results of the integration are shown in Figure 7.6 with the MC-integrated model shown in blue and the reconstructed $m_{2\mu}$ from data shown in black. The agreement between the MC-integrated model and the reconstructed $m_{2\mu}$ indicates that the muon response functions can be used to reproduce the reconstruction level lineshape.
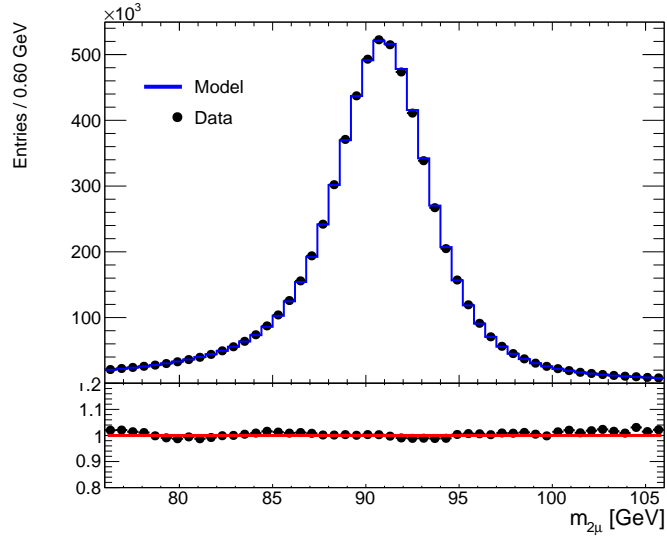
Figure 7.6: The truth Z-lineshape, derived from MC simulation, is convolved with the mass-response for each event from 8 TeV$Z \to \mu\mu$ data. The convolutions are then summed together to create the reconstruction-level invariant mass model seen in blue. The black points are the reconstructed $m_{2\mu}$ for 8 TeV $Z \to \mu\mu$ ATLAS data.

Muon Response Systematics

The scale factors and smearing parameters obtained from the Z and J/ψ resonances discussed in Chapter 5 are used to correct the MC muons so that they agree with the ATLAS data [6]. Each correction has systematic uncertainties associated with them and these systematics will lead to differences in the muon response functions that must be accounted for when using the response functions to produce a signal model.

The systematic uncertainties are provided in the form of up and down variations on the corrections for each source of system uncertainty. The up variation refers to the $+1\sigma$ upper bound on the correction while the down variation refers to the -1σ lower bound on the correction. Practically speaking these up and down variations will be used to create two additional signal models corresponding to the variation of these systematic uncertainties. A morphing is done between these three models

126

(nominal, up and down) so that a nuisance parameter under a Gaussian constraint can be fit for along with the Higgs parameters. This procedure is discussed at greater length in Section 7.8.

For muons, the systematic sources of uncertainty are the momentum scale correction, the Inner Detector (ID) resolution and the Muon Spectrometer (MS) resolution. To determine the effect of these systematic sources of error on the muon momentum response functions, the muon response functions are recalculated with the momentum corrections varied up and down by the systematic uncertainty. Thus, for the three muon momentum systematics, there will be seven sets of response functions:

1. **Nominal**: muon response functions with the default MCP corrections (the response functions already presented)

2. **Scale up**: muon response functions with the systematic scale correction varied up.

3. **Scale down**: muon response functions with the systematic scale correction varied down.

4. **ID up**: muon response functions with the systematic ID resolution correction varied up.

5. **ID down**: muon response functions with the systematic ID resolution correction varied down.

6. **MS up**: muon response functions with the systematic MS resolution correction varied up.

7. **MS down**: muon response functions with the systematic MS resolution correction varied down.

To consider the effect of these systematic uncertainties, the response functions from each method are used to generate mass responses which are then used, as discussed in the validation section above, to create a signal model. The result is compared to both the nominal model and the reconstructed mass. In Figure 7.7, the reconstruction level
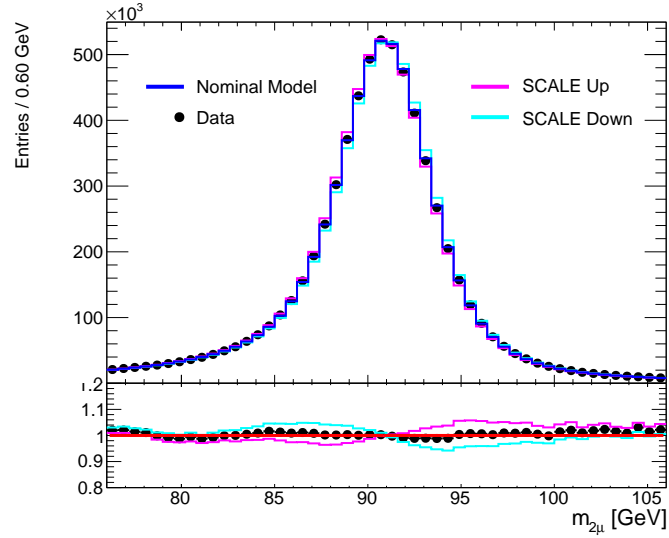
Figure 7.7: Truth $m_{2\mu}$ distribution convolved with the per-event Z mass response for nominal (blue), scale up (aqua), and scale down (violet) muon response functions and compared to 8 TeV $Z \rightarrow \mu\mu$ data.

$m_{2\mu}$ distribution is compared to the nominal model and the models with scale up and scale down resolution functions. This systematic error band largely encompasses the discrepancy between the reconstructed $m_{2\mu}$ in data and the model.

The other two systematic uncertainties, ID and MS resolution, are shown in Figure 7.8 and Figure 7.9, these systematics have negligible effect and can be ignored in the context of the muon response functions.
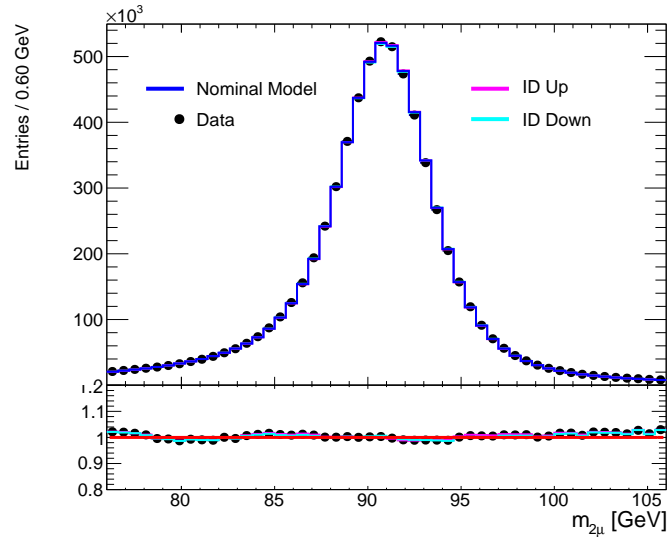
Figure 7.8: Truth $m_{2\mu}$ distribution convolved with the per-event Z mass response for nominal (blue), ID up (aqua), and ID down (violet) muon response functions and compared to 8 TeV $Z \rightarrow \mu\mu$ data.
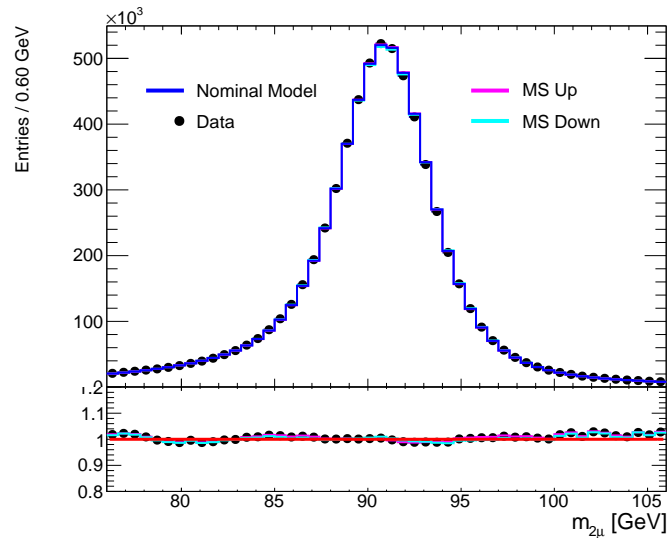
Figure 7.9: Truth $m_{2\mu}$ distribution convolved with the per-event Z mass response for nominal (blue), MS up (aqua), and MS down (violet) muon response functions and compared to 8 TeV $Z \rightarrow \mu\mu$ data.

7.2.2   Electron Response Functions

The electron energy is measured using the energy deposition in the electromagnetic calorimeter. This energy measurement is combined with an inner detector track to improve the energy resolution. This is known as the *E-p* combination. As with the muons, the electron detector response is estimated using electrons from MC and considering the weighted electron energy response given by Equation 7.11:

$$x_e = \frac{E_e^{reco} - E_e^{true}}{E_e^{reco}} \tag{7.11}$$

The distribution has a core which is described by the primary Gaussian and a large tail which is caused by the radiative energy loss of the electrons. This tail is best reproduced by an additional two Gaussians. This full three-Gaussian sum is fit to the MC simulated data which has all the relevant corrections applied. An example fit using this 3-Gaussian sum is shown in Figure 7.10. The computation and validation of these electron response functions was done by Graham Cree in conjunction with others from Carleton University and the Max-Planck Institute in Munich. The electron response model is validated in a similar manner to the muon response function.
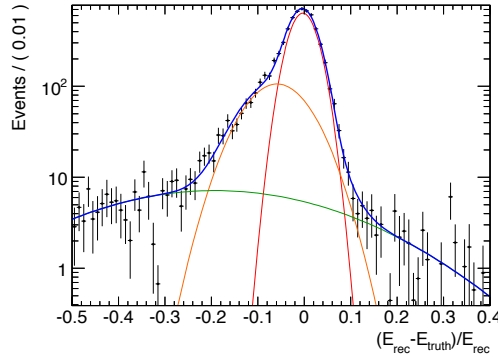
Figure 7.10: Example of the distribution of the fractional deviation of the reconstructed electron energy from the true energy. The data points are fitted with a sum of three normal distribution with the first Gaussian function constrained to describe the peak region and the second and third Gaussian functions to model the tail to negative values. Plot made by Graham Cree.

7.3 Signal Mass Model

The signal mass model starts by taking the truth distribution of the particle's invariant mass. The decay of any unstable particle will occur with a Breit-Wigner invariant mass distribution. This distribution is given by the following equation:

$$\text{Breit-Wigner}\,(m) = \frac{k}{\left(m^2 - M^2\right)^2 + M^2\Gamma^2} \tag{7.12}$$

Where M is the mass of the resonance, Γ is the decay width, and k is a normalization constant which depends on both the mass and width of the resonance. In Figure 7.11, a comparison between the MC truth at generator level, the notation for which is $m_{4l}^{true,born}$, and the resonance Breit-Wigner is shown. The MC events used are those which have passed the reconstruction level analysis selections detailed in Chapter 6.
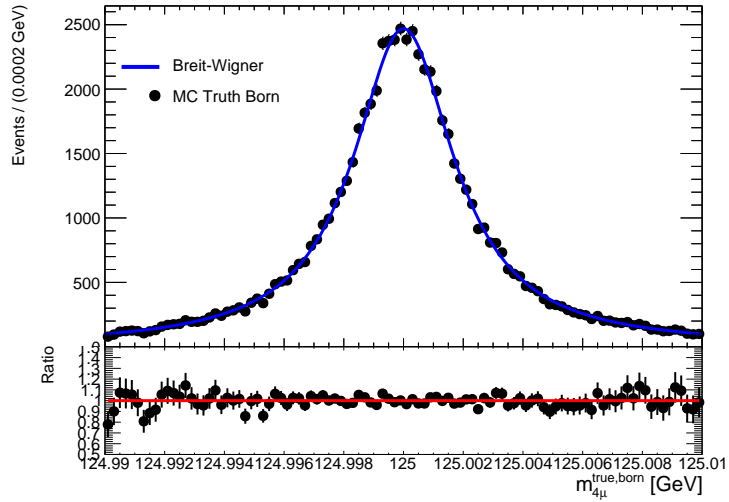
Figure 7.11: Truth $m_{4\mu}$ distribution at generator level from 125 GeV Higgs MC is compared to a Breit-Wigner with a mass of 125 GeV and a width of 4.083 MeV.

7.3.1 Acceptance Effects

For a very narrow resonance it is unlikely that the analysis selections will shape the truth-level invariant mass distribution because each event will have a true mass very close to the mass of the resonance. For a wider resonance, however, the truth distribution will likely be shaped by the analysis selections. In the case of the Higgs analysis, events on the left tail of the Breit-Wigner will be more likely to fail the p_{T} and invariant mass cuts while those on the right tail are more likely to pass these selections. Such effects are clearly visible in Figure 7.12 which compares the invariant mass distribution for events from from Higgs MC generated with a 3 GeV width that have passed the analysis selections to a Breit-Wigner with the same width. The ratio plot shows the truth level acceptance of the reconstruction level analysis selections.

By construction, the "acceptance ratio" corrects the Breit-Wigner so that it matches the truth lineshape in MC after reconstruction level analysis selections as
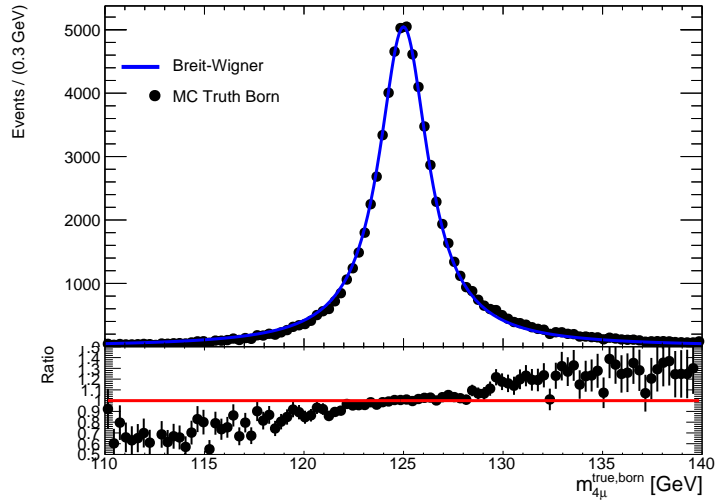
Figure 7.12: Truth $m_{4\mu}$ distribution at generator level from 125 GeV Higgs MC with a width of 3 GeV is compared to a Breit-Wigner with a mass of 125 GeV and a width of 3 GeV.

seen in Equation 7.13 where "Acc" stands for the acceptance ratio.

$$\mathrm{BW}^{corrected}\left(m_{4l}^{true,born}, \Gamma_H, m_H\right) = \mathrm{Acc}\left(m_{4l}^{true,born}\right)\cdot\mathrm{BW}\left(m_{4l}^{true,born}, \Gamma_H, m_H\right) \quad (7.13)$$

It remains to be seen, however, if the acceptance ratio is invariant for MC samples with different widths. Figure 7.13 shows the acceptance ratio for two MC samples with different width: $\Gamma_H = 3$ GeV and $\Gamma_H = 6$ GeV. A polynomial fit is performed on each acceptance ratio. Their compatibility indicates that the same acceptance ratio can be used to correct the Breit-Wigner for different values of Γ_H. The acceptance ratio used in the analysis is calculated by combining the 6 GeV and 3 GeV samples and using the increased statistics to fit a 2nd order polynomial. As expected, the acceptance ratio properly corrects the Breit-Wigner to agree with the truth invariant mass distribution after analysis selections as seen in Figure 7.14.
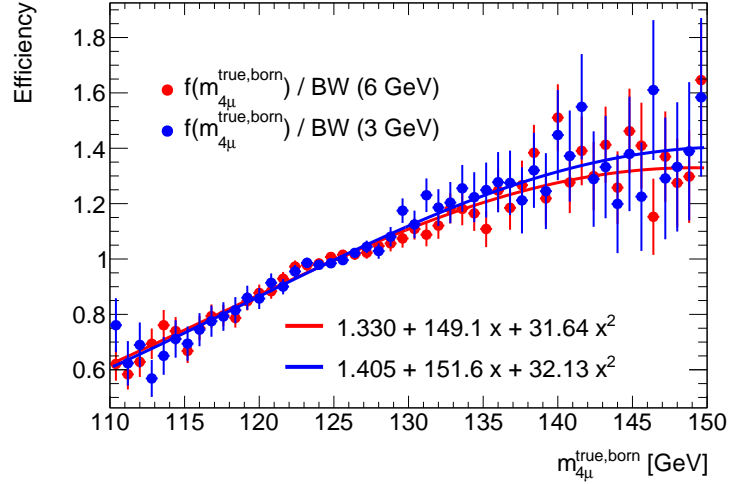
Figure 7.13: Truth $m_{4\mu}$ at generator level divided by the Breit-Wigner for 125 GeV Higgs MC with 3 and 6 GeV widths. The colored lines represent 2nd order polynomial fits.
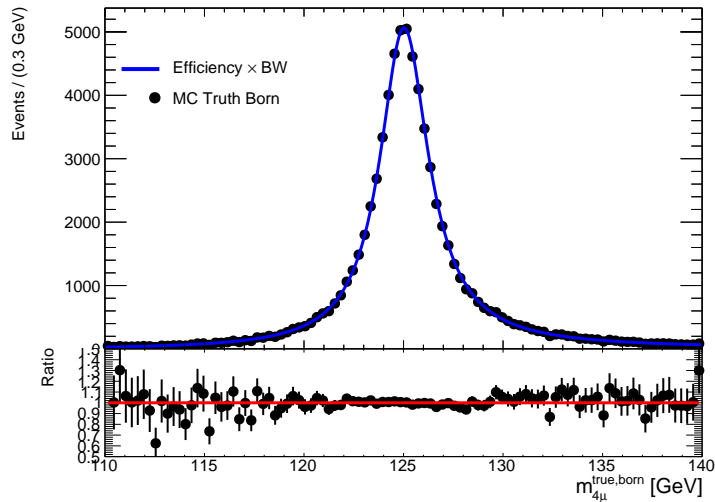
Figure 7.14: Truth m_{4e} at generator level from 125 GeV Higgs MC with a width of 3 GeV is compared to Acceptance $\times$ Breit-Wigner with a mass of 125 GeV and a width of 3 GeV.

7.3.2 Final State Radiation

Even if the muons were perfectly measured, their four-momenta would not sum together to get an invariant mass distribution as seen in Figure 7.11 due to final state radiation. This FSR will add a "tail" to the left side of the invariant mass distribution[1]. This truth invariant mass distribution, after subtracting final state radiation will be called the "bare" truth mass, $m_{4l}^{true,bare}$. The bare truth distribution from 125 GeV Higgs MC that passes the analysis selections can be seen in Figure 7.15. Using these two quantities: $m_{4l}^{true,born}$ (seen in Figure 7.11) and $m_{4l}^{true,bare}$ (seen in Figure 7.15), it is possible to describe the radiative tail in a coherent way:

$$\text{Tail} = m_{4l}^{true,bare} - m_{4l}^{true,born} \tag{7.14}$$

In Figure 7.16, the tail distribution is shown for different MC samples with different Higgs masses and widths. The tail distributions are similar thereby indicating that the same tail distribution can be used to correct the Breit-Wigner distribution regardless of mass or width. Rearranging Equation 7.14, the bare mass is simply:

$$m_{4l}^{true,bare} = \text{Tail} + m_{4l}^{true,born} \tag{7.15}$$

Because the $m_{4l}^{true,born}$ distribution is simply the modified Breit-Wigner (Acceptance × Breit-Wigner), the bare truth PDF can be written as the convolution:

$$PDF_{bare,true} = \text{Tail} \otimes (\text{Acc} \cdot BW) \tag{7.16}$$

---

[1]The electron response functions are computed using the born (pre-FSR) energy. This is because collinear FSR is oftentimes measured in the electron's calorimeter energy cluster and so the electron response cannot be factorized from the FSR like the muon response can.
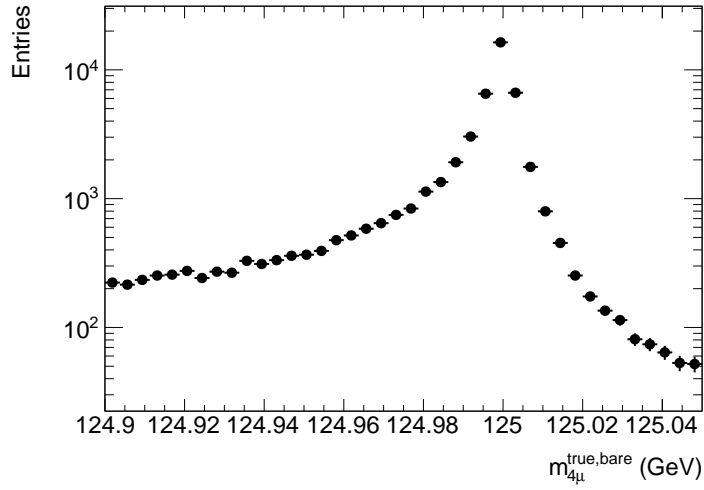
Figure 7.15: Bare truth distribution $m_{4\mu}$ from 125 GeV Higgs MC. An asymmetrical FSR tail is seen on the left-hand side of the distribution.
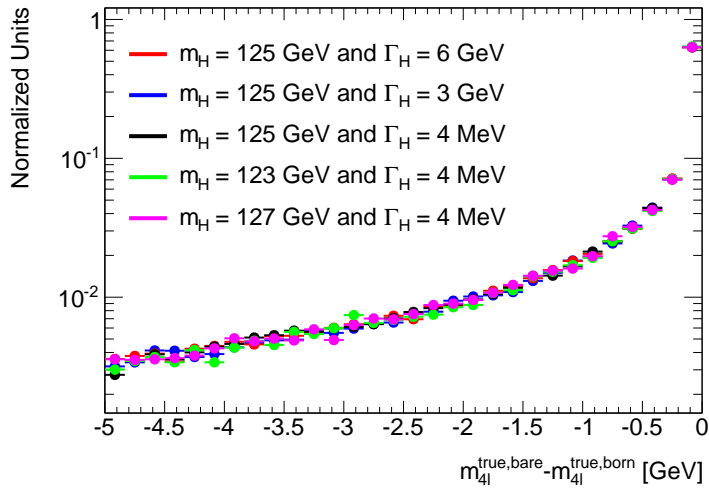
Figure 7.16: Radiative tail for Higgs MC samples with different widths and masses in the 4μ channel.

The convolution can be written explicitly as the following integral:

$$\int_{-\infty}^{\infty} \text{Tail}\left(m_{4l}^{true,bare} - m_{4l}^{true,born}\right) \text{Acc}\left(m_{4l}^{true,born}\right) \text{BW}\left(m_{4l}^{true,born}, \Gamma_H, m_H\right) dm_{4l}^{true,born}$$

$$(7.17)$$

Using this procedure, it is possible to compare the bare truth distribution from MC to the bare truth PDF constructed in this way. This comparison between the PDF and Higgs MC is seen in Figure 7.17 for Higgs MC samples ($m_H = 125$ GeV) with widths of 3 GeV and 6 GeV. As discussed in Section 6.4.5, there is an attempt to add reconstructed FSR candidates back into an event. To account for this using the tail distribution, the difference between the reconstructed invariant mass (denoted m_{4l}^{reco}) and the invariant mass after the FSR candidate (denoted $m_{4l}^{reco,w/fsr}$) is added to the FSR tail histogram. This leads to a redefinition of the tail as:

$$\text{Tail} = m_{4l}^{true,bare} - m_{4l}^{true,born} + m_{4l}^{reco,w/fsr} - m_{4l}^{reco} \qquad (7.18)$$

This tail distribution with the FSR candidates added, calculated using the 8 TeV Higgs MC sample with $m_H = 125$ GeV after analysis selections, is shown for the 4μ channel in Figure 7.18. This leads to a tail distribution that is no longer zero at all values greater than zero. This is due to instances when fake or mismeasured FSR candidates are added back into the event. Using this new tail histogram in the convolution gives good agreement between reconstructed $m_{4\mu}$ after the FSR corrections and the signal model. The tail shown in Figure 7.18 is for the 4μ channel. As mentioned earlier, electron response functions are calculated with respect to the *born* truth quantities. Accordingly, the value used to fill the tail histogram for channels
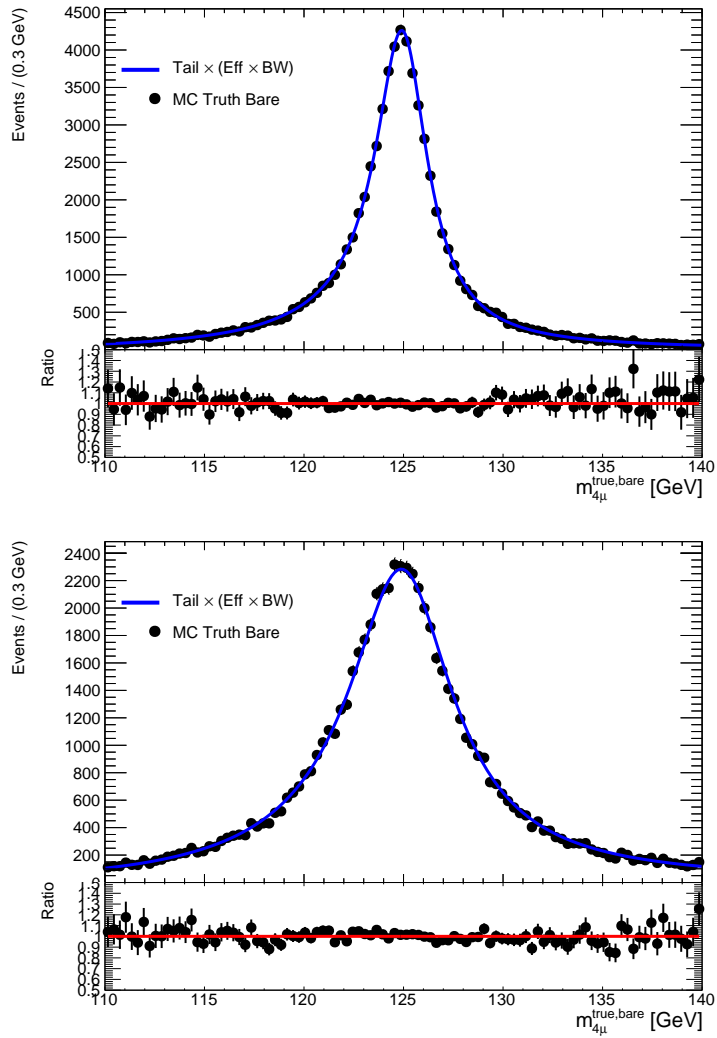
Figure 7.17: Bare truth $m_{4\mu}$ distributions from Higgs MC (with $m_H = 125$ GeV compared the the bare truth PDF. MC with 3 GeV width is top, MC with 6 GeV width is bottom.
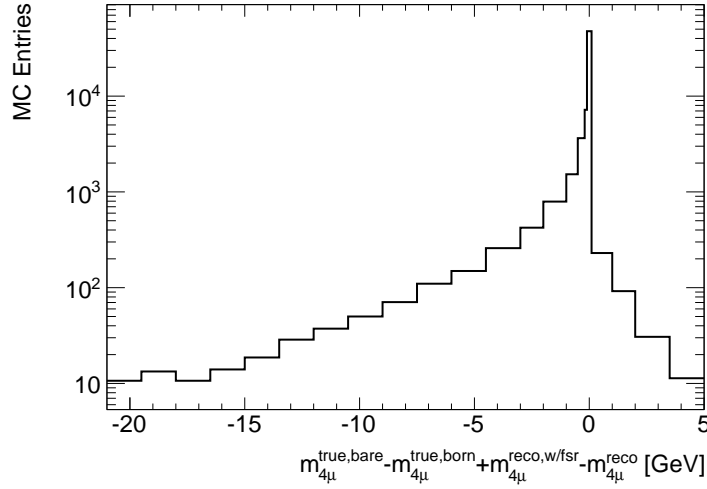
Figure 7.18: Radiative tail histogram for the 4μ-channel which includes the reconstruction level FSR correction detailed in Section 6.4.5. The histogram is obtained using 125 GeV Higgs MC that has passed all analysis selection.

involving electrons is given by:

$$
\text{Tail} = \sqrt{\left(\sum_{i}^{\#\text{muons}} p_i^{true,bare} + \sum_{j}^{\#\text{electrons}} p_j^{true,born}\right)^2} - m_{4l}^{true,born} + m_{4l}^{reco,w/fsr} - m_{4l}^{reco}
\tag{7.19}
$$

This reduces to $\text{Tail} = m_{4l}^{reco,w/fsr} - m_{4l}^{reco}$ in the $4e$-channel and $\text{Tail} = m_{4l}^{true,bare} - m_{4l}^{true,born} + m_{4l}^{reco,w/fsr} - m_{4l}^{reco}$ in the 4μ channel.

7.3.3 Detector Response

Having developed an expression for the truth distribution, it is now possible to integrate the detector response together with the truth distribution. As discussed in Section 7.2.1, the mass response function is a parameterization of the following distribution:

$$
x_{m_{4l}} = \frac{m_{4l}^{reco} - m_{4l}^{true,bare}}{m_{4l}^{true,bare}}
\tag{7.20}
$$

139

Furthermore, Equation 7.9 shows how the mass response can be written in terms of individual lepton response functions. Equation 7.20 can be rearranged to give:

$$m_{4l}^{reco} = m_{4l}^{true,bare} + m_{4l}^{true,bare} x_{m_{4l}} \tag{7.21}$$

This indicates that the PDF of the reconstruction level invariant mass at reconstruction level is the convolution of the mass response function with the invariant mass distribution at truth level as discussed in the previous two sections. This convolutions means that the full signal PDF can be written as the following convolution:

$$\text{PDF}_{signal} = \text{Response} \otimes [\text{Tail} \otimes (\text{Acceptance} \cdot \text{Breit-Wigner})] \tag{7.22}$$

7.3.4   Numerical Convolutions

Practically this convolution (Equation 7.22) would be very slow if done numerically. To speed it up, the commutative property of convolution is used to rearrange the convolutions:

$$PDF_{signal} = \text{Tail} \otimes [\text{Response} \otimes (\text{Acceptance} \cdot \text{Breit-Wigner})] \tag{7.23}$$

With this ordering, the convolution can be sped up by taking advantage of the fact that both the gaussian and the Breit-Wigner distributions fall off far from the peak. Normally the Gaussian with Breit-Wigner convolution is given by:

$$\int_{-\infty}^{\infty} \text{Gaus}(\tau, \mu, \sigma) \, \text{Acc}(x - \tau) \, \text{BW}(x - \tau, m_H, \Gamma) \, d\tau \tag{7.24}$$

Since 99.99% of the Gaussian distribution is located between the -4σ to $+4\sigma$ mark, this range is used for the integration in most regions. The integral is evaluated numerically and thus the infinitesimal $d\tau$ goes to $\Delta\tau$. This $\Delta\tau$ step size is chosen

to be whichever of the following values is smaller: 1) the width of the Breit-Wigner divided by two $\Gamma/2$ or 2) the width of the Gaussian divided by two $\sigma/2$. Using these values to perform the numerical convolution transforms Equation 7.24 into Equation 7.25

$$\sum_{i=0}^{8\sigma/\Delta\tau} \mathrm{Gaus}\,(\tau_i, \mu, \sigma)\,\mathrm{Acc}\,(x - \tau_i)\,\mathrm{BW}\,(x - \tau_i, m_H, \Gamma)\,\Delta\tau \qquad (7.25)$$

Where $\Delta\tau = \mathrm{Min}\,(\Gamma/2, \sigma/2)$ and $\tau_i = \mu - 4\sigma + i\Delta\tau$. There is one region, however, where this is not practical. This is when Γ is much much smaller than σ. In this case, the integration is done around the Breit-Wigner instead of around the Gaussian. For this region, the numerical integration is given by the following:

$$\sum_{i=0}^{8\Gamma/\Delta\tau} \mathrm{Gaus}\,(x - \tau_i, \mu, \sigma)\,\mathrm{Acc}\,(\tau_i)\,\mathrm{BW}\,(\tau_i, m_H, \Gamma)\,\Delta\tau \qquad (7.26)$$

Where $\Delta\tau = \Gamma/2$ and $\tau_i = m_H - 4\Gamma + i\Delta\tau$. After performing the Gaussian Breit-Wigner numerical convolution, it is now necessary to do the FSR tail convolution.

This is done numerically using a pre-calculated histogram that defines the tail with fairly coarse binning (Seen previously in Figure 7.18). Such binning is justified because the typical width of the Breit-Wigner convolved with the response Gaussian is quite wide. The equation which describes the next numerical integration is seen in Equation 7.27.

$$\sum_{i} \mathrm{Tail}\,(\tau_i)\,[Gaus \otimes (\mathrm{Acc} \cdot \mathrm{BW})]\,(x - \tau_i)\,\Delta\tau_i \qquad (7.27)$$

Where τ_i is the center of the ith bin in the FSR tail histogram and $\Delta\tau_i$ is the width of the ith bin. This is sufficiently fast to allow fitting on high statistics MC samples. Using this numerical convolution together with the the 16-Gaussian sum, it is now
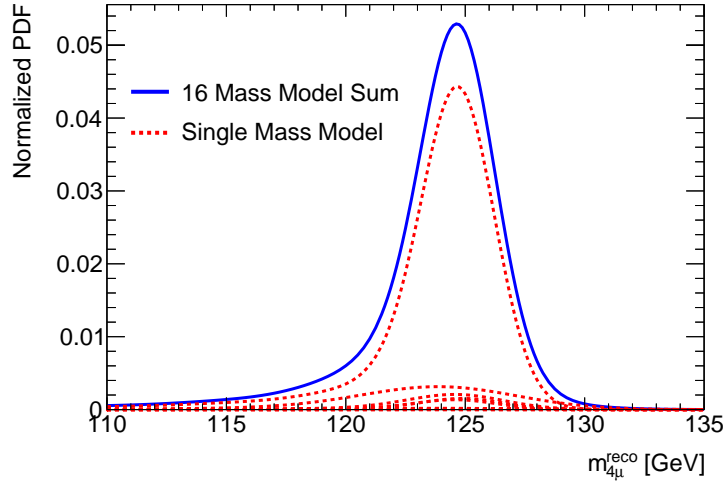
Figure 7.19: Signal PDF for an event in 125 GeV Higgs MC with nominal width.

possible to construct a full signal model. Figure 7.19 shows such a signal PDF for a single event from 125 Higgs MC.

To fully validate the signal model using MC, the full model is made for each event (as in Figure 7.19) and then summed up for every event in MC. This summation is then compared to the reconstructed level m_{4l} from various Higgs MC samples with different widths.

Figures 7.20, 7.21, and 7.22 show that there is good agreement between reconstructed m_{4l} and the model. This agreement indicates that the model is working properly for the signal and can be used in a combined fit.
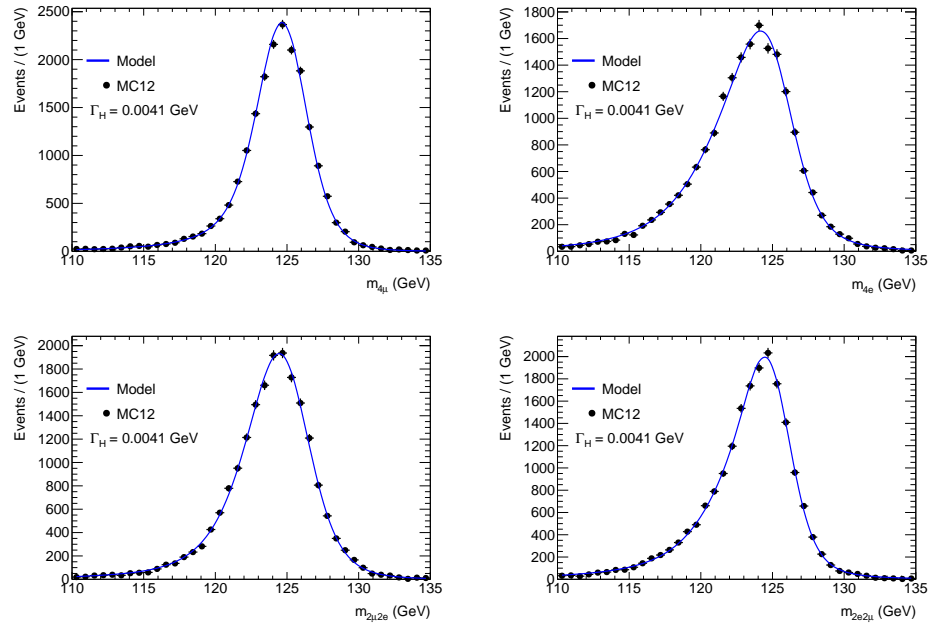
Figure 7.20: Model vs. reco m_{4l} for Higgs MC with 125 GeV mass and nominal (4.1 MeV) width. Top left is for 4μ, top right is for $4e$, bottom left is for $2\mu2e$, and bottom right is for $2e2\mu$.
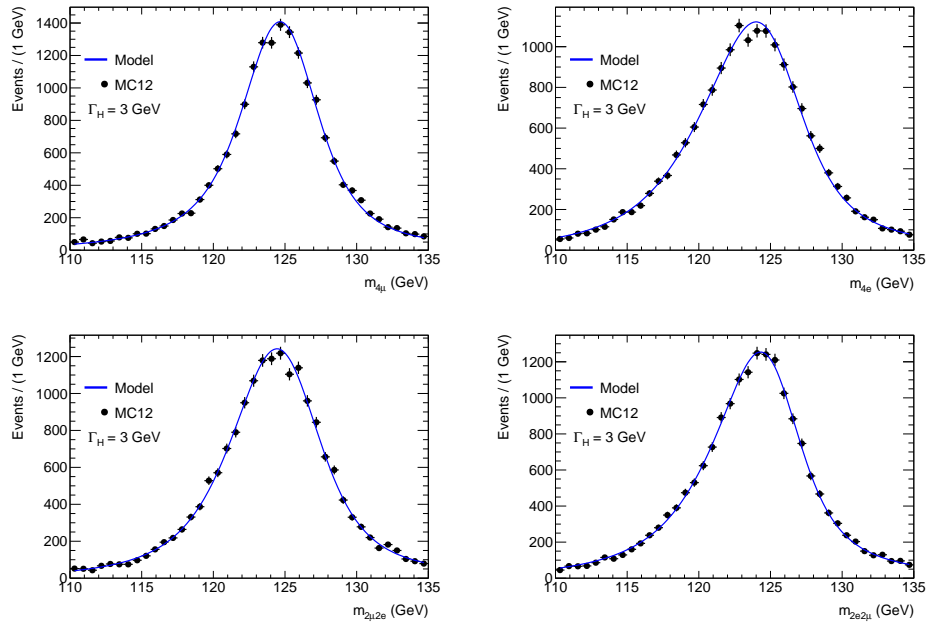
Figure 7.21: Model vs. reco m_{4l} for Higgs MC with 125 GeV mass and 3 GeV width. Top left is for 4μ, top right is for $4e$, bottom left is for $2\mu2e$, and bottom right is for $2e2\mu$.
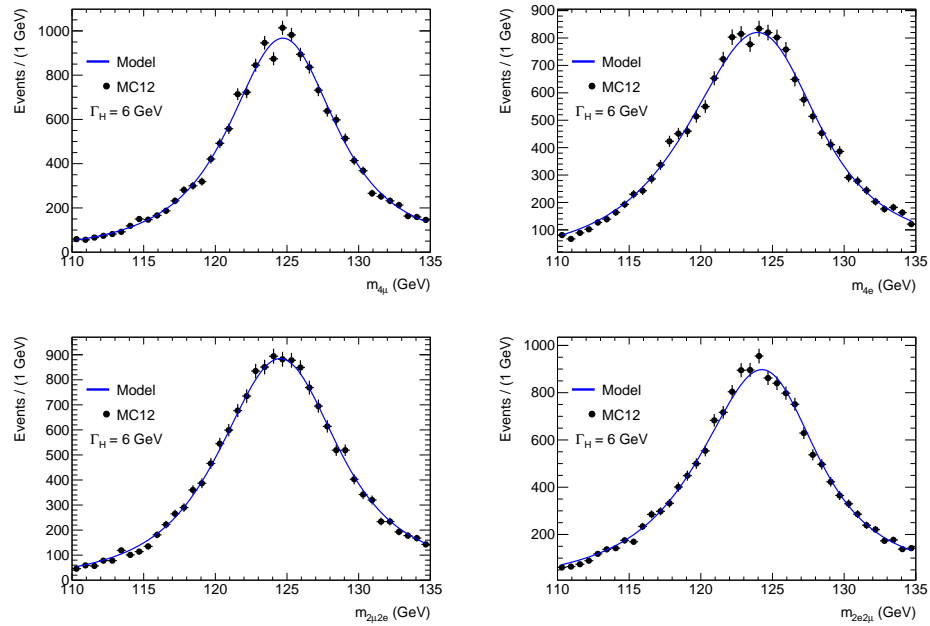
Figure 7.22: Model vs. reco m_{4l} for Higgs MC with 125 GeV mass and 6 GeV width. Top left is for 4μ, top right is for $4e$, bottom left is for $2\mu2e$, and bottom right is for $2e2\mu$.

7.3.5   Signal Mass Model Validations

One strength of the event-by-event approach to fitting the mass and width of the Higgs boson is that this same approach can be used (with the same response functions) on additional physics processes. This makes it possible to understand whether the response functions derived using muons from one resonance can be applied to others. Furthermore, additional resonances with higher statistics in data than the $H \rightarrow ZZ^{(*)} \rightarrow 4l$ can be used to ensure the validity of the general method. Two physics processes that can be used are the $Z \rightarrow \mu\mu$ and the $Z \rightarrow 4\mu$. The Feynman diagrams for these processes are shown in Figure 7.23 and Figure 7.24 respectively. The $Z \rightarrow \mu\mu$ is particularly useful because there are a large number of candidate events that can be used to ensure the signal model will reproduce the shape in both data and MC simulated events. The $Z \rightarrow 4\mu$ has the same final state as the Higgs signal which makes it an excellent resonance for checking the machinery of the signal model.

As with the $H \rightarrow ZZ^{(*)} \rightarrow 4\ell$ model, the FSR tail is calculated from MC while a Breit-Wigner with width set to the known width of the Z resonance is used as the born truth shape. Acceptance ratios are calculated from MC. For the $Z \rightarrow \mu\mu$ resonance, no fit for the Z mass or width is performed. Instead, a simple comparison is done between the signal model and the reconstruction level $m_{2\mu}$ using the known
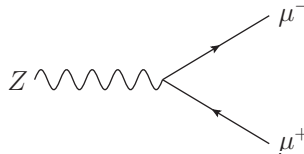
Figure 7.23: A Feynman diagram showing the lowest order decay of a Z-boson to two muons.
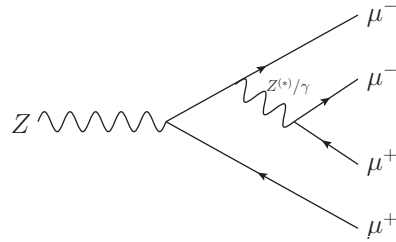
Figure 7.24: A Feynman diagram showing the lowest order decay of a Z-boson to four muons.

values of the mass and width of the Z-boson as the parameters for the signal model.

Figure 7.25 shows the comparison between the signal model and the $m_{2\mu}$ in data and

MC for the $Z \to \mu\mu$ resonance. The data used for these plots is a subset of data from

the 2012 data-taking. The data and MC are selected by requiring a single same-flavor,

opposite-sign dilepton pair. The muons themselves are required to pass the muons

preselection requirements of the Higgs analysis described in Section 6.4.1.
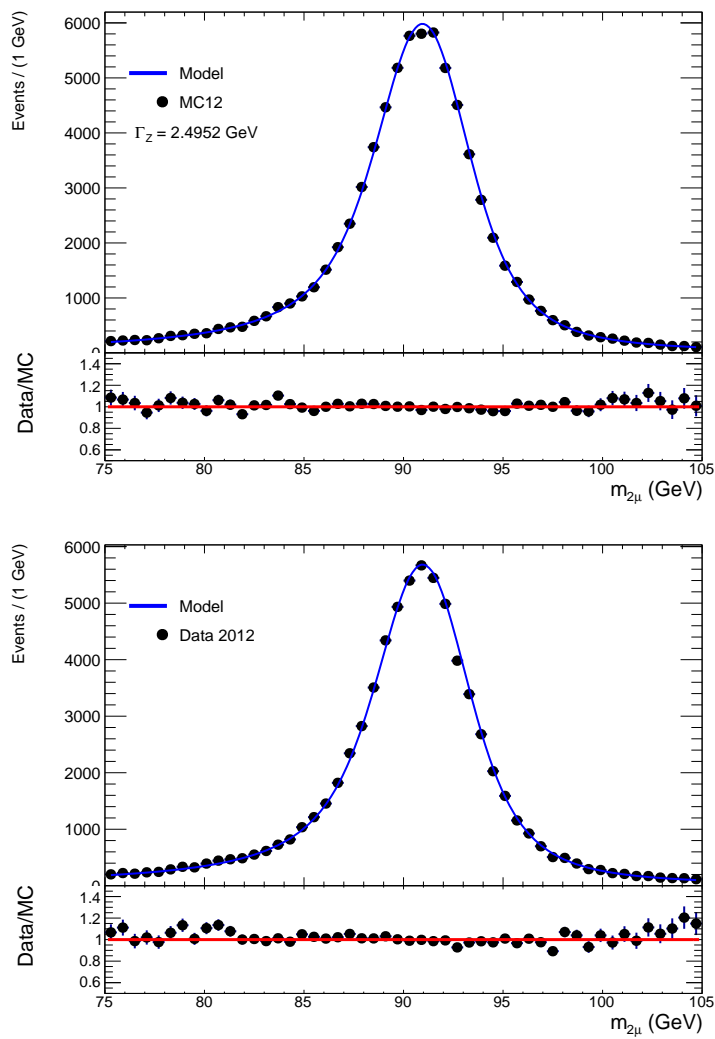
Figure 7.25: Signal model compared with 8 TeV $Z \rightarrow \mu\mu$ MC (above) and data (below).

In the case of $Z \to 4\mu$, relaxed selections from the Higgs analysis are used. The muon preselection p_T-cut is reduced to 4 GeV for CB, ST, and SA muons. Furthermore, the lepton-p_T cuts are reduced to $p_{T,1} > 20$ GeV, $p_{T,2} > 15$ GeV, and $p_{T,3} > 10$ GeV for electrons or $p_{T,3} > 8$ GeV for muons. The invariant mass cuts on both dilepton pairs are relaxed: $m_{12} > 20$ GeV and $m_{34} > 5$ GeV. To ensure that the signal model for the $Z \to 4\mu$ is working properly a comparison is made between the model and the MC where the mass and width of the Breit-Wigner are set to their known values of 91.1876 GeV and 2.4952 GeV respectively [9]. The fit to data is shown in Figure 7.26. The fitted m_Z using 8 TeV data is found to be 90.9 ± 0.3 GeV and the width is found to be 3.07 ± 0.65 GeV. The uncertainties are purely statistical and the model used includes no background contributions. A full and more complete analysis of the $Z \to 4\ell$ resonance is detailed in [49].
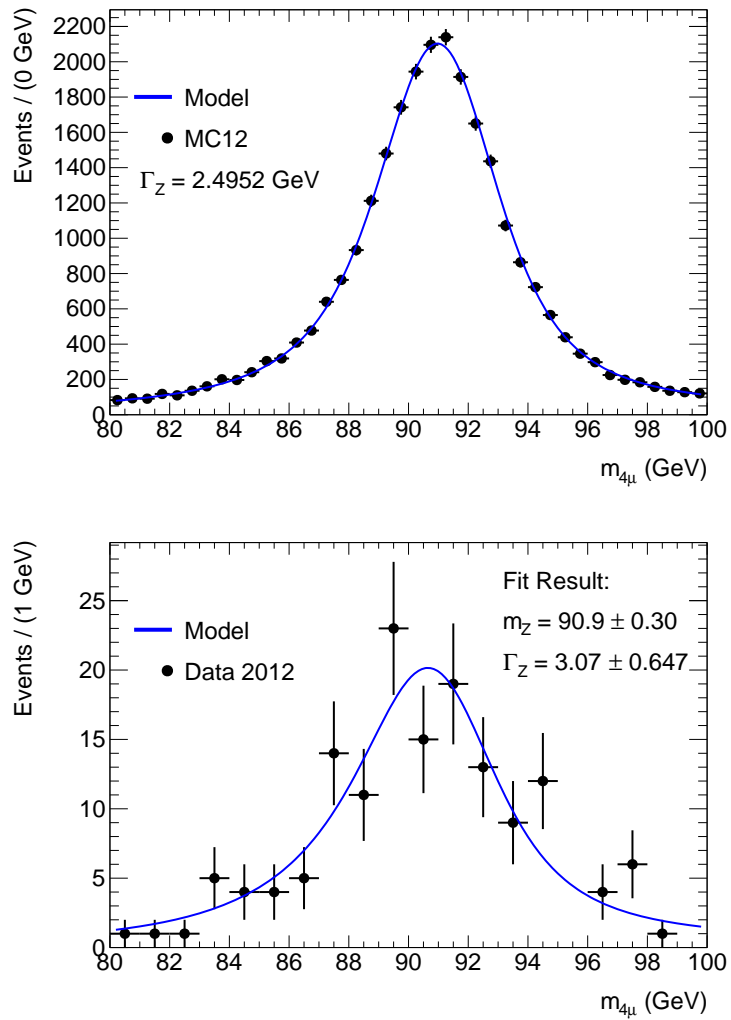
Figure 7.26: Signal model compared with 8 TeV $Z \to 4\mu$ MC (above) and the signal model fit to ATLAS data (below) with the fitted mass and width displayed.

7.4   Signal BDT Model

Although the shape of the signal has been modeled in the invariant mass dimension, it is also necessary to parameterize the shape of the signal for different values of the BDT discussed more fully in Section 6.4.7. Like the m_{4l} shape, the BDT shape will depend on the Higgs parameters. The dependence on the Higgs mass, m_H, is seen in Figure 7.4. The dependence on the Higgs width can be neglected so the BDT observable is only parameterized with respect to the m_H. To produce a smooth PDF which can be evaluated at any value of the parameter, m_H, the kernel based smoothing discussed in Section 7.7 is used.
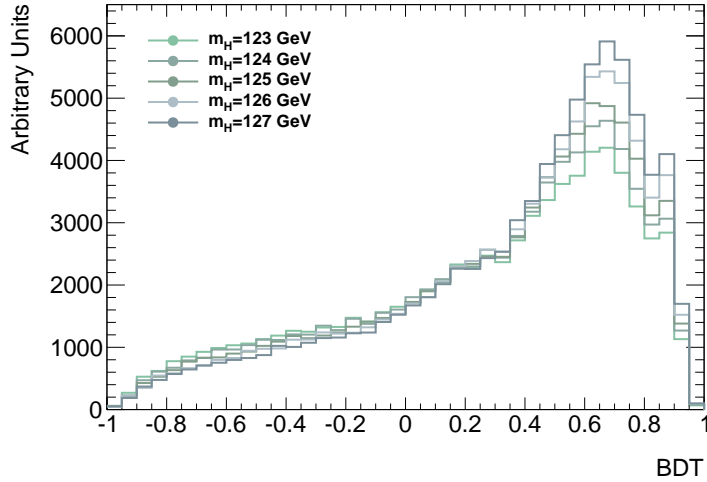
Figure 7.27: Comparison of BDT shapes for signal samples of different m_H using 8 TeV MC.

7.5 Background Models

The irreducible background to the Higgs signal in the $H \rightarrow ZZ^{(*)} \rightarrow 4\ell$ analysis is the Standard Model ZZ^* production. The primary production modes are $q\bar{q} \rightarrow ZZ$ and $gg \rightarrow ZZ$. MC simulated events are used to determine the shape of the ZZ background. A Kernel Density Estimate (KDE) smoothing is performed to ensure a continuous PDF in the m_{4l} and BDT dimensions. The KDE smoothing is discussed in Section 7.7.

7.6 Reducible Background Model

The reducible backgrounds for the Higgs analysis are generally produced by the Z+jets, $t\bar{t}$, and WZ physical processes. The data driven techniques used to estimate the reducible backgrounds are discussed in Section 6.4.4. The shape of the background

is smoothed in two dimensions, m_{4l} and BDT, using the kernel density estimate technique that is discussed in Section 7.7. The 2D shape of the backgrounds in BDT and m_{4l} after smoothing are compared to data and shown in Figure 6.5.

7.7   Smoothing with Kernel Estimation Techniques

Although the signal model in invariant mass is calculated using event-by-event information, reconstruction level MC simulated data and data-driven techniques are used to understand the shape of the backgrounds in the invariant mass dimension and the shape of both signal and background in the BDT dimension. Smoothing techniques are used to transform these shapes into continuous smoothed PDFs. A particularly powerful method uses kernel estimation techniques which attempt to find an underlying parent distribution which is relatively smooth and statistically consistent with the data sample used to generate this parent distribution. Practically this is done by summing Gaussian kernels. In one dimension, the parent distribution is given by:

$$f_0(x) = \frac{1}{nh} \sum_{i=1}^{n} K\left(\frac{x - t_i}{h}\right) \tag{7.28}$$

where n is the number of data points, t_i represents the position of the ith data point and h is the smoothing parameter. K is a Gaussian kernel with a mean of 0 and a width of 1.

$$K(x) = \frac{1}{\sqrt{2\pi}} e^{-x^2/2} \tag{7.29}$$

The h can be varied based on the statistics of the sample. Additionally this procedure can be extended to 2-dimensions. In practice, this procedure is performed using the

Root library known as *RooKeysPdf* [50].

7.8 Systematic Uncertainties on the Mass Measurement

The systematic uncertainties on both signal and background models are treated as nuisance parameters. Nuisance parameters are those which are not of primary interest but which must be included in a fit to account for some uncertainty about the shape of the PDF. A classic example of a nuisance parameter is when fitting Gaussian-distributed data to find the mean of the distribution. In this case, the width, σ, of the data is unimportant but it must be fitted along with the mean when using a Gaussian PDF to fit.

A nuisance parameter, α, is used for each source of systematic uncertainty. For each systematic, three signal and background PDFs are computed: the nominal model, the model with the systematic varied up by one sigma, and the model with the systematic varied down by one sigma. A linear morphing between these three models is then performed. The nuisance parameter is used to vary the degree of morphing (when the parameter, α, is set to zero, the nominal model is used while $\alpha = \pm 1$ refer to the $\pm 1\sigma$ models). Due to the linear morphing, the nuisance parameter can take on any value including those outside of the $\pm 1\sigma$ models used to construct the morphing. However, to ensure that the nuisance parameter will not move substantially away from the central value, a Gaussian penalty function is added to the likelihood to constrain the nuisance parameter.

The sources of systematic uncertainty detailed in the following section can be split into two types: efficiency and shape. Those associated with efficiency are the identification, reconstruction, and trigger efficiency of various particles used in the analysis. These systematics will affect the normalization of various components of the signal and background. Additionally there are systematics which affect the shape of the signal and background models. These systematics are related to the scale and resolution of the energy and momentum of the particles.

At the analysis level, the systematics are evaluated by comparing the event yield with the nominal values of the systematics to the event yield with the systematic varied $+1\sigma$ and -1σ. The percent change is then evaluated by considering the value of $|(N - N')/N|$ where N is the nominal event yield and N' is the event yield after the systematic variation.

Leptons are treated as correlated so if a systematic uncertainty is applied to one of the leptons, it is applied to all. The weights corresponding to efficiency are varied up and down in unison; if the weight of an event is given by $w_1 \cdot w_2 \cdot w_3 \cdot w_4$, then the overall weight with the weights of each lepton varied up is given by $(w_1 + \delta w_1) \cdot (w_2 + \delta w_2) \cdot (w_3 + \delta w_3) \cdot (w_4 + \delta w_4)$. This change in weights will be reflected in the overall event yield. To understand the systematic uncertainty on the energy and momentum scale (for electrons and muons respectively), the value of the energy/momentum is shifted by the scale systematic variation before event selections and then the effect of this is seen on event yields. Using the change in event yields, it is possible to understand which systematics are relevant to the measurement.

7.8.1 Electron Reconstruction and Identification

The uncertainties on the electron reconstruction and identification efficiency are separated into those which are uncorrelated and correlated [51]. The uncorrelated uncertainties are those related to the statistical uncertainty which is unrelated for the different E_{T} bins. These bins are $7 < E_{\mathrm{T}} < 10$ GeV, $10 < E_{\mathrm{T}} < 15$ GeV, $15 < E_{\mathrm{T}} < 20$ GeV, and $E_{\mathrm{T}} > 20$ GeV; the three nuisance parameters corresponding to the statistical part of the uncertainty for the first three bins are called EL_2012_ST_7, EL_2012_ST_10, and EL_2012_ST_15. The final bin is $E_{\mathrm{T}} > 20$ GeV and has a single nuisance parameter, EL_2012_IDST_high, that incorporates the correlated part of the identification efficiency uncertainty and the uncorrelated part of the identification and reconstruction efficiency uncertainty (i.e. the statistical component). The correlated part of the identification efficiency uncertainty for the $E_{\mathrm{T}} < 20$ GeV bins is encapsulated by a single nuisance parameter, EL_2012_ID_low. The reconstruction efficiency is split into two nuisance parameters for $E_{\mathrm{T}} < 15$ GeV and $E_{\mathrm{T}} > 15$ GeV. These are EL_2012_REC_Low and EL_2012_REC_high respectively.

An additional uncertainty is based on the data-MC comparison in tag-and-probe studies (detailed in [52]). This uncertainty, called H4l_EL_EFF_ISOIP, relates to the uncertainty on the isolation and impact parameter (IP) significance cut efficiency and is applied to electrons with an $E_{\mathrm{T}} < 15$ GeV. The impact of this uncertainty on the measurement varies from 0.7% to 2.5 % based on the region and E_{T}. The percentage effect of each systematic uncertainty on the signal yield ($|N - N'|/N$) is seen in Table 7.1.

Table 7.1: Systematic uncertainty on the signal yield, $|(N - N')/N|$, for signal Higgs MC with $m_H = 125$ GeV for the four final states. The meaning of the names of the nuisance parameters is discussed in the Section 7.8.1 for the electrons, Section 7.8.2 for the muons, and Section 7.8.3 for the trigger..

Nuisance parameter	$4e$	$2e2\mu$	$2\mu2e$	4μ
Electron reconstruction, identification and cut efficiencies				
EL_2012_ST_7	0.67%	0.02%	0.63%	-
EL_2012_ST_10	0.91%	0.08%	0.85%	-
EL_2012_ST_15	0.78%	0.14%	0.65%	-
EL_2012_ID_low	1.54%	0.23%	1.34%	-
EL_2012_IDST_high	2.64%	1.61%	1.04%	-
EL_2012_REC_low	2.63%	0.20%	2.45%	-
EL_2012_REC_high	0.94%	0.28%	0.65%	-
H4l_EL_EFF_ISOPID	1.18%	0.07%	1.10%	-
Muon reconstruction and identification efficiencies				
MU_EFF	-	1.09%	0.77%	1.86%
Trigger efficiencies				
EL_TRIG	0.21%	0.21%	0.05%	-
MU_TRIG	-	0.03%	0.58%	0.65%

7.8.2 Muon Reconstruction and Identification

The muon reconstruction and identification efficiency systematic uncertainty is parameterized by a single nuisance parameter (MU_EFF) [6]. The percent effect on the signal yield is seen in Table 7.1.

7.8.3 Trigger

Because the final state of the Higgs decay includes four leptons two of which tend to be at high-p_T/E_T, the trigger efficiency is very high. This is because the probability an event will not be reconstructed is only $(1-\epsilon_1)\cdot(1-\epsilon_2)\cdot(1-\epsilon_3)\cdot(1-\epsilon_4)$. The trigger efficiency is estimated at around 97% for the 4μ, $2e2\mu$, and $2\mu2e$ channels. While for the $4e$ channel, the efficiency is close to 100%. The trigger efficiency uncertainty

is determined by calculating the number of events that pass all the selection criteria with and without the trigger requirement. The nuisance parameter related to the electron trigger efficiency uncertainty is called EL_TRIG while the nuisance parameter corresponding to the muon trigger efficiency uncertainty is called MU_TRIG.

7.8.4 Lepton Energy Scale and Resolution

Rather than use the percent effect on the signal yield to gauge the effect of the energy scale and resolution systematics, the difference in reconstructed four-lepton invariant mass, m_{4l}, is calculated between the nominal value and the $+1\sigma$ (Up) and -1σ (Down) variations of the given systematic uncertainty. The change in the mean value of the reconstructed m_{4l} of the events, $\langle m_{4l}^{varied} \rangle - \langle m_{4l}^{nominal} \rangle$, is used to characterize the effect of the systematic on the ensemble of events.

7.8.5 Electron Energy Scale and Resolution

There are a large number of systematics which vary the scale of the electron and photon energy. A total of 24 separate nuisance parameters are used to vary both the electron and photon energy scale. An additional 5 nuisance parameters are dedicated to the photon energy scale in particular. These are needed due to the usage of FSR photons by the analysis. Lastly, a single nuisance parameter is used which varies the electron momentum scale and relates to the uncertainty on the ID track measurement. The majority of these systematics correspond to different regions and components of the electron reconstruction algorithms. The combined effect of these 24 systematics (labeled ZeeAll) on the average invariant mass of signal MC ($\langle m_{4l}^{varied} \rangle - \langle m_{4l}^{nominal} \rangle$)

Table 7.2: Difference of the mean reconstructed mass, $\langle m_{4l}^{varied}\rangle - \langle m_{4l}^{nominal}\rangle$, in MeV for nuisance parameters of electron energy scale and resolution and muon momentum scale and resolution using signal MC with a Higgs mass of 125 GeV (8 TeV). Up (Down) means a $+1\sigma$ (-1σ) variation.

Nuisance parameter	4e		2e2μ		2μ2e		4μ	
	Up	Down	Up	Down	Up	Down	Up	Down
Electron & photon energy scale								
ZeeAll	52	−53	34	−34	21	−18	-	-
Electron momentum scale								
Momentum	16	−16	3	−4	12	−11	-	-
Muon momentum scale								
SCALE	-	-	21	−25	32	−32	54	−55
Muon momentum resolution								
ID	-	-	−1	1	−2	2	0	0
MS	-	-	1	−1	−2	2	4	−4

is seen in Table 7.2. The effect of the photon energy scale is completely negligible and is ignored by the measurement.

7.8.6   Muon Momentum Scale and Resolution

As discussed in Chapter 5, muons are reconstructed by combining tracks in the ID and in the MS. There is a single scale correction for muons but the resolution corrections are separated into the ID and MS portions of the muon resolution. This gives a total of three nuisance parameters: one for the muon scale and two for the muon resolution. The effect of varying these nuisance parameters on the reconstructed m_{4l} is detailed in Table 7.2.

Table 7.3: Systematic uncertainty (normalization) for PDF+α_S and QCD scale uncertainties on the signal yield for each production mechanism at 125 GeV for 7 and 8 TeV.

Production mechanism	2011 (7 TeV)				2012 (8 TeV)			
	PDF+α_S		QCD scale		PDF+α_S		QCD scale	
	Up	Down	Up	Down	Up	Down	Up	Down
ggH	7.5%	6.9%	7.2%	7.8%	7.5%	6.9%	7.2%	7.8%
VBF	2.6%	2.8%	0.2%	0.2%	2.6%	2.8%	0.2%	0.2%
WH	2.3%	2.3%	1.0%	1.0%	2.3%	2.3%	1.0%	1.0%
ZH	2.5%	2.5%	3.1%	3.1%	2.5%	2.5%	3.1%	3.1%
ttH	8.1%	8.1%	3.8%	9.3%	8.1%	8.1%	3.8%	9.3%

7.8.7 Luminosity

The luminosity represents a normalization uncertainty for the measurement. This overall uncertainty is 1.8% for 7 TeV data and 2.8% for 8 TeV data.

7.8.8 Theory Uncertainties

The theoretical uncertainties in the branching ratio to Higgs decay and the PDF+α_s and QCD scale uncertainties are discussed in [1,2,46] and these theoretical calculations are used for the Higgs analyses by both ATLAS and CMS. The parton distribution function, PDF, details the momentum fraction carried by each parton in the proton. Additionally, the α_s parameter relates to the strong force coupling. The theoretical uncertainty on these parameters will affect the production rate and branching fractions at the LHC. For a Higgs with a mass of 125 GeV, these percent uncertainties are shown in Table 7.3.

As with the signal, PDF+α_s and QCD scale uncertainties affect the m_{4l} shape for the $qq \to ZZ$ and $gg \to ZZ$ processes. The overall normalization uncertainties are

Table 7.4: Systematic uncertainty (normalisation) for PDF+α_S and QCD scale for $qq \to ZZ$ and $gg \to ZZ$ backgrounds.

Background process	2011 (7 TeV)				2012 (8 TeV)			
	PDF+α_S		QCD scale		PDF+α_S		QCD scale	
	Up	Down	Up	Down	Up	Down	Up	Down
$qq' \to ZZ$	4 %	4 %	5 %	5 %	4 %	4 %	5 %	5 %
$gg \to ZZ$	8 %	8 %	37 %	25 %	10 %	10 %	31 %	22 %

shown in Table 7.4.

7.8.9   Ranking of Systematics

The 2D template approach which uses kernel smoothed templates derived from MC for signal and background [7] is used to understand the importance of the various systematic uncertainties. The systematics with the biggest effect on the mass measurement and the signal strength measurement are listed in Table 7.5 for the mass measurement and in Table 7.6 for the μ measurement. The change on the fitted parameter by varying the given nuisance parameter up $(+1\sigma)$ or down (-1σ) relative to the nominal value of the fitted parameter is shown.

Table 7.5: Nuisance parameters for 2012 signal and background models and their effect on the 2D template mass measurement (m_H).

Description	Nuisance parameter	$+\delta m_H$ (MeV)	$-\delta m_H$ (MeV)
Muon momentum scale:			
SCALE	MU_MS	39	40
Electron & photon energy scale:			
ZeeAll	EM_ES_Z	19	19

Table 7.6: Nuisance parameters for 2012 signal and background models and their effect on the 2D template signal strength (μ) measurement.

Description	Nuisance parameter	$+\delta\mu$	$-\delta\mu$
Luminosity 2012	LUMI_2012	0.027	0.029
Branching ratio $H \to ZZ$	BR_VV	0.040	0.042
PDF+α_S:			
$gg \to H$	pdf_Higgs_ggH	0.060	0.062
$q\bar{q} \to ZZ$	pdf_qq	0.010	0.010
QCD scale:			
$gg \to H$	QCDscale_ggH	0.058	0.071
$q\bar{q} \to ZZ$	QCDscale_VV	0.008	0.008
Electron reco+ID efficiencies:			
reco+ID stat, ID syst, $E_T > 20$ GeV	EL_2012_IDST_high	0.013	0.011
reco, $7 < E_T < 15$ GeV	EL_2012_REC_low	0.013	0.010
ID, $7 < E_T < 20$ GeV	EL_2012_ID_low	0.008	0.008
Electron cut efficiency	H4l_EL_EFF_ISOIP_2012	0.006	0.006
Muon reco & ID efficiencies	MU_EFF	0.014	0.013

7.9 Fit to m_{4l} and ZZ Discriminant Using Per-Event Response

At reconstruction level, the four-lepton invariant mass distribution is the convolution of the truth distribution, which here will be referred to as $g(m_{4l,true})$, with the mass response function $R(m_{4l,reco}, m_{4l,true})$. This mass response is derived from the individual lepton response functions (Section 7.2). The invariant mass distribution is given by the sum of the Higgs distribution, $g_H(m_{4l,true}, m_H, \Gamma_H)$ and the background distributions, $g_{bkg}(m_{4l,true})$ with the corresponding signal and background normalizations. The mass and width parameters can then be obtained by a fit of $R \otimes g$ to the measured four-lepton invariant mass spectrum after analysis selections.

7.9.1 Building the Probability Density Function

As discussed in the introduction, the goal of this measurement is to build a PDF which depends on the Higgs parameters, m_H, Γ_H, and signal strength, that describes the shape of the the observable quantities, such as the kinematics of the leptons and the m_{4l}. Additionally, constrained nuisance parameters which describe the normalization of the backgrounds and the variations on the lepton energy, scale, and efficiencies should be determined in the same maximization. When estimating the mass, the signal strength is allowed to vary but the width is fixed. Similarly, when the signal strength is estimated, the mass is allowed to vary but the width is fixed. When the width is estimated, the mass is fixed to a specific value and the signal strength is allowed to vary. The combined PDF will be in the form seen in Equation 7.30.

$$\text{Combined PDF} = N_{sig}(\text{Signal PDF}) + \sum_{i=1}^{\# \text{ bkgs}} N_{bkg,i}(\text{Background PDF}_i) \qquad (7.30)$$

Where N_{sig} represents the number of signal events and $N_{bkg,i}$ is the number of background events for each background type. Generally, the form of the PDFs, for either signal or background, can be written as seen in Equation 7.31:

$$PDF = P\left(m_{4l} | \vec{p_1}, \vec{p_2}, \vec{p_3}, \vec{p_4}; m_H, \Gamma_H\right) \cdot P\left(\vec{p_1}, \vec{p_2}, \vec{p_3}, \vec{p_4} | m_H, \Gamma_H\right) \qquad (7.31)$$

The 3×4 components of the momenta vectors would result in a 12-dimensional PDF. This can be simplified using a variable which encapsulates the useful kinematic information given by the four lepton momentum vectors. As discussed earlier, the variable used for this is the BDT (see Section 6.4.7). The BDT, encapsulates the difference between the kinematics of signal and background into one number. To ensure that there is a one-to-one relationship between the BDT and the lepton kinematics, the

kinematics of the lepton are compared between signal and background for different slices of BDT. The kinematics show good agreement between signal and background (as seen in Figure 7.28) although there are some discrepancies in the shape. The approximation, however, that the kinematics can be encapsulated by the BDT is validated, however, by the fits run on the MC samples discussed in Section 6.3. These fits show that the estimated parameters have no appreciable bias. Using the BDT as an approximation for the lepton kinematics, the background PDFs can be simplified greatly because the background shapes have no dependence on the Higgs parameters:

$$\text{Background PDF} = P\left(m_{4l}|BDT\right) \cdot P\left(BDT\right) \tag{7.32}$$

Using the approximation that $P\left(m_{4l}|\vec{p_1}, \vec{p_2}, \vec{p_3}, \vec{p_4}\right) \approx P\left(m_{4l}|BDT\right)$, the signal PDF can be written as:

$$\text{Signal PDF} = P\left(m_{4l}|\vec{p_1}, \vec{p_2}, \vec{p_3}, \vec{p_4}; m_H, \Gamma_H\right) \cdot P\left(BDT|m_H, \Gamma_H\right) \tag{7.33}$$

Because the mass response can be determined from the individual muon responses which are themselves specified by the lepton kinematics, the signal PDF is given by:

$$P\left(m_{4l}|m_{4l} \text{ response}; m_H, \Gamma_H\right) \cdot P\left(m_{4l} \text{ response}|\mu_i \text{ response}\right) \cdot \prod_{i=1}^{4} P\left(\mu_i \text{ response}|\vec{p_i}\right) \tag{7.34}$$

This reduces to the term found in Equation 7.33:

$$P\left(m_{4l}|m_H, \Gamma_H, \vec{p_1}, \vec{p_2}, \vec{p_3}, \vec{p_4}\right) \tag{7.35}$$

and the specific derivation of this term is found in Section 7.3. The background PDFs are discussed in Section 7.6 and Section 7.5.
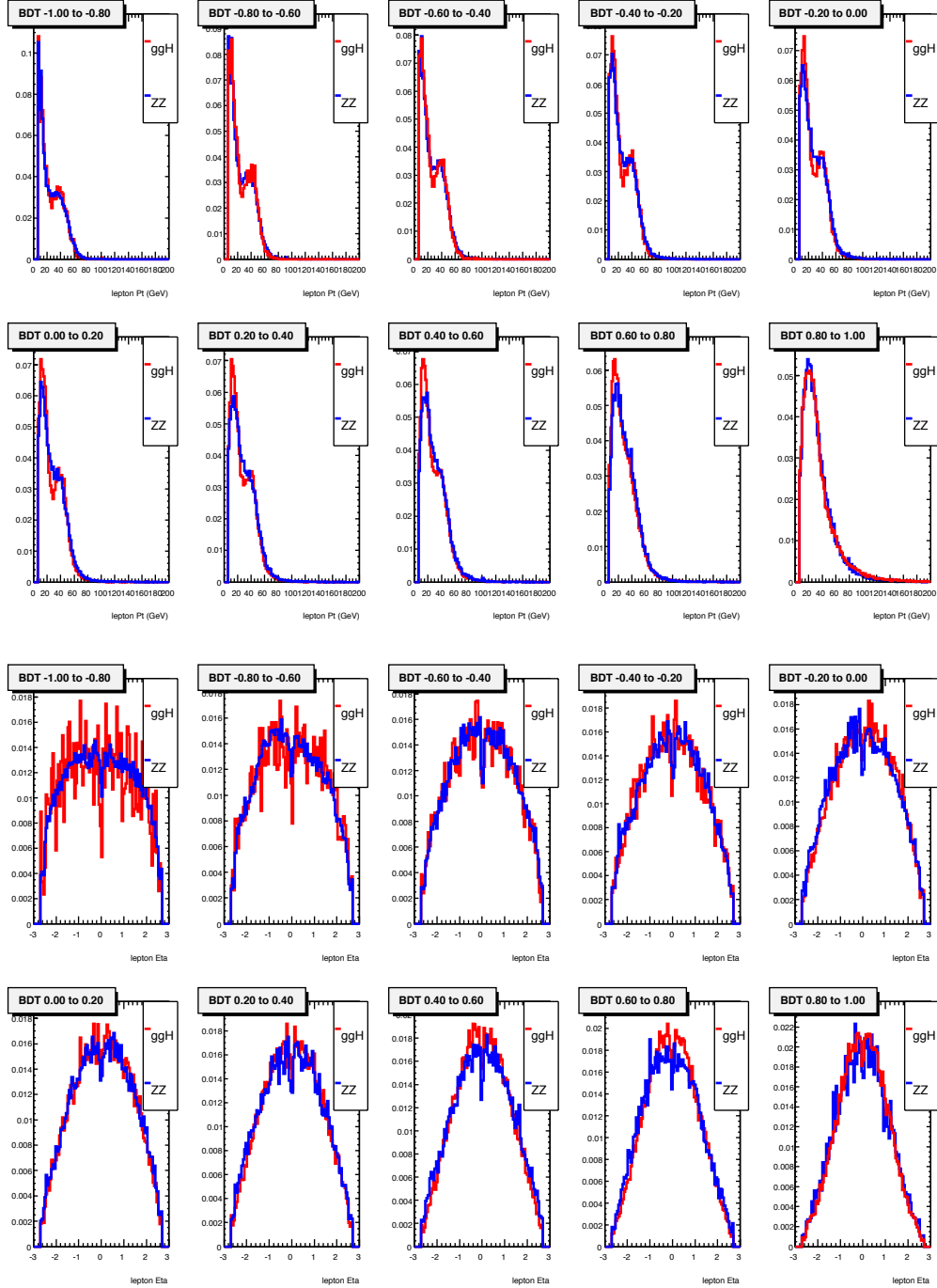
Figure 7.28: Comparison of the lepton kinematics for the Higgs signal ($m_H = 125$ GeV) shown in red and $ZZ^{(*)}$ background shown in blue. The first two rows show the lepton p_{T} while the second two rows show the lepton η. The events are split into 10 evenly spaced bins of BDT. For each event, all four leptons fill the corresponding histograms once.

7.9.2   The Combined Likelihood

Using the combined PDF (in Equation 7.30) allows a likelihood maximization to estimate the fit parameters of interest. These are the signal strength, μ; Higgs mass, m_H; and Higgs width, Γ_H. To estimate the value of these parameters, a negative log-likelihood scan is used. The equation which describes the full negative log-likelihood is seen in Equation 7.36.

$$ -\prod_{i=1}^{\#\text{ events}} \ln\left[\mathcal{L}\left(m_H, \Gamma_H, \mu_H | m_{4l,i}, BDT_i\right)\right] \tag{7.36} $$

This log-likelihood scan makes use of the fact that the likelihood is equal to the PDF (i.e. $\mathcal{L}(y|x) = P(x|y)$). Additionally, the negative log-likelihood scans shown in the results section represent the $-2\Delta(\ln\mathcal{L}) = -2(\ln\mathcal{L} - \ln\mathcal{L}_{max})$, where $\mathcal{L}_{max}$ is the the most likely value of the likelihood in a given range. The systematics are evaluated, as discussed in Section 7.8, by varying nuisance parameters which change the shape or normalization of the signal and background models. The additional variation through the use of nuisance parameters will translate into added uncertainties in the fit parameters of interest and accordingly the stated uncertainties include both statistical and systematic uncertainties. To disentangle the systematic uncertainties from the statistical uncertainty, it is necessary to perform the likelihood minimization without the nuisance parameters. This ensures that the only uncertainty is statistical. Subtracting (in quadrature) the uncertainty of the fit without nuisance parameters enabled from the uncertainty of the fit with nuisance parameters enabled gives the total systematic error on the measurement. A quantitative description of the effect of specific systematics on the measurement is discussed in Section 7.8.9.

From the negative log-likelihood scan, it is possible to determine the upper and

lower uncertainties on the most likely value of the parameter. The one sigma and negative one sigma bounds can be read off at the point where $-2\log\mathcal{L} = 1$. In addition, one can determine the 95% confidence intervals on the value of the parameter.

Scans are run on simulated MC events which are scaled to the expected luminosity for the 2011 and 2012 run periods in order to determine what the expected results should be and to give a point of comparison to the actual scans which are performed on 25 fb^{-1} of ATLAS data with a center-of-mass energy of 7 TeV for 2011 and 8 TeV for 2012. To produce the expected results, a signal MC sample is used with a Higgs mass of 125 GeV and the nominal Higgs width for this mass which is 4.1 MeV.

7.10 Results

With these signal and background models it is possible to fit the Higgs data directly using an unbinned maximum likelihood fit. In this procedure the background normalizations are set to their estimated values. Shape and normalization systematics are treated as nuisance parameters in the fit. The following tables and plots summarize the minima of the likelihood scans for the signal strength, μ; the mass, m_H; and the width, Γ_H. These are shown for each channel separately and for all channels combined. Furthermore, the results are split into the expected and observed results. The observed results are produced using the full ATLAS dataset while the expected results are run on MC samples discussed in Section 6.3 and scaled to the expected luminosity for 2011 or 2012 as needed. All stated uncertainties include statistical and systematic components.

To better understand the results in data, tables are presented which show the

relevant information for candidate events in the 110-140 GeV mass range. The mass and BDT for each event is shown, and the RMS of the multi-Gaussian per-event mass response is quoted as an encapsulation of the information contained in the per-event mass response. Tables 7.7, 7.8, 7.9, and 7.10 show the candidates for the 4μ, $2e2\mu$, $2\mu2e$, and $4e$ channels respectively. Unlike the event yields presented in Table 6.5, the reconstruction level invariant mass from these these tables does not have the Z-mass constraint applied.

Table 7.7: Candidate 4μ events in 2011 and 2012 data from the 110-140 GeV mass range. The first column is the reconstructed four lepton invariant mass for the event, the second column is the RMS of the per-event mass response for that event, the third column is the value of the BDT for the event, and the last column represents the year the event was measured in.

Mass (GeV)	Response RMS (GeV)	BDT	Year
113.4	1.66	0.86	2012
113.9	2.26	-0.81	2011
115.7	1.82	0.04	2011
118.8	1.94	0.63	2012
120.9	2.16	-0.81	2012
122.0	1.99	-0.54	2011
122.8	3.10	-0.85	2012
123.2	3.19	-0.01	2012
123.3	1.57	0.76	2012
123.6	1.99	-0.88	2012
123.8	2.22	0.37	2012
124.1	1.50	-0.13	2012
124.4	1.94	0.62	2012
124.6	1.80	0.60	2011
124.6	2.32	-0.55	2012
126.9	2.34	-0.31	2012
129.2	2.02	-0.12	2012
129.6	2.21	-0.38	2012
132.3	1.92	-0.59	2012
133.1	2.88	-0.06	2012
135.4	2.43	0.12	2012

Table 7.8: Candidate $2e2\mu$ events in 2011 and 2012 data from the 110-140 GeV mass range. The first column is the reconstructed four lepton invariant mass for the event, the second column is the RMS of the per-event mass response for that event, the third column is the value of the BDT for the event, and the last column represents the year the event was measured in.

Mass (GeV)	Response RMS (GeV)	BDT	Year
112.7	3.77	-0.06	2012
117.3	3.93	-0.06	2012
118.3	3.92	0.13	2012
123.8	2.63	0.58	2012
123.8	3.43	0.65	2012
124.0	3.81	0.38	2012
124.2	2.89	0.86	2011
124.9	4.60	-0.32	2012
125.5	4.60	0.85	2012
127.0	3.05	-0.22	2011
127.0	4.69	0.77	2012
129.9	5.68	0.40	2012
131.0	5.18	-0.95	2011
131.2	3.44	0.15	2012
134.4	2.84	0.66	2012

Table 7.9: Candidate $2\mu2e$ events in 2011 and 2012 data from the 110-140 GeV mass range. The first column is the reconstructed four lepton invariant mass for the event, the second column is the RMS of the per-event mass response for that event, the third column is the value of the BDT for the event, and the last column represents the year the event was measured in.

Mass (GeV)	Response RMS (GeV)	BDT	Year
115.5	2.57	0.58	2012
117.4	2.43	0.17	2012
117.7	2.06	-0.32	2012
118.5	2.97	0.47	2012
121.7	2.62	0.40	2012
122.0	2.47	-0.20	2012
124.3	3.44	0.28	2011
135.5	3.95	0.29	2012
136.5	2.76	0.19	2012

Table 7.10: Candidate 4*e* events in 2011 and 2012 data from the 110-140 GeV mass range. The first column is the reconstructed four lepton invariant mass for the event, the second column is the RMS of the per-event mass response for that event, the third column is the value of the BDT for the event, and the last column represents the year the event was measured in.

Mass (GeV)	Response RMS (GeV)	BDT	Year
111.1	5.71	0.32	2012
115.3	4.42	-0.67	2011
121.7	4.79	0.09	2012
122.8	4.02	0.53	2011
124.0	3.89	0.80	2012
125.4	2.39	0.89	2012
125.8	4.51	-0.57	2012
126.0	3.60	-0.46	2012
126.8	3.44	-0.85	2012
126.8	5.47	0.54	2012
129.1	5.60	0.56	2012
135.1	4.13	0.54	2012

Table 7.11 presents the expected results from 7 TeV MC. These scans are produced by scaling the ensemble of simulated events to the expected signal and background normalizations. The estimated mass, width, and signal strength of the Higgs are each consistent with the input values used to generate the MC samples. This indicates that there is no intrinsic bias to the fit. The width measurements in the subchannels are marked with "−" indicating that the likelihood scan is flat within the 0 - 30 GeV range used to perform the likelihood scan.

Table 7.11: Expected Higgs signal strength, mass and width measurement extracted using a likelihood scan with event-by-event resolution on Higgs MC ($m_H = 125$ GeV) at 7 TeV. Results are presented for each analysis channel and their combination. The uncertainty includes the statistical and systematic components.

Channel	Mass (GeV)	Signal Strength	Width (GeV)
4μ	$125.03^{+3.40}_{-3.09}$	$0.98^{+1.69}_{-0.75}$	−
$2e2\mu$	$124.95^{+5.02}_{-4.48}$	$0.99^{+2.28}_{-0.90}$	−
$2\mu2e$	$125.03^{+4.97}_{-4.53}$	$0.98^{+3.48}_{-0.88}$	−
$4e$	$124.81^{+5.19}_{-4.31}$	$0.84^{+4.26}_{-0.74}$	−
Combined	$124.98^{+2.30}_{-2.09}$	$0.97^{+1.02}_{-0.56}$	$0.0^{+12.7}_{-0.00}$

Table 7.12 shows the observed results for the mass, signal strength, and width of the Higgs using 7 TeV data. The width likelihood scans are less flat than the expected MC due to a few events near the signal region with high values of the BDT. The same effect is also seen in the estimated signal strengths which are noticeably larger than unity.

Table 7.13 presents the expected results from 8 TeV MC. As before, these scans are produced by scaling the ensemble of simulated events to the expected signal and background normalizations. As with the 7 TeV results, the estimated mass, width, and signal strength are each consistent with the input values used to generate the MC

Table 7.12: Observed Higgs signal strength, mass and width measurement extracted using a likelihood scan with event-by-event resolution on ATLAS data taken at 7 TeV. Results are presented for each analysis channel and their combination. The uncertainty includes the statistical and systematic components.

Channel	Mass (GeV)	Signal Strength	Width (GeV)
4μ	$124.07^{+1.95}_{-1.57}$	$2.00^{+2.50}_{-1.44}$	$0.0^{+6.22}_{-0.00}$
$2e2\mu$	$125.53^{+1.95}_{-1.64}$	$2.56^{+2.68}_{-1.58}$	$0.0^{+3.48}_{-0.00}$
$2\mu2e$	$123.24^{+6.75}_{-7.64}$	$1.71^{+3.72}_{-1.62}$	$-$
$4e$	$123.26^{+4.68}_{-2.86}$	$2.23^{+3.87}_{-2.09}$	$0.0^{+21.00}_{-0.00}$
Combined	$124.46^{+1.20}_{-1.02}$	$1.99^{+1.28}_{-0.94}$	$0.0^{+1.30}_{-0.00}$

Table 7.13: Expected Higgs signal strength, mass and width measurement extracted using a likelihood scan with event-by-event resolution on Higgs MC ($m_H = 125$ GeV) at 8 TeV. Results are presented for each analysis channel and their combination. The uncertainty includes the statistical and systematic components.

Channel	Mass (GeV)	Signal Strength	Width (GeV)
4μ	$125.00^{+1.18}_{-1.15}$	$1.00^{+0.59}_{-0.44}$	$0.0^{+4.05}_{-0.00}$
$2e2\mu$	$124.99^{+1.72}_{-1.61}$	$1.00^{+0.89}_{-0.58}$	$0.0^{+8.82}_{-0.00}$
$2\mu2e$	$124.97^{+2.09}_{-1.93}$	$1.00^{+0.74}_{-0.54}$	$0.0^{+9.30}_{-0.00}$
$4e$	$125.06^{+2.42}_{-2.36}$	$0.99^{+0.93}_{-0.60}$	$0.0^{+16.10}_{-0.00}$
Combined	$125.00^{+0.79}_{-0.78}$	$1.00^{+0.36}_{-0.30}$	$0.0^{+2.55}_{0.00}$

samples. This indicates that there is no intrinsic bias to the fit. Because muons have more narrow response functions and there is a larger event yield in the 4μ channel, the 4μ channel dominates the combined uncertainty on the mass, width, and signal strength.

Table 7.14 shows the observed results for the mass, signal strength, and width of the Higgs using 8 TeV data. Compared to the expected results, the uncertainty on the mass is lower. This is primarily due to the excess of events in the peak region first observed in the event yields in Table 6.5. The same effect is also seen in the measured signal strength.

Table 7.14: Observed Higgs signal strength, mass and width measurement extracted using a likelihood scan with event-by-event resolution on ATLAS data taken at 8 TeV. Results are presented for each analysis channel and their combination. The uncertainty includes the statistical and systematic components.

Channel	Mass (GeV)	Signal Strength	Width (GeV)
4μ	$124.20^{+0.80}_{-0.85}$	$1.53^{+0.75}_{-0.56}$	$0.0^{+1.17}_{-0.00}$
$2e2\mu$	$125.39^{+1.16}_{-1.14}$	$1.73^{+0.95}_{-0.69}$	$0.0^{+4.22}_{-0.00}$
$2\mu2e$	$119.71^{+1.68}_{-1.41}$	$3.14^{+1.83}_{-1.31}$	$10.20_{-8.72}$
$4e$	$126.12^{+1.17}_{-1.03}$	$2.10^{+1.12}_{-0.84}$	$0.0^{+4.84}_{-0.00}$
Combined	$124.57^{+0.54}_{-0.52}$	$1.72^{+0.48}_{-0.40}$	$0.0^{+1.93}_{0.00}$

Table 7.15: Expected Higgs signal strength, mass and width measurement extracted using a likelihood scan with event-by-event resolution on Higgs MC ($m_H = 125$ GeV) at 7 and 8 TeV combined. Results are presented for each analysis channel and their combination. The uncertainty includes the statistical and systematic components.

Channel	Mass (GeV)	Signal Strength	Width (GeV)
4μ	$124.97^{+1.10}_{-1.05}$	$1.00^{+0.55}_{-0.44}$	$0.0^{+2.50}_{-0.00}$
$2e2\mu$	$125.08^{+1.61}_{-1.51}$	$0.97^{+0.87}_{-0.56}$	$0.0^{+7.27}_{-0.00}$
$2\mu2e$	$125.00^{+1.93}_{-1.88}$	$0.99^{+0.85}_{-0.54}$	$0.0^{+8.68}_{-0.00}$
$4e$	$125.09^{+2.39}_{-2.29}$	$0.99^{+0.70}_{-0.50}$	$0.0^{+15.15}_{-0.00}$
Combined	$125.00^{+0.76}_{-0.80}$	$0.99^{+0.36}_{-0.26}$	$0.0^{+2.52}_{-0.00}$

Table 7.15 shows the expected results from 7 and 8 TeV MC. As with the individual 7 and 8 TeV expected results, the combined expectation is dominated by the 4μ channel. Again, there is no bias in the expected results.

Table 7.16 shows the observed results for 7 and 8 TeV ATLAS data. This represents the full run 1 ATLAS dataset. In data, the mass and the width measurements have substantially better uncertainties than expected. As seen in Table 7.7, the 4μ channel that drives the measurement has a number of events between 123 and 125 GeV with a high BDT and a narrow mass response. In general, the other channels have better Higgs width limits than expected. Typically this is due to a clustering of signal

events that have mass response functions that are more narrow than average. The

$2\mu2e$ channel has a very poor limit on the Higgs width. In this channel, there are three

events with high values of the BDT located well below 125 GeV as seen in Table 7.9.

To treat these events as signal, the fit widens the signal shape to accommodate.

Table 7.16: Observed Higgs signal strength, mass and width measurement extracted using a likelihood scan with event-by-event resolution on ATLAS data taken at 7 and 8 TeV. Results are presented for each analysis channel and their combination. The uncertainty includes the statistical and systematic components.

Channel	Mass (GeV)	Signal Strength	Width (GeV)
4μ	$124.21^{+0.73}_{-0.79}$	$1.60^{+0.72}_{-0.55}$	$0.0^{+0.94}_{-0.00}$
$2e2\mu$	$125.39^{+1.01}_{-0.93}$	$1.87^{+0.87}_{-0.65}$	$0.0^{+2.00}_{-0.00}$
$2\mu2e$	$120.62^{+1.54}_{-1.72}$	$2.84^{+1.53}_{-1.18}$	$6.00^{+18.2}_{-6.0}$
$4e$	$126.01^{+1.15}_{-1.02}$	$2.01^{+1.06}_{-0.76}$	$0.0^{+4.18}_{-0.00}$
Combined	$124.57^{+0.48}_{-0.43}$	$1.76^{+0.46}_{-0.37}$	$0.0^{+0.74}_{-0.00}$

Figures 7.29, 7.30, 7.31, and 7.32 show the likelihood scans for each of the four

analysis sub-channels (4μ, $2e2\mu$, $2\mu2e$, and $4e$ respectively) using the 7 and 8 TeV

combined MC samples. Figure 7.33 shows the likelihood scan for all channels com-

bined. At the left of each figure is the mass scan, in the middle is the signal strength

scan, and on the right is the width scan. Characteristically, the mass scan is symmet-

ric around the central value while the signal strength scan will rise sharply towards

zero. This is because a negative signal is not permitted by the fit. The width has

a minimum at zero with the negative log likelihood rising with increasing widths. It

should be noted that the width scan tends to level off. This is because the fit window

is between 110 GeV and 140 GeV and the signal model will appear flat in this range

for large values of the Higgs width. This means that the negative log-likelihood scan

will not rise parabolically (as it would in a typical likelihood scan) at large values of

Figure 7.29: Mass (left), signal strength (middle), and width (right) scans in 125 GeV Higgs MC for the 4μ channel including systematic uncertainties for the simulated MC 2011 and 2012 data set.
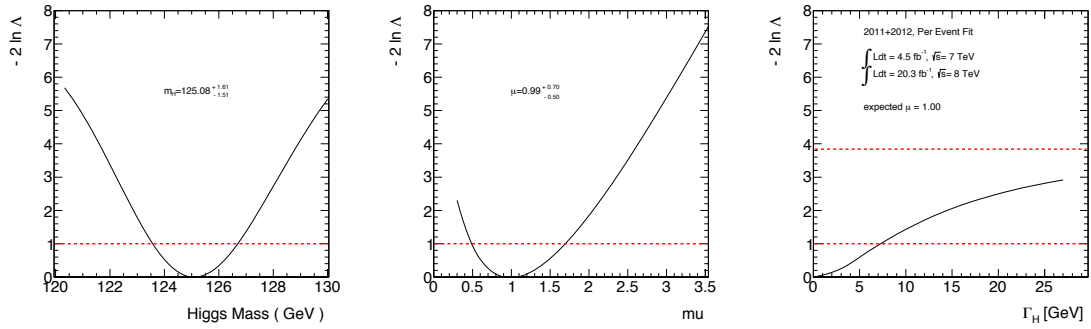
Figure 7.30: Mass (left), signal strength (middle), and width (right) scans in 125 GeV Higgs MC for the $2e2\mu$ channel including systematic uncertainties for the simulated MC 2011 and 2012 data set.

the Higgs width.

The likelihood scans of the width can be used to set exclusions on the width of the Higgs. The 95% expected Confidence-Level (CL) on the Higgs natural width using 8 TeV data is $\Gamma_H < 6.98$ GeV. For the combined 7 and 8 TeV data set, the expected limit is $\Gamma_H < 6.24$ GeV. This expected limit decreases to $\Gamma_H < 3.5$ at a 95% confidence limit when the SM signal is scaled to the observed excess. The actual observed limits are $\Gamma_H < 4.46$ GeV with 95% confidence using 8 TeV data and $\Gamma_H < 2.63$ GeV using the 7 TeV and 8 TeV data set. The difference between

175
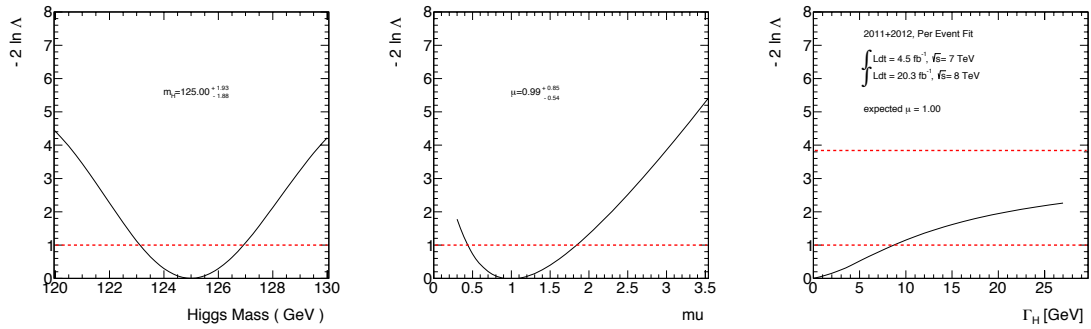
Figure 7.31: Mass (left), signal strength (middle), and width (right) scans in 125 GeV Higgs MC for the $2\mu2e$ channel including systematic uncertainties for the simulated MC 2011 and 2012 data set.
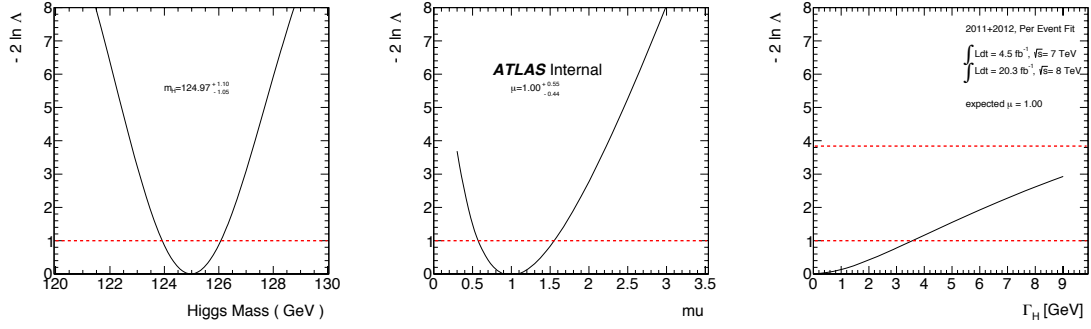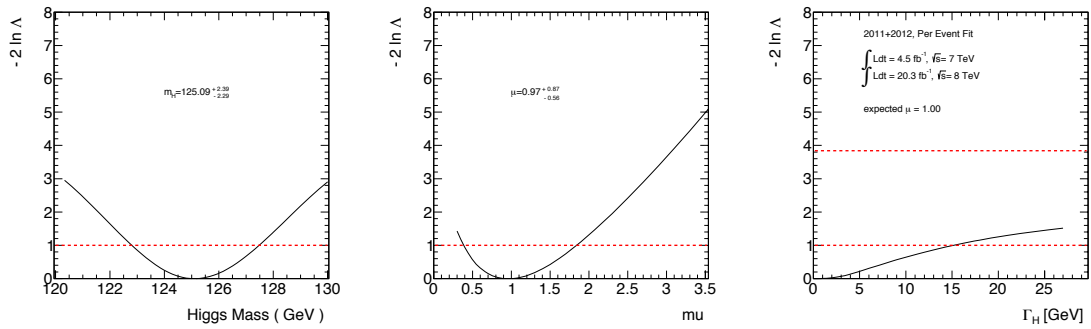

Figure 7.32: Mass (left), signal strength (middle), and width (right) scans in 125 GeV Higgs MC for the $4e$ channel including systematic uncertainties for the simulated MC 2011 and 2012 data set.
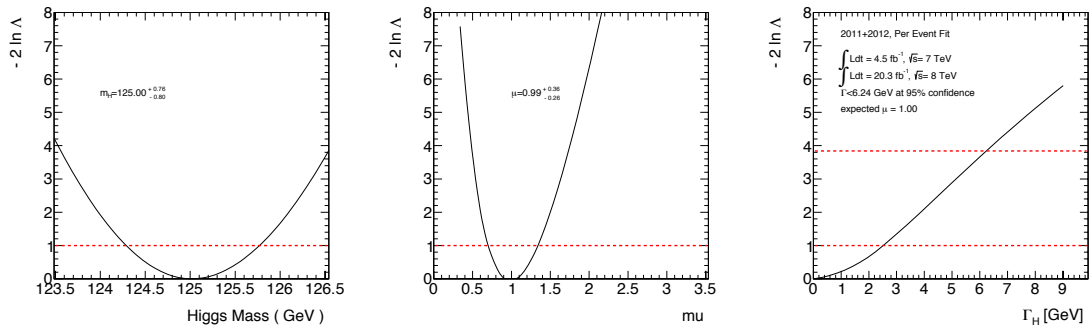
Figure 7.33: Mass (left), signal strength (middle), and width (right) scans in 125 GeV Higgs MC for all channels combined including systematic uncertainties for the simulated MC 2011 and 2012 data sets.

the observed and expected results is largely due to the higher than expected signal strength observed in data.

Chapter 8

Conclusions

In 2012, the Higgs boson was discovered. Since then, increased data and improved analysis techniques have reduced the statistical uncertainty on the mass of this new resonance. This thesis presents a new measurement of the signal strength, mass, and width of the Higgs boson using the full ATLAS dataset from run 1. These measurements were performed using a new technique that uses the detector response on an event-by-event level. This results in the most precise measurement of the Higgs mass using the 25 fb^{-1} of ATLAS data from 2011 and 2012. The measurement of the Higgs width using this technique provides the strongest exclusion limit on the width of the Higgs from a direct measurement of the invariant mass with either ATLAS or CMS data. The results from the event-by-event approach were published, along with complementary results from a 2D template[1] approach, in [7].

Using the event-by-event approach detailed in this thesis, the signal strength for

---

[1]The 2D template approach uses MC and data-driven based template models for the signal and background shapes in both BDT and m_{4l}

all channels is measured to be $1.76^{+0.46}_{-0.37}$. The corresponding 2D template approach

measures the signal strength to be $1.66^{+0.45}_{-0.38}$. The signal strength measured by the

ATLAS $H \to \gamma\gamma$ analysis is found to be $1.29^{+0.30}_{-0.30}$. These ATLAS measurements are

consistent within 1σ of each other and within 2σ of the SM prediction. Using 2011 and

2012 data, the CMS experiment measures a signal strength of $0.93^{+0.26}_{-0.23}(\text{stat})^{+0.13}_{-0.09}(\text{syst})$

in the $H \to ZZ^{(*)} \to 4\ell$ decay channel. This result does not show the same excess

present in the ATLAS measurements. The measurements of the Higgs signal strength

are shown in Figure 8.1.

Table 8.1: Higgs signal strength measurements performed using various approaches with 2011 and 2012 ATLAS and CMS data. Systematics are included in the quoted uncertainties.

Channel	Signal Strength
ATLAS $H \to 4\ell$ (event-by-event)	$1.76^{+0.46}_{-0.37}$
ATLAS $H \to 4\ell$ 2D template [7]	$1.66^{+0.45}_{-0.38}$
ATLAS $H \to \gamma\gamma$ [7]	$1.29^{+0.30}_{-0.30}$
CMS $H \to 4\ell$ [53]	$0.93^{+0.26}_{-0.23}(\text{stat})^{+0.13}_{-0.09}(\text{syst})$

The mass, in the $H \to ZZ^{(*)} \to 4\ell$, was measured to be $124.57^{+0.48}_{-0.43}$ GeV using

the event-by-event approach. As a point of comparison, the 2D template approach

measures the mass of the Higgs to be $m_H = 124.51^{+0.54}_{-0.51}$ GeV [7]. The event-by-event

approach exhibits a smaller uncertainty on the mass than the 2D template approach

because there is an excess of events near 125 GeV with well measured leptons.

An additional ATLAS measurement using the $H \to \gamma\gamma$ decay channel estimated

the mass of the Higgs to be $125.98^{+0.50}_{-0.50}$ GeV. The combination of the $H \to ZZ^{(*)}$ and

$H \to \gamma\gamma$ mass and width measurements is shown in Figure 8.1. This figure shows

the likelihood contours of a simultaneous fit to the signal strength and mass and

the combination, including all systematic uncertainties, of the two measurements. The Higgs mass from this combination is estimated to be $125.35^{+0.41}_{-0.41}$. The CMS experiment measures a Higgs mass of $125.6^{+0.45}_{-0.45}$ GeV in the $H \to 4\ell$ final state [53]. This is consistent with the various ATLAS measurements. Table 8.2 summarizes these results.

Table 8.2: Higgs mass measurements performed using various approaches with 2011 and 2012 ATLAS and CMS data. Systematics are included in the quoted uncertainties.

Channel	Mass Measurement (GeV)
ATLAS $H \to 4\ell$ (event-by-event)	$124.57^{+0.48}_{-0.43}$
ATLAS $H \to 4\ell$ 2D template	$124.51^{+0.54}_{-0.51}$
ATLAS $H \to \gamma\gamma$	$125.98^{+0.50}_{-0.50}$
ATLAS Combined (4ℓ 2D template + $\gamma\gamma$) [7]	$125.36^{+0.41}_{-0.41}$
CMS $H \to 4\ell$ [53]	$125.6^{+0.45}_{-0.45}$

The natural width of the Higgs boson measured in this thesis is used as the ATLAS baseline width measurement for the $H \to ZZ^{(*)} \to 4\ell$ analysis. The observed and expected log-likelihood scans are shown in Figure 8.2. A direct limit on the total width of the Higgs boson of $\Gamma_H < 2.6$ GeV at 95% confidence is observed. The expected limit for the SM Higgs is estimated to be $\Gamma_H < 6.2$ GeV at 95% confidence. The measurement is limited by the mass resolution of the detector. Much of the difference between the observed and expected limits on the Higgs width can be accounted for by the higher than expected signal yield. When scaled to the observed signal rate, the expected limit is found to be $\Gamma_H < 3.5$ GeV at 95% confidence. The 95% observed and expected exclusion confidence limits from the $H \to \gamma\gamma$ analysis are < 5.0 GeV and < 6.2 GeV respectively. The CMS experiment has performed a width measurement
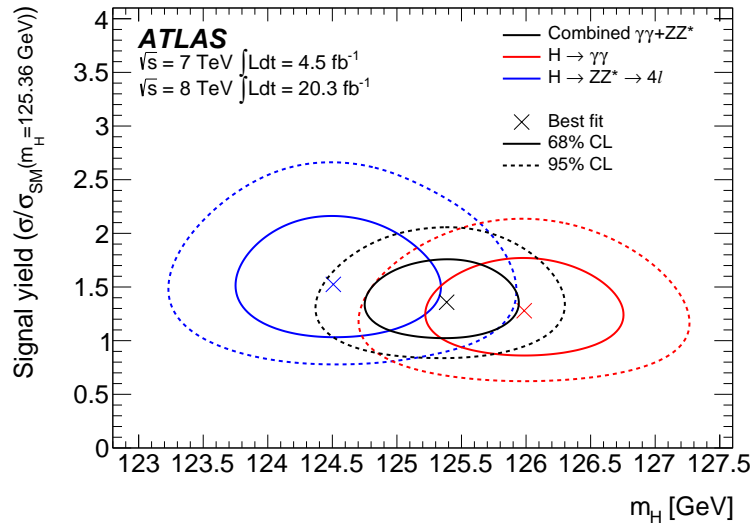
Figure 8.1: Likelihood contours $-2\ln\Lambda(S, m_H)$ as a function of the normalized signal yield $S = \sigma/\sigma_{SM}$ ($m_H = 125.36$ GeV) and m_H for the $H \to \gamma\gamma$ and $H \to ZZ^{(*)} \to 4\ell$ channels, where $H \to ZZ^{(*)}$ uses the 2D template approach, and their combination, including all systematic uncertainties. For the combined contour, a common normalised signal yield S is used. The markers indicate the maximum likelihood estimates in the corresponding channels [7].
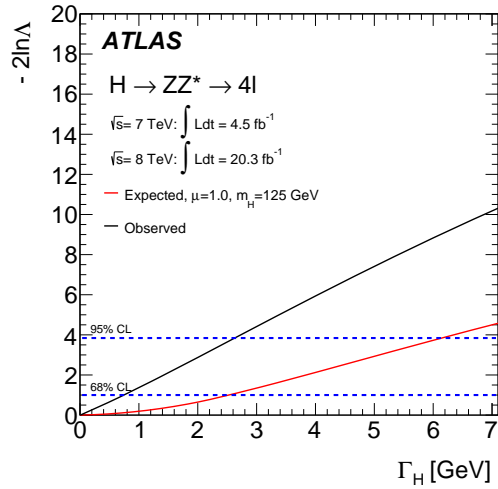
Figure 8.2: The profile likelihood as a function of Γ_H for the $H \rightarrow ZZ^{(*)} \rightarrow 4\ell$ channel for the combined $\sqrt{s} = 8$ TeV and $\sqrt{s} = 7$ TeV ATLAS data samples.

using data from the 2011 and 2012 run periods [53]. The observed and expected 95% confidence limits on the width of the Higgs resonance from this measurement are < 3.4 GeV and < 2.8 GeV respectively[2]. All limits using data from p-p collisions at the LHC are compatible with the expected 4.1 MeV natural width of a 125 GeV Standard Model Higgs boson.

The direct measurements presented in this thesis of the width and signal strength of the particle discovered in 2012 [15, 16] support the hypothesis that the resonance is the Standard Model Higgs boson predicted by Peter Higgs, François Englert, Robert Brout, Gerald Guralnik, C. R. Hagen, and Tom Kibble [12–14].

As discussed in Section 2.3, the mass of the Higgs is an important component when checking the consistency of the Standard Model of particle physics. The mass of the top quark, the W-boson, and the Higgs boson are related to each other through

---

[2]An additional CMS measurement which determines the width of the Higgs boson using off-shell production of Z-boson pairs was performed in [54]. Using this procedure, the width of the Higgs is found to be less than 22 MeV at the 95% confidence level.

higher order loop corrections. Using a fit to the electroweak observables, a check on the consistency of the SM can be performed. These consistency checks are described in [8]. The mass of the Higgs used in the fit is the average of the ATLAS [7] and CMS [55] measurements. The p-value for the SM to describe the data is calculated to be 0.21 which corresponds to a 0.8σ one-sides significance [8].

Figure 8.3 presents the results of the electroweak fit and their constraints on the mass of the W boson and the top quark. The grey contours show the constraints without including measurements of the Higgs mass. Including the average of the Higgs mass as measured by ATLAS and CMS in the global electroweak fit greatly improves the constraint as shown by the blue contours. The constraints are consistent with the direct measurements of the top and W masses within their uncertainties. If statistically significant deviations between the fit results and the direct measurements were to appear, they could be an indication of new physics.

With the 2015 LHC run, the $H \rightarrow ZZ^{(*)} \rightarrow 4\ell$ analysis will become more powerful because the analysis is heavily dominated by the statistical uncertainty on the measurement. With increased data, the precision on the mass, width, and signal strength measurements will increase substantially. Additional measurements, performed on data from the 2015 LHC run, will shed light on the discrepancies between the $H \rightarrow ZZ^{(*)} \rightarrow 4\ell$ measured signal strength and the Standard Model prediction.
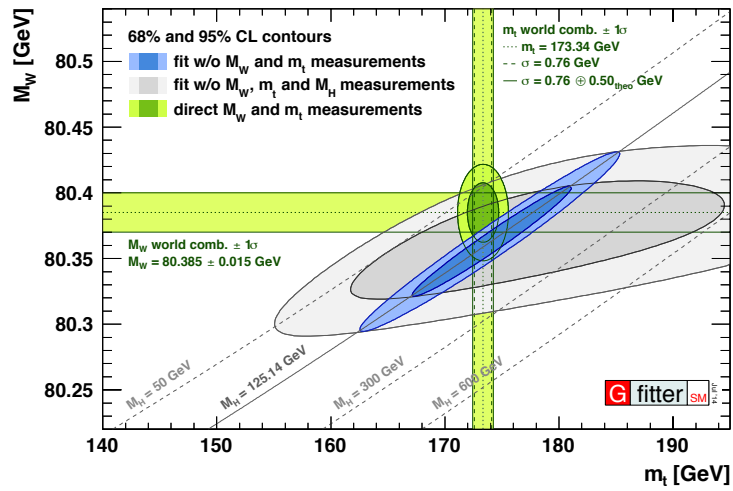
Figure 8.3: Contours of 68% and 95% confidence level obtained from scans of fits with fixed variable pairs m_W vs. m_t. The narrower blue and larger grey allowed regions are the results of the fit including and excluding the m_H measurements, respectively. The horizontal bands indicate the 1σ regions of the m_W and m_t measurements (world averages) [8].

Bibliography

[1] LHC Higgs Cross Section Working Group, S. Dittmaier et al., *Handbook of LHC Higgs Cross Sections: 1. Inclusive Observables*, `arXiv:1101.0593 [hep-ph]`.

[2] LHC Higgs Cross Section Working Group, S. Heinemeyer et al., *Handbook of LHC Higgs Cross Sections: 3. Higgs Properties*, `arXiv:1307.1347 [hep-ph]`.

[3] The ATLAS Collaboration, *ATLAS detector and physics performance: Technical Design Report, 1.* CERN, Geneva, 1999.

[4] ATLAS Collaboration, G. Aad et al., *The ATLAS Experiment at the CERN Large Hadron Collider*, JINST **3** (2008) no. 08, S08003.

[5] The ATLAS Collaboration, *ATLAS tile calorimeter: Technical Design Report.* CERN, Geneva, 1996.

[6] The ATLAS Collaboration, *Preliminary results on the muon reconstruction efficiency, momentum resolution, and momentum scale in ATLAS 2012 pp collision data*, ATLAS-CONF-2013-088, 2013.

[7] The ATLAS Collaboration, G. Aad et al., *Measurement of the Higgs boson mass from the $H \to \gamma\gamma$ and $H \to ZZ^* \to 4\ell$ channels with the ATLAS detector using 25 fb^{-1} of pp collision data*, `arXiv:1406.3827 [hep-ex]`.

[8] The Gfitter Group, M. Baak, J. Cuth, J. Haller, A. Hoecker, R. Kogler, K. Moenig, M. Schott, and J. Stelzer, *The global electroweak fit at NNLO and prospects for the LHC and ILC*, DESY-14-124. CERN-OPEN-2014-038, 2014. `arXiv:1407.3792 [hep-ph]`.

[9] Particle Data Group, J. Beringer et al., *Review of Particle Physics*, Phys. Rev. D **86** (2012) 1528.

[10] M. Lamont, *The First Years of LHC Operation for Luminosity Production*, in *Proceedings of IPAC2013*. Shanghai, 2013.

[11] M. Lamont, *Status of the LHC*, J. Phys. Conf. Ser. **455** (2013) 012001.

[12] F. Englert and R. Brout, *Broken Symmetry and the Mass of Gauge Vector Mesons*, Phys. Rev. Lett. **13** (1964) 321–323.

[13] P. W. Higgs, *Broken Symmetries and the Masses of Gauge Bosons*, Phys. Rev. Lett. **13** (1964) 508–509.

[14] G. S. Guralnik, C. R. Hagen, and T. W. B. Kibble, *Global Conservation Laws and Massless Particles*, Phys. Rev. Lett. **13** (1964) 585–587.

[15] The ATLAS Collaboration, G. Aad et al., *Observation of a new particle in the search for the Standard Model Higgs boson with the ATLAS detector at the LHC*, Phys. Rev. B **716** (2012) 1–29, `arXiv:1207.7214 [hep-ex]`.

[16] The CMS Collaboration, S. Chatrchyan et al., *Observation of a new boson with mass near 125 GeV in pp collisions at $\sqrt{s}$ = 7 and 8 TeV*, JHEP **1306** (2013) 081, `arXiv:1303.4571 [hep-ex]`.

[17] F. Halzen and A. D. Martin, *Quarks and leptons: An Introductory Course in Modern Particle Physics*. Wiley, 2008.

[18] M. E. Peskin and D. V. Schroeder, *An Introduction to Quantum Field Theory*. Advanced book classics. Addison-Wesley Publishing Company, 1995.

[19] M. Baak, M. Goebel, J. Haller, A. Hoecker, and D. Ludwig, *Updated Status of the Global Electroweak Fit and Constraints on New Physics*, Eur. Phys. J **C72** (2012) 2003, `arXiv:1107.0975 [hep-ph]`.

[20] L. Evans and P. Bryant, *LHC Machine*, JINST **3** (2008) S08001.

[21] The ATLAS Collaboration, *ATLAS central solenoid: Technical Design Report*. CERN, Geneva, 1997.

[22] The ATLAS Collaboration, *ATLAS magnet system: Technical Design Report, 1*. CERN, Geneva, 1997.

[23] The ATLAS Collaboration, *ATLAS inner detector: Technical Design Report, 1*. CERN, Geneva, 1997.

[24] The ATLAS Collaboration, S. Haywood, L. Rossi, R. Nickerson, and A. Romaniouk, *ATLAS inner detector: Technical Design Report, 2*. CERN, Geneva, 1997.

[25] The ATLAS Collaboration, *ATLAS calorimeter performance: Technical Design Report.* CERN, Geneva, 1996.

[26] The ATLAS Collaboration, *ATLAS muon spectrometer: Technical Design Report.* CERN, Geneva, 1997.

[27] The ATLAS Collaboration, *A measurement of the ATLAS muon reconstruction and trigger efficiency using J/ψ decays*, ATLAS-CONF-2011-021, 2011.

[28] The ATLAS Collaboration, G. Chiodini, N. Orlando, and S. Spagnolo, *A measurement of the muon reconstruction efficiency in 2010 ATLAS data using J/ψ decays*, ATL-COM-MUON-2011-032, 2011.

[29] The ATLAS Collaboration, *Determination of the muon reconstruction efficiency in ATLAS at the Z resonance in proton-proton collisions at $\sqrt{s} = 7$ TeV*, ATLAS-CONF-2011-008, 2011.

[30] The ATLAS Collaboration, N. Orlando, *Muon reconstruction efficiency measurement in the ATLAS experiment*, ATL-PHYS-PROC-2012-011, 2012.

[31] S. Sjostrand, S. Mrenna, and P. Skands, *PYTHIA 6.4 Physics and Manual*, JHEP **0605** (2006) 026, `arXiv:0711.2473 [hep-ph]`.

[32] S. Agostinelli et al., *Geant4 a simulation toolkit*, Nucl. Instrum. Meth. A **506** (2006) 250–303.

[33] The ATLAS Collaboration, G. Aad et al., *The ATLAS Simulation Infrastructure*, Eur. Phys. J **C70** (2010) 823–874, `arXiv:1005.4568 [physics.ins-det]`.

[34] S. Hassani et al., *A muon identification and combined reconstruction procedure for the ATLAS detector at the LHC using the (MUONBOY, STACO, MuTag) reconstruction packages*, Nucl. Instrum. Meth. A **572** (2007) 77–79.

[35] D. Adams et al., *Track reconstruction in the ATLAS Muon Spectrometer with MOORE 007*, ATL-SOFT-2003-007, 2003.

[36] The ATLAS Collaboration, G. Aad et al., *Measurement of the muon reconstruction performance of the ATLAS detector using 2011 and 2012 LHC proton-proton collision data*, `arXiv:1407.3935 [hep-ex]`.

[37] S. Alioli, P. Nason, C. Oleari, and E. Re, *NLO Higgs boson production via gluon fusion matched with shower in POWHEG*, JHEP **0904** (2009) 002, `arXiv:0812.0578 [hep-ph]`.

[38] P. Nason and C. Oleari, *NLO Higgs boson production via vector-boson fusion matched with shower in POWHEG*, JHEP **1002** (2010) 037, `arXiv:0911.5299 [hep-ph]`.

[39] T. Sjostrand, S. Mrenna, and P. Z. Skands, *A Brief Introduction to PYTHIA 8.1*, Comput. Phys. Commun. **178** (2008) 852–867, `arXiv:0710.3820 [hep-ph]`.

[40] P. Golonka and Z. Was, *PHOTOS Monte Carlo: A Precision tool for QED corrections in Z and W decays*, Eur. Phys. J **C45** (2006) 97–107, `arXiv:hep-ph/0506026 [hep-ph]`.

[41] T. Melia, P. Nason, R. Rontsch, and G. Zanderighi, W^+W^-, WZ and ZZ

production in the POWHEG BOX, JHEP **1111** (2011) 078, `arXiv:1107.5051`
`[hep-ph]`.

[42] M. L. Mangano, M. Moretti, F. Piccinini, R. Pittau, and A. D. Polosa,
ALPGEN, a generator for hard multiparton processes in hadronic collisions,
JHEP **0307** (2003) 001, `arXiv:hep-ph/0206293 [hep-ph]`.

[43] T. Gleisberg, S. Hoeche, F. Krauss, M. Schonherr, S. Schumann, et al., *Event
generation with SHERPA 1.1*, JHEP **0902** (2009) 007, `arXiv:0811.4622`
`[hep-ph]`.

[44] The ATLAS Collaboration, G. Aad et al., *Electron reconstruction and
identification efficiency measurements with the ATLAS detector using the 2011
LHC proton-proton collision data*, Eur. Phys. J **C74** (2014) 2941,
`arXiv:1404.2240 [hep-ex]`.

[45] The ATLAS Collaboration, *Improved electron reconstruction in ATLAS using
the Gaussian Sum Filter-based model for bremsstrahlung*,
ATLAS-CONF-2012-047, 2012.

[46] S. Dittmaier, S. Dittmaier, C. Mariotti, G. Passarino, R. Tanaka, et al.,
Handbook of LHC Higgs Cross Sections: 2. Differential Distributions,
`arXiv:1201.3084 [hep-ph]`.

[47] A. Hoecker et al., *TMVA - Toolkit for Multivariate Data Analysis*, PoS ACAT
040 (2007) .

[48] J. Alwall, R. Frederix, S. Frixione, V. Hirschi, F. Maltoni, et al., *The automated*

computation of tree-level and next-to-leading order differential cross sections, and their matching to parton shower simulations, JHEP **1407** (2014) 079, `arXiv:1405.0301 [hep-ph]`.

[49] ATLAS Collaboration, G. Aad et al., *Measurement of Four-Lepton Production at the Z Resonance in pp Collisions at $\sqrt{s} = 7$ and 8 TeV with ATLAS*, Phys. Rev. Lett. **112** (2014) 231806, `arXiv:1403.5657 [hep-ex]`.

[50] I. Antcheva, M. Ballintijn, B. Bellenot, M. Biskup, R. Brun, et al., *ROOT: A C++ framework for petabyte data storage, statistical analysis and visualization*, Comput. Phys. Commun. **182** (2011) 1384–1385.

[51] The ATLAS Collaboration, *Electron efficiency measurements with the ATLAS detector using the 2012 LHC proton-proton collision data*, ATLAS-CONF-2014-032, 2014.

[52] S. H. Abidi et al., *Event selection and background estimation for the measurement of the properties of the Higgs particle in the four lepton decay channel with the ATLAS detector*, ATL-COM-PHYS-2013-1599, 2013.

[53] The CMS Collaboration, *Properties of the Higgs-like boson in the decay H to ZZ to 4ℓ in pp collisions at $\sqrt{s} = 7$ and 8 TeV*, CMS-PAS-HIG-13-002, 2013.

[54] The CMS Collaboration, *Constraints on the Higgs boson width from off-shell production and decay to Z-boson pairs*, Phys. Rev. B **736** (2014) 64. 29 p, `arXiv:1405.3455 [hep-ex]`.

[55] The CMS Collaboration, *Precise determination of the mass of the Higgs boson*

and studies of the compatibility of its couplings with the standard model,

CMS-PAS-HIG-14-009, 2014.